Switching Activation Barriers: New Insights in E-field driven processes at the interface

Perspectives in physical chemistry and catalysis

SWITCHING ACTIVATION BARRIERS: NEW INSIGHTS IN E-FIELD DRIVEN PROCESSES AT THE INTERFACE

PERSPECTIVES IN PHYSICAL CHEMISTRY AND CATALYSIS

Promotion committee

Prof. Dr. Ir. L. Lefferts (promotor)	University of Twente	The Netherlands
Prof. Dr. J. G. E. Gardeniers (promotor)	University of Twente	The Netherlands
Dr. A. van Houselt (assistant promotor)	University of Twente	The Netherlands
Prof. Dr. D. Lohse	University of Twente	The Netherlands
Prof. Dr. S. Franssila	Aalto University	Finland
Prof. Dr. Ir. A. I. Stankiewicz	Delft University of Technology	The Netherlands
Prof. Dr. G. Mul	University of Twente	The Netherlands
Prof. Dr. Ir. R. G. H. Lammertink (chairman)	University of Twente	The Netherlands

Cover design by the silver-jewelry and graphical designer Rossana Yañez Mendoza. The cover symbolizes my PhD journey.

Switching Activation Barriers: New Insights in E-field driven processes at the interface

Perspectives in Physical Chemistry and Catalysis

ISBN: 978-90-365-3646-2

Printed by: Gildeprint Drukkerijen – The Netherlands

This work is financially supported by NWO (Netherlands' Organization for Scientific Research) under grant No. 700.58.041.

SWITCHING ACTIVATION BARRIERS: NEW INSIGHTS IN E-FIELD DRIVEN PROCESSES AT THE INTERFACE

PERSPECTIVES IN PHYSICAL CHEMISTRY AND CATALYSIS

DISSERTATION

To obtain
the degree of doctor at the University of Twente,
on the authority of the rector magnificus,
Prof. Dr. H. Brinksma
on account of the decision of the graduation committee,
to be publicly defended
on Friday 11th of April 2014 at 16:45

by

Arturo Susarrey Arce

born on August 7th, 1981
in La Paz, Baja California Sur, México

This dissertation has been approved by the promoters

Prof. dr. ir. L. Lefferts

Prof. dr. J. G. E. Gardeniers

A mi abuelo, Arturo Susarrey Acero

Siempre estás a mi lado

In the end, just three things matter:

How well we have lived,

How well we have loved,

How well we have learned to let go - *Jack Kornfield*

Contents

Chapter 1 **1-8**

Activation Barriers at the Interface

Perspectives in physical chemistry and catalysis

1. Linking and switching 2
1.1. Why switching activation barriers? 2
1.2. Electronic control of a reaction at the surface 3
1.2.1. Why electrical fields? 3
1.2.2. Why microstructures? 4
1.3. Why an ATR-IR microreactor? 5
1.4. Scope and outline of this thesis 6-7
1.5. References 8

Chapter 2 **9-22**

Microreactor fabrication

From superhydrophobic surfaces to electrodes for chemistry

2.1. Introduction 10
2.2. Experimental section 10-12
2.3. Results and discussions 13
2.3.1. Microstructure shapes obtained with system RIE-1 13-15
2.3.2. Microstructure shapes obtained with system RIE-2 16-
2.3.3. Wetting behavior of the fabricated structures 17-19
2.4. Conclusions 20
2.5. References 22
Chapter 3 **23-42**

E-field electrodes

Towards the design of omniphobic surfaces and its applications

3.1. Omniphobicity 24-26
3.2. Experimental section 26-27
3.3. Results and discussions 27
3.3.1. Samples and contact angles 27-29
3.3.2. Evaporation of water droplets 29-31
3.3.3. Evaporation of a colloidal solution 31-32
3.3.4. Comparing with mechanisms from literature 32-36

3.3.5. The global energy argument crises 36-37
3.3.6. Colloidal fakir droplets leading to microsoccerballs 37-38
3.4. Conclusions 38-39
3.5. References 40-42
Chapter 4 **43-84**

Combining microreactor technology with ATR-IR
In situ characterization and microreactor system integration

4.1. E-field driven processes in an ATR-IR microreactor 44-45
4.2. Experimental section 45
4.2.1. Microreactor design and fabrication and characterization of $TiSi_2$ electrodes 45-48
4.3. Results and discussion 48
4.3.1. Electrical characterization of E-field controlled microreactors 48-53
4.3.2. Infrared measurement of effects introduced by the application of an electric field 53
4.3.2.1. Optical interference effects 53-56
4.3.2.2. Phonon generation and relaxation 57-58
4.3.2.3. Decrease of the 1727 cm^{-1} interstitial oxygen band 58
4.3.3. Infrared measurement of gases and liquids under application of an electric field 59
4.3.3.1. CO_2 59-61
4.3.3.2. Decomposition of ammonium 61-63
4.4. Conclusions and outlook 63-64
4.5. References 65-67
Chapter 4-*Supporting Information* 68-84
Chapter 5 **85-100**

A newly developed ATR-IR Microreactor
The study of interstitial oxygen (O_i) defects

5.1. O_i in silicon 86-87
5.2. Experimental section 87
5.2.1. Fabrication of the internal reflection elements and ATR-IR microreactors 87-88
5.2.2. Optical and electrical experiments 89
5.3. Results and discussion 90-98
5.4. Conclusions 98
5.5. References 99-100

Chapter 6 **101-122**

Electric field-induced molecular polarization of *n*-hexane in an ATR-IR microreactor

6.1. Solvated electrons in *n*-hexane 102-103

6.2. Experimental section 103-104

6.3. Results and discussion 104

6.3.1. Electron transport in *n*-hexane and 1-hexene 104-106

6.3.2. Effect of E-field on IR spectra 107-111

6.3.3. Observation of infrared-inactive vibrations 111-114

6.3.4. Induced -CH_3 bending 114-115

6.4. Conclusions and recommendations 115

6.5. References 116-117

Chapter 6-*Supporting Information* 118-122

Chapter 7 **123-138**

CO adsorption on Pt nanoparticles in low E-fields studied by ATR-IR spectroscopy

7.1. CO adsorption by ATR-IR 124

7.2. Experimental section 124

7.2.1. Fabrication of the ATR-IR microreactors 124-125

7.2.2. Coating of the gas flow channel with Pt nanoparticles 125

7.2.3. Electrical characterization of the Pt coated microreactors 125

7.2.4. Pre-treatment of the microreactors 125-126

7.2.5. CO adsorption/oxidation cycles 126

7.2.6. ATR-IR measurements 126-127

7.3. Results 127

7.3.1. Coating the gas flow channel of the ATR-IR microreactor with Pt particles 127

7.3.2. Electrical characterization of the microreactors 128-129

7.3.3. CO adsorption ATR-IR measurements 130-133

7.4. Discussions 134

7.4.1. Coating the gas flow channel of the ATR-IR microreactor with Pt particles 134

7.4.2. Electrical characterization of the microreactors 134

7.4.3. CO adsorption ATR-IR measurements 134-136

7.5. Conclusions 136-137

7.6. References 138

Chapter 8 **139-151**
CO oxidation on Pt nanoparticles in low E-fields studied by ATR-IR spectroscopy
8.1. CO oxidation by ATR-IR 140
8.2. Experimental section 140-142
8.3. Results 143
8.3.1. CO oxidation without E-field 143
8.3.2. E-field CO saturation + E-field CO oxidation (experiment 1) 144-146
8.3.3. E-field oxidation (Experiment (2)) 146-147
8.3.4. E-field saturation (experiment (3)) 147-148
8.4. Discussions 148
8.4.1. E-field saturation + oxidation (experiment (1)) 148-149
8.4.2. E-field oxidation (Experiment (2)) 149-150
8.4.3. E-field saturation (experiment (3)) 150
8.5. Conclusions 150
8.6. References 151
Chapter 9 (English version) *i-vi*
Summary and Outlook
Closing of an E-field cycle
Chapter 9 (Dutch version) *vii-xii*
Samenvatting en Outlook
"*Closing of an E-field cycle*"
About the Author *xiii*
About the cover of my thesis *xiii*
Publications *xiv-xv*
Acknowledgements *xvi-xvii*

1

Activation Barriers at the Interface:

Perspectives in physical chemistry and catalysis

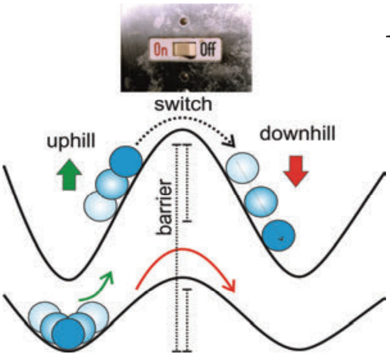

In this thesis we investigate the effect of a tuneable and switchable electrical field (E-field) generated in a microreactor as a new approach to control the selectivity of a chemical reaction. To fulfil this aim, we fabricate a microreactor, which allows the use of *in-situ* ATR-IR (attenuated total reflection infrared) spectroscopy to study the E-field-induced effects during a catalytic reaction. The basic configuration of the silicon-based homemade microreactor consist of a flow channel with integrated electrodes for application of the external E-field. In this chapter we describe the motivation for this work and introduce the underlying principles.

"*Switch* ***on*** *the light*"

1. Linking and switching

1.1. Why switching activation barriers?

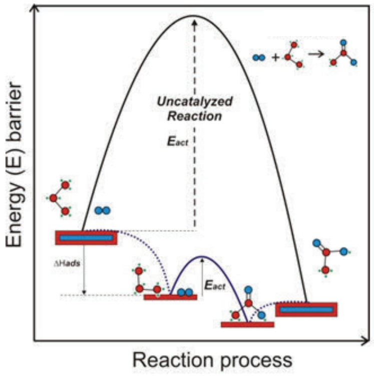

Figure 1. Energy barrier for an uncatalyzed and catalysed reaction.

The concept of **activation energy** is introduced by S. Arrhenius[1] in 1889, which is the minimum energy that is needed to make a chemical reaction to happen. The activation energy can be thought of as the height of the **potential barrier** separating two minima of **potential energy**. This general concept is applicable in many different fields. In the field of catalysis it is an ongoing effort to improve the kinetics of a reaction, by lowering the **activation barrier** (**E_{act}**, see **Figure 1**). In heterogeneous catalysis this is achieved by adsorption of one or more molecules on the surface of a catalyst, e.g. metal nanoparticles or a porous oxide. By the adsorption at the surface, the internal bonds within the molecule are weakened (activated) and, hence the activation energy for a reaction is lowered. After the reaction on the surface, the product desorbs, and a next reaction can take place and the catalytic cycle is closed. The reaction step which exhibits the lowest reaction rate (which usually has the highest activation barrier), is rate determining. Which step- adsorption, surface reaction or desorption – is rate determining, depends on the catalyst and the reactants/products.

In this thesis attempts to investigate the feasibility to use an external electrical field (E-field) to lower the activation barrier of chemical reaction are described.

1.2. Electronic control of a reaction at the surface

1.2.1. Why electrical fields?

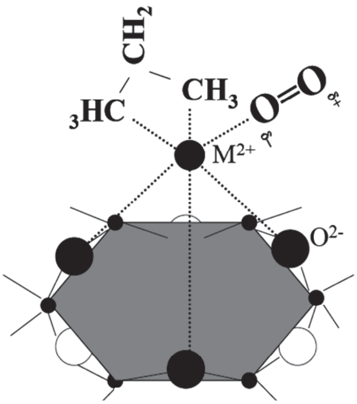

Figure 2. Schematic adsorption of propane an oxygen on changed in the Ca-modified Zeolite Y (dimensions are not drawn to scale).

The motivation for this study originates from the selective oxidation of propane over zeolite Y.[2-4] Selectivity is particularly important in oxidation reactions, since it is difficult to stop the oxidation at the right moment, preventing deep oxidation to CO_2 and water. In zeolite Y the active sites (adsorption sites) are located at specific positions. This catalyst has very well defined cages of 1.2 nm,[2] in which a alkali metal ion (M^{2+}), e.g. Ca^{2+}, acts as an active site for the co-adsorption of propane and oxygen,[3] via **electrostatic interaction**. The position of the active site in the cage promotes a specific orientation or conformation of the reactants, schematically presented in **Figure 2**. However, the acetone, which is the main product, cannot desorb due to the electrostatic interaction. To desorb the acetone from the Zeolite Y cage, a sufficient amount of energy is needed and this is usually done by providing heat.[3] Inspired by the effect of the electric field of the Ca^{2+} ion in the selective of oxidation of propane over Ca-modified zeolite Y,[2-3] the idea which is explored in this thesis is to decrease the activation barrier of a catalytic reaction by using an external E-field. The catalytic cycle can be closed if the products desorb from the surface when the E-field is switched off. To this aim a microreactor which allows application of an external electrical field is developed.

1.2.2 Why microstructures?

H. J. Kreuzer, reported on calculations of the adsorption of chemical species on metal surfaces,[5] in the present of a weak electrical fields (<0.1 V/nm). By polarizing the solid surface, the adsorption of different molecules is expected to increase drastically, due to the distortion of the binding orbital, which leads to new bonding properties.[5] In order to generate field strengths in this order of magnitude, the fabrication of microelectrodes with microstructures similar to the field emitter tips[5] will be discussed. The sharp curvature of the microstructures is expected to enhance the local E-field. In **Figure 3** a schematic representation of the proposed microstructures used as a microelectrodes is presented. Each microstructure is expected to act somehow similar to the adsorption site in Ca-modified Zeolite Y[2-4] in **Figure 2**.

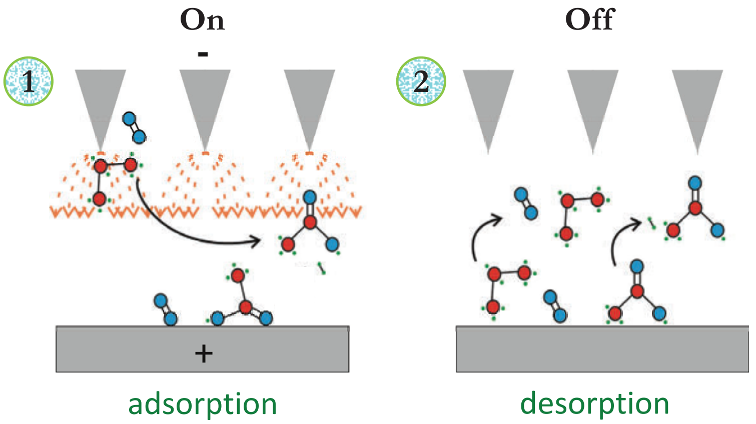

Figure 3. Cross sectional representation of the flow channel in the homemade, silicon-based microreactor with microstructures. In (1) a potential difference is applied and the E-field (represented by the orange arrows) is locally enhanced and adsorption of the reactants is expected. In (2), when the field is switched off (or the polarization is changed), the desorption of the products is expected.

1.3. Why an ATR-IR microreactor?

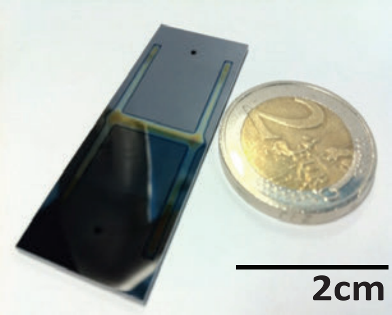

Figure 4. Silicon-based ATR-IR microreactor image with electrodes (gold colored stripes) on both side to apply an electric field across a flow channel.

Microreactor technology has been considered a novel technology for novel chemistry[6] and microreactors are used for different purposes, e.g. organic synthesis[7], catalytic reactions[8] and synthesis of nanoparticles.[9] Many advantages can be cited in the usage of microreactor systems, e.g. small length scales, which is easy to handle and enables coupling to a spectroscopic techniques,[10] large surface to volume ratio, easy to operate in continuous flow, high degree of temperature control and ease of confining small volumes.[6-11]

In this work microreactors are used, because their small dimensions are beneficial to achieve a sufficient E-field strength, since the field strength is inversely proportional to the separation distance of the electrodes. In the design of the microreactor special attention is paid to the integration of an total internal reflection element for ATR-IR[12] (Attenuated Total Reflection Infrared Spectroscopy), which is a power-full tool for investigation of catalytic reactions[13] and other processes that might occur at the interface, allowing *in situ* detection of adsorbed species and reaction products in the liquid or gas phase.[14] A photograph of the homemade microreactor is shown in **Figure 4.**

1.4. Scope and outline of this thesis

In **chapter 2** and **chapter 3** the fabrication of the used microstructures is described. Their use as water and oil repellent surfaces is also described. We investigate their stability against a so called wetting transition. We compare the experimental findings with existing models. Furthermore, the application of these surfaces for colloidal deposition is discussed.

In **chapter 4** a silicon-based microreactor with a configuration that allows in situ analysis by Attenuated Total Internal Reflection Infrared spectroscopy (ATR-IR) of processes driven by an external electrical field (E-field) is presented. The experimental results provide insight into the electronic properties of the device, and into potential application in the initiation of novel chemistry. The fabricated pillar microstructures are integrated into the flow channel of the microreactor and locally densify the electrical field. The interference of these microstructures with the optical behaviour in the IR wavelength region will be presented, and methods to extract valuable chemical information from the microdevices by dealing with these undesired optical side-effects will be discussed.

The goal of ATR-IR is to detect and characterize both adsorbed species as well as product molecules. Any change in the IR spectrum that is caused by other phenomena in the microreactor needs to be identified to ensure correct interpretation. In **chapter 5** the IR spectrum of interstitial oxygen (O_i) defects and phonons in the silicon of the fabricated ATR microreactor is studied. The time course of the induced O_i asymmetric vibration (A_{2u}) during an externally applied E-field is studied. We observe a decrease in the weak ~1727 cm^{-1} absorption band with increasing potential. We evidence the assignment of this peak to the presence of O_i and explain the decrease with increasing voltage as a consequence of temperature via resistive heating of silicon.

In **chapter 6** the ATR-IR microdevice is used to study conformational changes in a non-conductive liquid (i.e. *n*-hexane) upon application of an electrical field. The study opens the possibility to explore the polarization of molecules in liquid phase to control the selectivity of a chemical reaction for fine chemistry purposes.

In **chapter 7** and **Chapter 8** morphological changes on platinum nanoparticles during applying an E-field are studied with CO in a homemade ATR-IR microreactor. CO chemisorption and CO oxidation experiments with and without E-field are performed at different potentials. *In situ* measurements evidence field-driven changes in the CO linear (CO_L), CO bridges (CO_B) and carbonates IR bands. The influence of the presence of an E-field on the CO oxidation is discussed.

1.5. References

(1) Logan, R. S.; *J. Chem. Educ.*, **59**, (1982) 279

(2) Xu, J; Mojet, B. L.; Lefferts, L.; *Microporous and Mesoporous Materials*, **91**, (2006) 187

(3) Xu, J; Mojet, B. L.; van Ommen, G. J.; Lefferts, L.; *J. Phys. Chem. B*, **108**, (2004) 15728

(4) Blatter, F.; Frei, H.; *J. Am. Chem. Soc.*, **116**, (1994) 1812

(5) Kreuzer, H. J.; *Surf. Interface Anal.*, **36**, (2004) 372

(6) Hartman, R. L.; Jensen, F. K.; *Lab on a Chip*, **9**, (2009) 2495

(7) Mason, B. P.; Price, K. E.; Steinbacher, J. L.; Bogdan, A. R.; McQuade, D. T.; *Chem. Rev.*, **107**, (2007) 2300

(8) Jähnisch, K.; Hessel, V.; Löwe, H.; Baerns, M.; *Angew. Chem. Int. Ed.*, **43**, (2004) 406

(9) Abou-Hassan, A.; Neveu, S.; Dupuis, V.; Cabuil, V.; RSC *Advances*, **2**, (2012) 11263

(10) van Bentum, P.J.M.; Janssen, J.W.G.; Kentgens, A.P.M.; Bart, J.; Gardeniers, J.G.E.; *J. of Magnetic Resonance*, **189**, (2007) 104

(11) Frost, C. G.; Mutton, L.; *Green Chem.*, **12**, (2010) 1687

(12) Herzig-Marx, R.; Queeney, K. T.; Jackman, R. J.; Schmidt, A. M.; Jensen, F. K.; *Anal. Chem.*, **76**, (2004) 6476

(13) Mojet, B. L.; Ebbesen, S. D.; Lefferts, L.; *Chem. Soc. Rev.*, **39**, (2010) 4643

(14) Popa, A. M.; Angeloni, S.; Bürgi, T.; Hubbell, J. A.; Heinzelmann, H.; Pugin, R.; *Langmuir*, **26**, (2010) 15356

2

Microreactor fabrication

From superhydrophobic surfaces to electrodes for chemistry

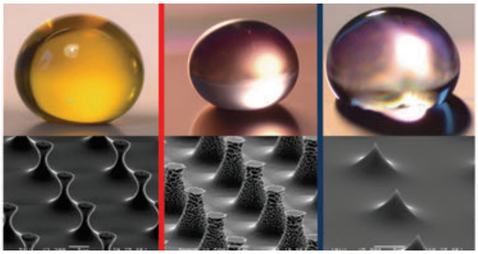

In this chapter we detail the microfabrication method of silicon microelectrodes to enhance the electric field (E-field) strength by changing the shape of the microstructures. The structures are planned to be coupled to an ATR crystal using IR spectroscopy (ATR-IR) to induce and study chemical reactions. The fabrication method of the microstructures is based on careful tuning of the process conditions in a reactive etching protocol. We investigate the influence of SF_6, O_2 and CHF_3 gases during the etching process using the same pitch of the photolithographic mask. Varying the loading conditions during etching, we optimized the conditions to fabricate homogeneous pedestal-like structures. The roughness of the microstructures could also effectively be controlled by tuning the dry plasma etching conditions. Towards further application of such microstructures, we study the wetting behaviour in terms of the water and oil contact angles. Excitingly, the surfaces can be engineered from superhydrophobic to omniphobic by variation of the aforementioned predefined parameters.

This chapter has been published as:

A. Susarrey-Arce, A. G. Marín, S. Schlautmann, L. Lefferts, J. G. E. Gardeniers and A. van Houselt, One-step sculpting of silicon microstructures from pillars to needles for water and oil repelling surfaces, *Micromech. Microeng.*, **23**, (2013) 025004.

T. Tran, H. J. J. Staat, A. Susarrey-Arce, T. C. Foertsch, A. van Houselt, H. J. G. E. Gardeniers, A. Prosperetti, D. Lohse and Chao Sun, Droplet impact on superheated micro-structured surfaces, *Soft Matter*, **9**, (2013)3272. (not included).

2.1. Introduction

Superhydrophobicity[1] and superoleophobicity[2] have attracted particular attention over the last decade, during which new methodologies have become available to establish water, oil or organic solvent repellency.[3-6] Besides the choice of a specific roughness and chemical composition, a good control of the shape of the micro and/or nanofeatures on the surface is critical to achieve these special properties. A surface is superhydrophobic (superoleophobic) when the contact angle (CA) between the water (oil) droplets and the surface is above 150°.[6] Nature-inspired superhydrophobic (superoleophobic) materials with lotus leaf-like micro and nano bumps,[7] and waterstrider leg mimicking features8 have been reported. These artificial surfaces are fabricated via different methods,[9] including plasma etching,[10] soft imprinting lithography,[11] backside 3D diffuser lithography,[12] physical or chemical vapor deposition[13] and electrochemical synthesis.[14]

Reports on combined superhydrophobic and superoleophobic properties in one surface structure in order to establish so-called "omniphobicity" are, however, much scarcer.[15-19] An appealing recent example can be found in the work of Im *et al.* who report the fabrication of inverse trapezoidal polydimethylsiloxane (PDMS) microstructures.20

In the present chapter we will detail the fabrication process and determine the key fabrication parameters to obtain an omniphobic surface.[21, 22] Moreover, in the forthcoming chapters we show that such engineered surfaces can be used as microelectrodes to induce chemical reactions driven by an electric field (E-field) in an ATR-IR microreactor.

2.2. Experimental section

Arrays of microstructures were fabricated by reactive ion etching of a silicon wafer (*p*-type, Boron doped 5-10 Ohm-cm resistivity, 100 mm diameter, 525 μm thickness, {100} crystal orientation; Okmetic Finland) which was covered by a patterned photoresist layer. The OiR 907/17 photoresist was spun on the silicon wafer at 4000 rpm for 30 s. to obtain a layer thickness of 1.7 μm. After a soft-bake step at 95° C for 90 s., the photoresist layer was exposed for 3.5 s. to mid UV light in an EVG 620 mask aligner through a photomask which contained the microstructure array geometry. Subsequently the wafers were immersed for 1 min. OPD-4262 and the patterned resist layer was hard-baked at 120° C for 30 min in air.

The reactive ion etching (RIE) was carried out on two different machines: (1) on an Electrotech Plasmafab 310-340 parallel-plate twin deposition/etch system, and (2) on an Adixen AMS100 SE ICP system. We will refer to these systems as RIE-1 and RIE-2, respectively. The etching time for experiments on RIE-1 was kept constant at 10 min, on RIE-2 at 5 min. The chamber pressure in both systems was set to 75 mTorr. The electrode with the attached silicon substrate was kept at 10° C for RIE-1, and at -50° C for RIE-2, using liquid nitrogen as coolant in the latter system. The gas flows of SF_6 and O_2 during the etching process were used as tuning-variables on both systems, as well as the presence or absence of a plasma shower head (PSH) on RIE-1. The RF plasma power on system RIE-1 and the ICP plasma power on RIE-2 were varied, while on RIE-2 a constant CCP power of 20 W and a source power of 500 W were maintained. A constant CHF_3 flow of 10 sccm was applied in RIE-1. Post to both DRIE-steps the photoresist was removed from the wafers with oxygen plasma cleaning, HNO_3 cleaning, and in 1% HF.

In addition, to achieve smoothening of the sides of the microstructure, 1 μm of SiO_2 was grown by steam oxidation (1150° C). Because oxidized silicon occupies a *ca.* 40% larger volume than unoxidized silicon, this procedure leads to rounding off of the sharp edges of the structures, as illustrated in **Figure 1**. The oxide thickness was controlled carefully to avoid a collapse of the microstructures due to “over-oxidation”.

Schematic representations of the three distinct microstructures, achieved by the varied etch parameters, are sketched in **Figure 1a**: needle-shaped (tapered off upwards) microstructures (a); pedestal-shaped (tapered off downwards) microstructures (b) and pillar-shaped (c).

Finally, the silicon microstructures were coated by vapor deposition in a vacuum system using trichloro (1H, 1H, 2H, 2H-perfluorooctyl) silane (FOTS 97%, Sigma-Aldrich). Contact angle (CA) measurements were carried out at room temperature (21°C), with a relative humidity of 35 % using Dutch water (Millipore Milli-Q system, resistivity: 18.2 MΩ-cm), commercial olive oil, and *n*-octane (99%, Alfa Aesar).

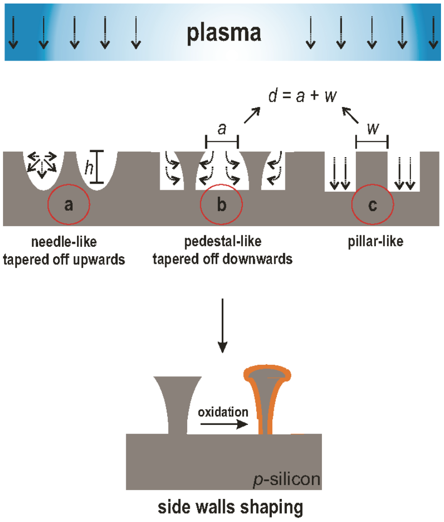

Figure 1. Schematic representation of the microstructure fabrication process. Reactive ion etching is used to tune the microstructure shapes to (a) needle-like with smooth or sharp edges, (b) negative tapered (pedestal-like) structure and (c) straight pillar structure; where *h* is defined as the height of the microstructures, *a* the interspace between adjacent microstructures and *w* the top diameter of the microstructures. An oxidation step to shape the pedestal-like structure from the microstructures in (b) is illustrated and indicated by an arrow.

2.3. Results and discussions

2.3.1. Microstructure shapes obtained with system RIE-1

In order to achieve a good control of the etched silicon microstructures, we varied the gas concentrations of SF_6, O_2 and CHF_3, since these concentrations influence the shape of the microstructures via a synergetic ion-inhibition mechanism. The surface passivation[23] is balanced with the ionic surface bombardment, via the parameters O_2 and SF_6 flow and plasma power.[24, 25] The systematic variations in the SF_6, O_2 and CHF_3, concentrations and the presence of plasma shower head during the etching process for 9 different etching procedures are shown in **Table 1**. In **Figure 2** the resulting microstructures are shown.

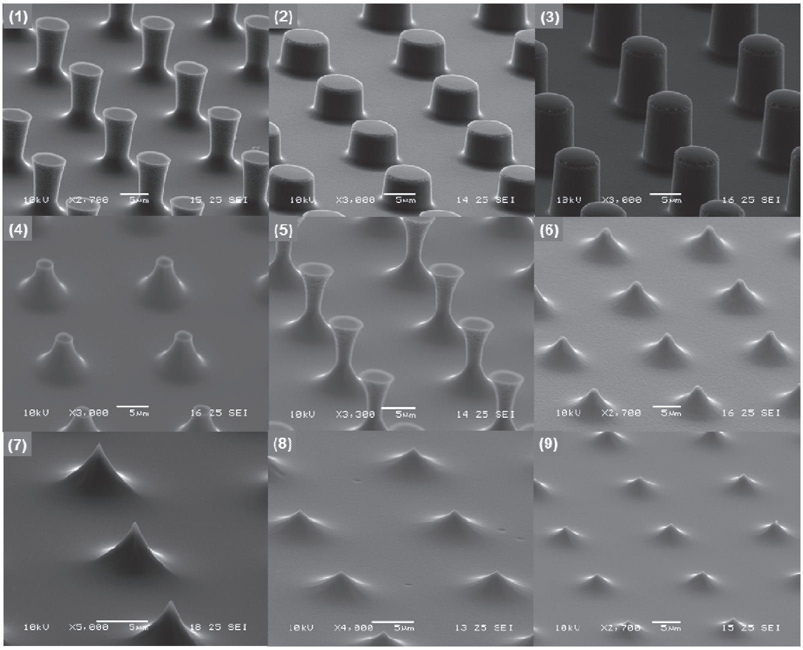

Figure 2. Microstructure patterns made with system RIE-1. In each SEM image the scale bar represents 5 μm. Each inset number is related to the parameters listed in **Table 1**.

Table 1. RIE-1 experimental parameters employed to fabricate the shaped microstructures

Sample **Parameters**	**1**	**2**	**3**	**4**	**5**	**6**	**7**	**8**	**9**
Plasma shower (PSH)	yes	yes	yes	no	no	no	yes	no	yes
O_2 [sccm]	5	20	20	5	5	5	20	20	5
RF power [W]	75	75	150	75	75	150	150	150	150
SF_6 [sccm]	30	30	30	30	50	50	50	50	50

In **Figure 2(1)-(3)** pillar-like microstructures can be observed. The pillars in **Figure 2(1)** are slightly tapered off downwards, while in **Figure 2(2)** and **Figure 2(3)** the pillars are straight. The difference between **Figure 2(1)** and **Figure 2(2)** is the amount of O_2 addition to SF_6/CHF_3 plasma (11 vol% and 33 vol% from the total plasma gas mixture). In addition, the height of the pillars reduces by ~3 μm going from **Figure 2(1)** to **Figure 2(2)**, possibly due to a lower surface coverage with fluorine atoms and which changes the surface chemistry from primarily Si-C to Si-F, and next to Si-O bonding, as the O_2 concentration is increased further (since the SF_6 and CHF_3 contributions to the plasma are changed from 66 vol% and 22 vol% in **Figure 2(1)** to 50 vol% and 16 vol%, respectively, in **Figure 2(2)**). It has also been suggested that a passivation layer of SiO_xF_y leads to a decrease in the etching rate perpendicular to the substrate surface.[26] To develop higher cylindrical microstructures, the conditions are maintained as in **Figure 2(2)**, but the RF plasma power is increased from 75 W to 150 W in **Figure 2(3)**. With these conditions higher and straight pillars are obtained of about 8.55 μm height. The increased RF plasma power also leads to an increase in the silicon etching rate from 0.40 μm/min (in **Figure 2(2)**) to 0.85 μm/min. (in **Figure 2(3)**). Without a plasma shower head (**Figure 2(4)**) the etching is more isotropic (then with a PSH, **Figure 2(1)**), resulting in microstructures which are tapered off upwards with a top diameter of ~ 1.2 μm against 2.3 μm in the case of **Figure 2(1)**).

An increase in the SF_6 flow to 50 sccm, while the other parameters in **Figure 2(4)** are kept constant, leads to pillars with well-defined smooth concave sides (**Figure 2(5)**). These 'pillars' have an overhanging top plateau. The angle between their sides and the top surface (measured in the dense phase) is ~60º.

In **Figures 2(5) – 2(9)** the combination of the increased SF_6 flow and the other preparation parameters (presence of a PSH, O_2 and CHF_3 flow and RF power) leads to faster (compared to **Figure 2(4)**) and isotropic etching, which results in sharp tips. The increased vertical and lateral etching rates originate possibly from a thinner passivation layer, due to a higher surface coverage with fluorine atoms, which leads to primarily Si-C surface chemistry, as discussed above. The maximum height difference between the sharp needles (between **Figure 2(7)** and **Figure 2(9)**) is ~0.7 μm. The result of a subsequent steam oxidation step of the microstructures shown in **Figure 2(5)**, is shown in **Figure 3**. The interfaces of these pedestal-like microstructures are more smooth after the oxidation step.

Compared to reported omniphobic,[27, 28] or superhydrophobic[29] similarly micropatterned[30,10] Si surfaces, our procedure results in a very precise control of the surface structure and interface smoothness, which enables one to verify systematically the influence of both surface roughness and edge-curvature on the wetting properties of these surfaces.[22]

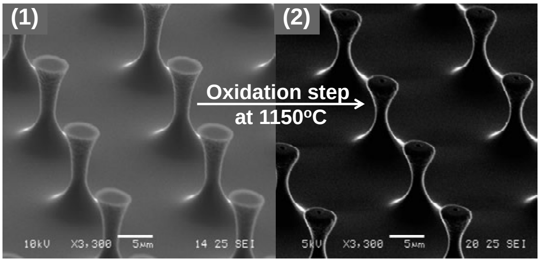

Figure 3. SEM image of the pedestal-like structures, before and after the thermal oxidation process.

2.3.2. Microstructure shapes obtained with system RIE-2

Microstructures grown in the RIE-2 system were fabricated using a SF_6 flow of 100 sccm, a CCP power of 20 W and a source power of 500 W, without plasma shower head. The effect of the addition of O_2 to the plasma was systematically investigated (see **Figure 4(1)-(5)**). Due to the high SF_6 concentration, the microstructures in **Figure 4(1)** are mainly needle-like. An increase in the O_2 flow in **Figure 4(2)-(5)** results in more anisotropic etching, in combination with a lower etching rate. In **Figure 4(2)** the sides of the pillars are composed of porous nanoflakes. In **Figure 4(4)** some small needles are present on the surface in between the micropillars, suggesting the presence of "black silicon" at higher O_2 concentrations. In fact, **Figure 4(5)**, a field of nanograss, "black silicon",[25] is obtained at 50 sccm O_2 flow. **Figure 4(6)**, shows square microtables with rough, porous sidewalls. The square nature arises from crystal-orientation dependent etching, due to the relatively low influence of ion bombardment under these conditions, an effect that has been reported before for similar conditions.[24]

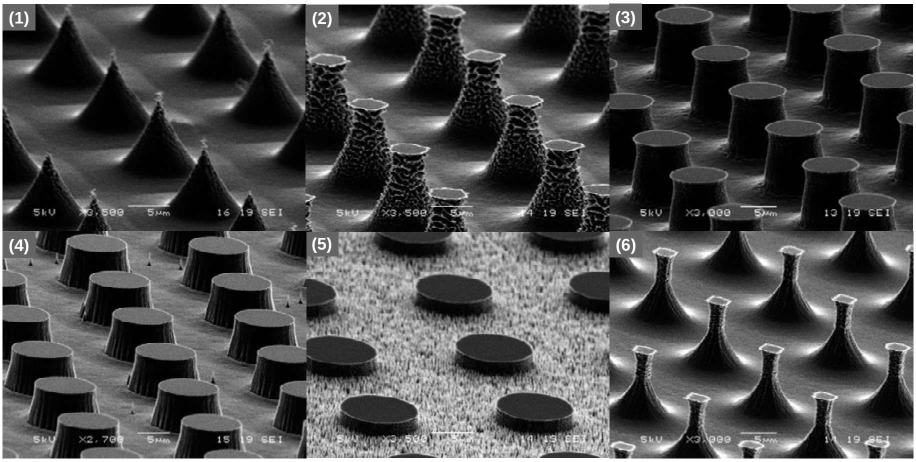

Figure 4. Microstructure patterns made with system RIE-2. In each SEM image the scale bar represents 5 μm. The O_2 flow used in the etching process was as follows; (1) 17.5 sccm, (2) 20 sccm, (3) 25 sccm, (4) 35 sccm and (5) 50 sccm for 5 min. Sample (6), was processed in two steps, 25 sccm for 2.5 min, followed by 15 sccm for 2.5 min.

2.3.3. Wetting behavior of the fabricated structures

For the case when a liquid wets only the top of the microstructures on the surface, leaving air underneath the droplet between the microstructures, Cassie and Baxter formulated an equation for the apparent contact angle θ^* in terms of the contact angle θ on the chemically equivalent flat surface: $\cos\theta^* = -1 + \Phi_s (1 + \cos\theta)$, where Φ_s is the fraction of the top-surface area of the microstructures from the total surface area,[31] or, in other words, the top-area packing fraction. In **Figure 5**, we show the top-area packing fraction Φ_s, calculated as $(\pi/4)(w/d)^2$, as function of h/w. (h, w and d as defined in **Figure 1** for the fabricated microstructures). The points in **Figure 5** follow essentially a hyperbola (indicated by the solid line), since Φ_s, which is proportional w^2, is plotted against h/w. The points above the dotted line ($\Phi_s > 0.01$) in **Figure 5** are accompanied by superhydrophobic behavior, as evidenced in **Figure 6(1)-(5)**. The points below the dotted line ($\Phi_s < 0.01$) are accompanied by lower contact angles (see for instance **Figure 6(6)**), most probably because the droplets are not in the Cassie-Baxter state on these sharp needles. These observations are in agreement with other studies with observed droplets in the Cassie-Baxter state for values of Φ_s around 0.02[31] to 0.20.[33] In addition, it is important to note that it is possible to change the top-area packing fraction Φ_s, even when the pitches of the masks are identical, by use of the so called loading effects in RIE.[24]

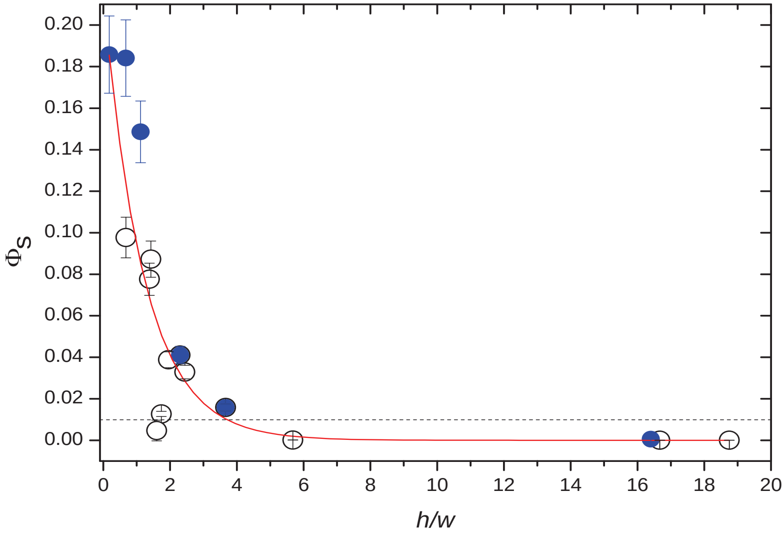

Figure 5. Pillar density Φ_s as function of *h*/*w*. Microstructures fabricated by RIE-1 are shown as open circles and microstructures fabricated by RIE-2 are shown as closed circles.

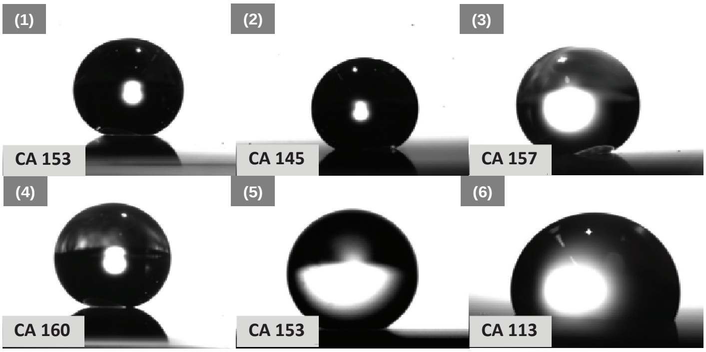

Figure 6. Side photographs of water droplets on the surfaces fabricated by RIE-1. The numbers correspond to the numbers in **Figure 2**. The contact angle value is shown in the inset.

Furthermore, in addition to superhydrophobicity, some of the fabricated microstructures also exhibit superoleophobicity, repelling both water and oil very effectively, as evidenced by the photographs of drops of water, olive-oil and *n*-octane on the substrate in **Figure 7**.

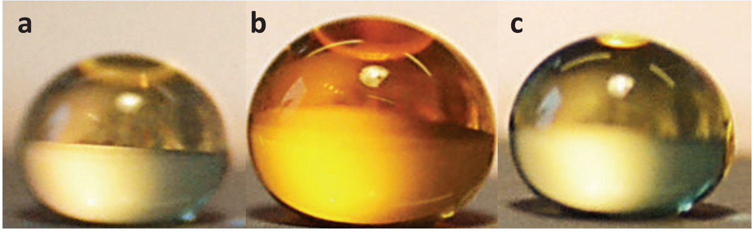

Figure 7. Side-photographs of droplets of (a) *n*-octane (left, σ_t = 21.6 mN/m), (b) water (middle, σ_t = 72.8 mN/m), and (c) olive oil (right, σ_t = 32.5 mN/m) on a negatively tapered substrate made by RIE-2, similar to **Figure 4(2)**. In all cases the contact angle is ~160°.

This, so called 'omnipobicity' could be related to the re-entrant surface curvature, or, in other words, the "over-hanging" microstructures.[20] The substrates, which show omniphobicity also show a remarkable stability against the wetting transition during water evaporation.[22] In comparison with most other fabrication methods for omniphobic surfaces, which were recently reported by N. Wilke et al., T. Wu et al., and A. Tuteja et al.,[16, 27, 28, 34] the control of the surface roughness of the micropillars, which is shown to have an influence on the wetting properties[22] is well controlled in our method. Recently, also H. Zhao et al. reported the microfabrication of oil repellent surfaces[19] with a well-controlled side roughness.

In short, by controlling effectively the top width of the prepared microstructured surfaces, we were able to produce superhydrophobic, and in some cases even omniphobic surfaces. RIE-1, reveals more control in the microstructure shape and less rough surfaces compared to RIE-2. A possible explanation is due to the presence of CHF_3 in the plasma in RIE-1 (in contrast to RIE-2) which leads to lower etching rates.[35] The absence of CHF_3 in RIE-2, resulting in moresurface roughness, leads to the absence of an evaporation transition on omniphobic surfaces as described in reference.[22]

2.4. Conclusions

Two silicon dry etching methods to create various microstructures by varying the gas loading during RIE using a single mask-layer etching procedure were described. The edges and shapes were well-controlled by varying the O_2/SF_6 gas loading, the plasma power and the presence of a plasma shower head. This method allows the growth of many different shapes, like pillars, needles, tipi's and pedestals, with one mask. In both cases, the more pillar-like microstructured surfaces exhibit hydrophobic, and in some case even omniphobic behavior.

2.5. References

(1) Quéré, D.; *Annual Review of Materials Research* **38**, (2008) 71

(2) Hsieh, C.-T.; Wu, F-L.; Chen, W.-Y.; *Materials Chemistry and Physics* **121**, (2010) 14

(3) Liu, M.; Liu, X.; Ding, C.; Wei, Z.; Zhu, Y.; Jiang, L.; *Soft Matter* **7**, (2010) 4163

(4) Yao, X.; Gao, J.; Song, Y.; Jiang, L.; *Adv. Funct. Mater.* **21**, (2011) 4270

(5) Im, M.; Im, H.; Lee, J.-H; Yoon, .J.-B.; Choi, Y.-K.; *Langmuir* **26(22)**, (2006) 17389

(6) Li, X.-M.; Reinhoudt, D.; Crego-Calama, M.; *Chem. Soc. Rev.* **36**, (2007) 1350

(7) Bhushan, B.; Jung, Y. C.; *Nanotechnology* **17**, (2006) 2758

(8) Zhang, X.; Zhao, J.; Zhu, Q.; Chen, N.; Zhang, M.; Pan, Q.; ACS *Appl. Mater. Interfaces* **3**, (2011) 2630

(9) Fürstner, R.; Barthlott, W.; *Langmuir* **21**, (2005) 956

(10) Azimi, S.; Sandoughsaz, A.; Amirsolaimani, B.; Naghsh-Nilchi, J.; Mohajerzadeh, S.*; J. Micromech. Microeng.* **21**, (2011) 074005

(11) Wu, D.; Wu, S.-Z.; Chen, Q.-D.; Zhang, Y.-L.; Yao, J.; Yao, X.; Niu, L.-G.; Wang, *et al. Adv. Mater.* **23**, (2011) 545

(12) Lee, J.-H.; Choi, W.-S.; Lee, K.-H.; Yoon, J.-B.; *J. Micromech. Microeng.* **18**, (2008) 125015

(13) Zhang, X.; Shi, F.; Niu, J.; Jiang, Y.; Wang, Z.; *J. Mater. Chem.* **18**, (2008) 621

(14) Zhao, N.; Shi, F.; Wang, Z.; Zhang, X.; *Langmuir* **21(10)**, (2005) 4713

(15) Meng, H.; Wang, S.; Xi, J.; Tang, Z.; Jiang, L.; *J. Phys. Chem. C* **112**, (2008) 11454

(16) Tuteja, A.; Choi, W.; Ma, M.; Mabry, J. M.; Mazzella, S. A.; Rutledge, G. C.; McKinley, G. H.; Cohen, R. E.; *Science* **318**, (2007) 1618

(17) Wu, W.; Wang, X.; Wang, D.; Chen, M.; Zhou, F.; Liu W.; Xue, Q.; *Chem. Commun.* **1043**, (2009) 1043

(18) Cao, L.; Price, T. P.; Weiss, M.; Gao, D.; *Langmuir* **24**, (2008) 1640

(19) Zhao, H.; Law, K.-Y.; Sambhy, V.; *Langmuir* **27**, (2011) 5927

(20) Im, M.; Im, H.; Lee, J.-H.; Yoo, J.-B.; Choi, Y.-K.; *Soft Matter* **6**, (2010) 1401

(21) Marín, A. G.; Gelderblom, H.; Susarrey-Arce, A.; van Houselt, A.; Lefferts, L.; Gardeniers, H.; Lohse, D.; Snoeijer, J. H.; *Proc. Natl. Acad. Sci.* **109**, (2012) 16455

(22) Susarrey-Arce, A.; Marín, A. G., Nair, H.; Lefferts, L.; Gardeniers, J.G.E.; Lohse, D.; van Houselt, A.; *Soft Matter* **8**, (2012) 9765

(23) Oehrlein, G. S.; Robey, S. W.; Lindström, J. L.; *Appl. Phys. Lett.* **52**, (1988) 1170

(24) de Boer, M. J.; Gardeniers, J. G. E.; Jansen, H. V.; Smulders, E.; Gilde, M.-J.; Roelofs, G.; Sasserath, J. N.; Elwenspoek, M.; *J. Microelectromech. Syst.* **11(25)**, (2002) 385

(25) Jansen, H.; de Boer, M.; Legtenberg, R.; Elwenspoek, M.; *J. Micromech. Microeng.* **5**, (1995) 115 (26)

(26) Legtenberg, R.; Jansen, H.; de Boer, M.; Elwenspoek, M.; *J. Electrochem. Soc.* **6(142)**, (1995) 2020

(27) Tuteja, A.; Choi, W.; Mabry, J. M.; McKinley, G. H.; Cohen, R. E.; *Proc. Natl. Acad. Sci.* **105**, (2008) 18200

(28) Wu, T.; Suzuki, Y.; *Sensors and Actuators B* **156**, (2011) 401

(29) Cao L., Hu, H.-H.; Gao, D.; *Langmuir* **23**, (2007) 4310

(30) Knizikevicius, R.; Kopustinskas, V.; *Vacuum* **77**, (2004) 1

(31) Cassie A.; S. Baxter, S.; *Trans. Faraday Soc.* **40**, (1944) 546

(32) Reyssat, M.; Yeomans, J. M.; Quéré, D.; *Eur. phys. letters* **81**, (2008) 26006

(33) Tsai, P.; Lammertink, R. G. H.; Wessling, M.; Lohse, D.; *Phys. Rev. Lett.* **104**, (2010) 116102

(34) Wilke, N.; Hilbert, C.; Brien, J. O'.; Morrissey, A.; *Sensors and Actuators A* **123-124**, (2005) 319

(35) Jansen, H.; Gardeniers, H.; de Boer, M.; Elwenspoek, M.; Fluitman, J.; *J. Micromech. Microeng.* **6**, (1996) 14

3

E-field electrodes

Towards the design of omniphobic surfaces and its applications

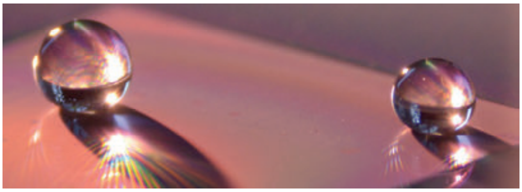

Surfaces that exhibit contact angles close to 180° for both polar and non-polar solvents are rare. Here we report the fabrication of such "omniphobic" surfaces by photolithography (see left-side picture). We investigate their stability against a so called wetting transition during evaporation of millimetric water droplets by systematically varying the shape and surface roughness of the micropillars on the surface. We show that a smooth curvature of the top of the micropillars strongly delays the transition, while it completely disappears when the surface roughness is increased. We compare these experimental findings with existing models that describe the Cassie-Baxter to Wenzel transition and conclude that new models are needed which include the hurdle of an energy barrier for the wetting transition. Our results reveal that by increasing the roughness of the micropillars we do not affect the apparent equilibrium contact angle of the droplets. The dynamic robustness of the surface is, however, dramatically enhanced by an increase of the surface roughness. Furthermore, an application of these surfaces for colloidal deposition is described.

Parts of this chapter has been published as

A. Susarrey-Arce, Á. G. Marín, H. Nairs, L. Lefferts, J.G.E. Gardeniers, D. Lohse and A. van Houselt, Absence of an evaporation-driven wetting transition on omniphobic surfaces, *Soft Matter*, **8**, (2012) 9765, (*Cover article and highlighted by the press*).

Á. G. Marín, H. Gelderblom, A. Susarrey-Arce, A. van Houselt, L. Lefferts, J. G. E. Gardeniers, D. Lohse and J. H. Snoeijer, Building microscopic soccer balls with evaporating colloidal fakir drops, *Proc. Natl. Acad. Sci.*, **109**, (2012) 16455 (*Highlighted by the press*).

3.1. Omniphobicity

Superhydrophobic surfaces are extremely water repellent,[1] and contact angles above 150° have been reported. Inspiration for artificial superhydrophobic surfaces is found in nature: lotus leaves,[2] gecko feet,[3] and the legs of the water strider[4] are natural superhydrophobic surfaces. A myriad of applications of superhydrophobic surfaces have been reported, including self-cleaning,[5] drag reducting,[6,7] anti-freezing[8] and selective condensation surfaces.[9]

Surfaces which are not only superhydrophobic, but also exhibit high contact angles (>150°) with other liquids than water, like oils and alkanes, are even more intriguing. Oil-repelling surfaces are known as oleophobic surfaces and are, for example, used as coatings to repel oily fingerprints on the screens of smartphones. Surfaces which combine superhydrophobicity and superoleophobicity are referred to as “omniphobic”. However, omniphobic surfaces are rare.[10, 11-15]

Superhydrophobic surfaces usually combine a low surface energy with surface texture, comprised of microstructures. The influence of the surface microstructures on the apparent contact angle of droplets is usually explained by the Wenzel model,[16] when the liquid fully fills the space between the surface microstructures, or by the Cassie-Baxter model,[17] when the liquid lays on top of the microstructures, leaving air in between the microstructures under the droplet. In the case of complete wetting Wenzel proposed that the apparent (macroscopic) droplet contact angle θ^* is influenced by the increase of the wetted area (compared to a droplet on a flat surface):

$$\cos \theta^* = r \cos \theta$$ (**Equation 1**),

where r is the ratio of the wetted surface to the projected at surface under the droplet and θ is the equilibrium contact angle on a flat, homogeneous surface, given by Young's equation

($\cos\theta = (\sigma_{sv}-\sigma_{sl})/\sigma_{lv}$, where σ is the interface tension between the solid (*s*), liquid (*l*) and vapour (*v*) phase). Usually, the contact angle hysteresis is high in the Wenzel state (hereafter W), due to the strong contact-line pinning at the microstructures.[1]

In contrast, when the droplet sits on a composite surface of air and a hydrophobic solid, Cassie and Baxter derived an equation for the apparent (macroscopic) droplet contact angle θ^*:

$$\cos\theta^* = -1 + \phi_s (1+ \cos\theta)$$ (**Equation 2**),

where ϕ_s is the fraction of the liquid interface that is in contact with the superhydrophobic solid. In the Cassie Baxter or "Fakir" state (hereafter CB), droplets can easily roll off, often referred to as "self-cleaning".[18] However, it have been found[19] that none of the mentioned equations describes the actual contact angle generally correctly.

The CB state is commonly accepted to be metastable[1] and there have been several recent reports on the CB to W wetting transitions in droplets on microstructered surfaces.[20-33] The CB to W transition can occur spontaneously,[20-23] or can be triggered by, for instance, rapid deceleration,[23] application of an electrical voltage,[24] drop impact,[25, 26] vibration of the substrate,[27, 28] droplet squeezing,[29] or evaporation.[30-32] On the other hand, the CB to W transition is not always observed in evaporating droplets.[34] Reyssat *et al.*,[32] for instance, reported that the CB to W transition is not occurring on surfaces with arrays of high micropillars with aspect ratios > 10. In order to model the experimental data for the evaporation-driven CB to W transition, two approaches are reported. One, in which the increase in the Laplace-pressure inside the evaporating droplet causes the CB to W transition, was successfully tested for long and thin micropillars with relatively large mutual interspaces.[32, 35, 36] And one, based on comparison of the global interfacial energies for the CB and the W state,[20-22, 30, 36-39] was successfully applied for shorter and thicker micropillars with relatively small mutual interspaces.[20-22, 30]

Here, we report the fabrication of new superomniphobic surfaces, on which water droplets preserve the CB state their entire lifetime during evaporation. We compare this evaporation process to water droplet evaporation on superhydrophobic surfaces with nanostructures of similar dimensions, and we examine the applicability of the interfacial energy argument to describe the CB to W transition on these surfaces.

3.2. Experimental section

The fabrication method of the microstructures and the coating of the surfaces are described in **chapter 2**. The dimensions of the microstructures on the studied substrates are given in **Table 1**.

Contact angle measurements during evaporation were performed at room temperature (21 ± 1 °C with a relative humidity of 35 ± 5%, placing a water droplet of 2-6 μL on the microstructured substrate. The used water (18.2 MΩ cm) was purified in a Millipore Milli-Q system, which involves reverse osmosis, ion-exchange, and filtration steps. Side videos were captured via a CCD camera equipped with 420× magnifying lenses and with a recording time of 1-2 frames per second. The equilibrium contact angle on a FOTS coated plane Si(001) wafer was 110 °. The contact angle values on all samples were reproducible within three months after sample fabrication.

Evaporation experiments with drops containing a colloidal suspension of spherical polystyrene were carried out by allowing a water droplet containing polystyrene particles (1 μm diameter, initial concentration 0.08% weight and initial volume 5 μL) to evaporate on the superhydrophobic surface at room temperature and 30% of humidity. After a typical evaporation time of 45 min, the solvent is completely evaporated and only the colloids are left upon the substrate.

Table 1. Height (*h*), pillar-to-pillar nearest neighbor interspace (*a*) and diameter (*w*) of the microstructures on substrates A-D.

Microstructure	***h* (μm)**	***a* (μm)**	***w* (μm)**
A	8.8	14	3.6
B	7.8	14	4
C	9.2	13.5	5.4
D	8.8	14.5	2.4

3.3. Results and discussion

3.3.1. Samples and contact angles

A photograph of droplets of *n*-octane (σ_{lv} = 21.6 mN/m), water (σ_{lv} = 72.8 mN/m) and olive oil (σ_{lv} = 32.5 mN/m) on one of our microstructured omniphobic surfaces (which is labeled as surface C) is shown in **Figure 1**. All droplets exhibit a similar contact angle (~160°), which clearly illustrates the substrate's omniphobicity. We fabricated a series of different microstructured substrates, the only difference being the edge-sharpness and surface roughness. The resulting microstructures, labeled A-D, are shown in **Figure 2** A-D. Their height (*h*), interspacing (*a*) and top diameter (*w*) were all in the same range, see **Table 1**.

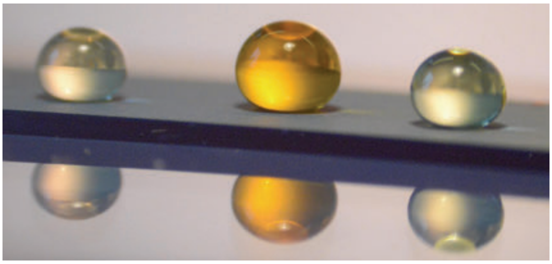

Figure 1. Demonstration of the omniphobicity of substrate C. Droplets of *n*-octane (left, σ_{lv} 21.6 mN/m), water (middle, σ_{lv} = 72.8 mN/m) and olive oil (right, σ_{lv} = 32.5 mN/m), showing contact angles of ~160° on this substrate.

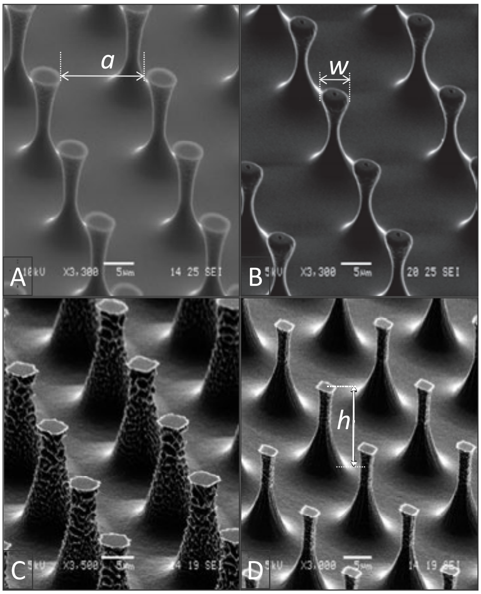

Figure 2. SEM micrographs of the surfaces A-D. In each image the scale bar represents 5 μm.

The microstructures were placed on a square lattice with periodicity $d = a + w$ and the surface packing fraction of the structures, Φ, was of the order of 5%. The sides of the micropillars on samples A and B were smooth at the micro-scale (see **Figure 2**), while the side of the micropillars on samples C were porous, giving rise to roughness at the micro-scale. On sample D the sockets of the pillars were smooth at the micro-scale, while their upper half was slightly porous. The edges of the pillars in sample A were very sharp (radius of curvature « 1 μm), while the edges on sample B were more rounded (radius curvature ≈ 1 μm). On samples C and D the top plateaus of the pillars exhibit frayed, sharp edges (radius of curvature « 1 μm).

On all samples the contact angles for water, olive oil and *n*-octane were found to be 150º (± 5º), 155º (± 5º) and 155 (± 5º), respectively. In all cases the contact angle hysteresis was limited to less than 10 degrees. The omniphobicity of substrates A-D could be related to the re-entrant surface curvature, or, in other words, the "over-Hanging" microstructures. According to

Tuteja *et al.*,[10] such multivalued surface topography does indeed result in superhydrophobicity and superoleophobicity.

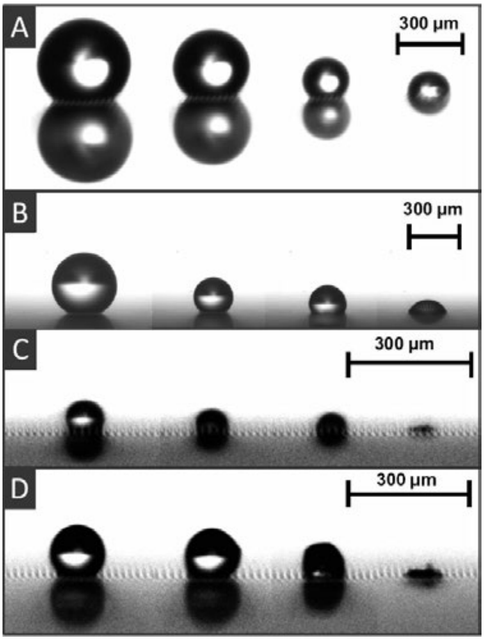

Figure 3. Snapshots of the side views of an evaporating water droplet on the microstructured substrates A-D. The droplet on sample A is in the CB state with a high contact angle in the first three snapshots, while in the last snapshot the droplet is in the W state. The droplet on substrate B is in the CB state in the first two snapshots and has undergone the CB to W transition in the last two snapshots. On substrates C and D the droplet stays in the CB state for its entire lifetime. Note that light and the microstructures are visible under the droplet when it is in the CB state and not when it is in the W state.

3.3.2. Evaporation of water droplets

The evaporation of water droplets with initial volumes ranging from 2 to 6 μL was filmed from the side. Snapshots of side view images of the evaporating droplets are shown in **Figure 3**. Several experiments were performed for each surface, with reproducible results. For substrates A and B a transition from the CB state to the Wenzel state is clearly visible. On substrate A the droplet was in the CB state for the first 3 images (note the light between the droplet and the surface microstructures), while in last snapshot the droplet has undergone the CB to W transition: the contact angle dropped from ~140° to ~80° and there was no light visible under the droplet, since the water filled the space between the droplet and the surface microstructures. Such a transition was also observed between the first and the last two snapshots of the droplet on substrate B. For substrates C and D the transition was not observed in the side view images at all.

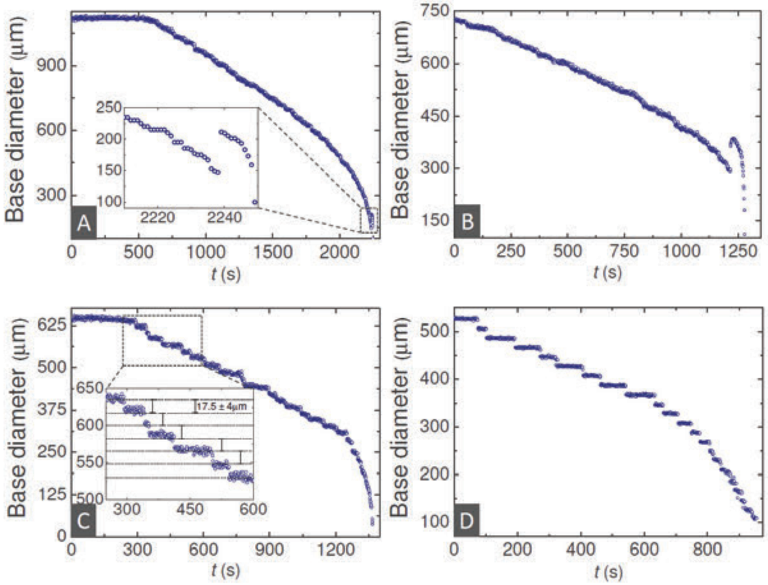

Figure 4. Base diameter of the evaporating water droplets on the substrates A-D, extracted from the side views, as a function of time.

From the side view images we extracted the height, the base radius, and the contact angle of the droplet as a function of time. The base diameter of the evaporating droplets on the substrates A-D is shown in **Figure 4** as a function of time. The evaporation time on the substrate A-D differs due to different initial volumes of the evaporating droplets. The CB to W transition on samples A and B is visible as a sudden increase in the base diameter: on sample A the base diameter increased from ~146 μm to 211 μm at *t* = 2240 s (see the inset in **Figure 4A**) and on sample B the base diameter increased from ~300 μm to 375 μm at *t* = 1220 s. On samples C and D such a sudden increase was not observed. Pinning of the contact-line leads to a stepwise retraction from pillar to pillar, which shows up as distinct plateaus in the base diameter as a function of time in **Figure 4C** and **D**. The step size between subsequent plateaus corresponds with the interspacing between the microstructures (= *d* ± *w*).

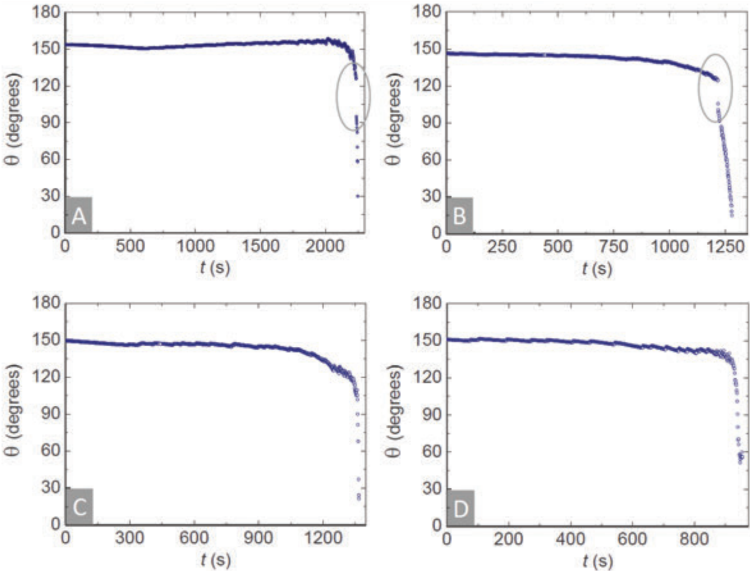

Figure 5. Contact angle θ of the evaporating water droplets on the substrates A-D, extracted from the side views, as a function of time. The CB to W transitions on substrates A and B are marked by the grey ellipses.

3.3.3. Evaporation of a colloidal solution

The contact angle of the evaporating droplets on the substrates A-D is shown in **Figure 5** as a function of time. The CB to W transition on samples A and B is noticeable as a sudden drop in the contact angle (marked by the grey ellipses). On samples C and D such a sudden drop is not observed. One could argue that the transition from the CB to the W state on substrates C and D may happen when the size of the droplet is beyond the resolution of our camera. To test this hypothesis we performed evaporation experiments with a colloidal suspension of spherical polystyrene particles of 1 μm in diameter. After evaporation, the polystyrene particles were exclusively found on top of the microstructures (see **Figure 6**), which shows that the droplet was in the CB state, sitting on top of the microstructures, during its entire lifetime. In contrast, we found the polystyrene particles all over the surface in cases where a CB to W transition occurred.

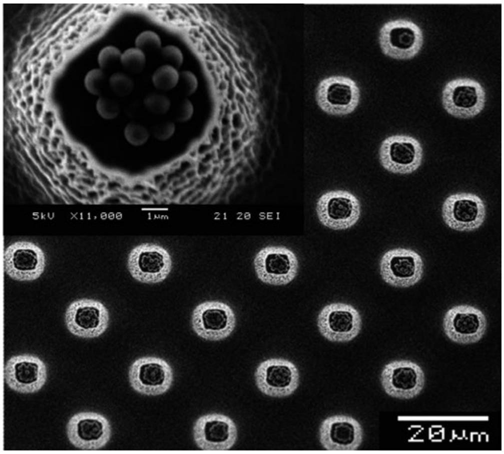

Figure 6. SEM micrographs of substrate C after evaporation of a droplet containing a colloidal suspension of polystyrene particles. After evaporation of the water, the particles are exclusively found on top of the microstructures, demonstrating that the droplet remained on top of the pillars during the entire evaporation process. The inset shows a zoom-in on a single micropillar with the polystyrene particles on top of the pillar.

3.3.4. Comparing with mechanisms from literature

We compare our experimental data with the transition mechanisms proposed in literature. For a Laplace-pressure driven mechanism the moment of transition will, for nanostructures of similar dimensions, be totally determined by the droplet size. Reyssat *et al.*[32] proposed that for a Laplace- pressure driven transition the transition will occur when the droplet radius $R < a^2/h$.

For our samples (with comparable *a* and *h* values) this corresponds to a critical radius of ~22 ± 3 μm. For sample A we observed the CB to W transition when the base diameter was ~150 μm. At that moment the drop had a radius of ~90 μm, corresponding to a Laplace-pressure of ~1.6 kPa. For sample B we observed the CB to W transition when the base diameter and radius were ~300 μm and ~180 μm, respectively, corresponding with a Laplace-pressure of ~0.8 kPa. In samples C and D the transition was never observed, even for very small droplet sizes (high Laplace-pressures). The CB to W transition can therefore not be fully described by a Laplace-pressure driven mechanism.

Next we discuss the validity of a global interfacial energy argument[20 – 22, 30] to describe the CB to W transition. This argument is based on comparison of the interfacial energies E_{CB} and E_W for the CB and the W states during the evaporation process. The total interfacial energy E_{CB} or E_W is the sum of the creation energies of all interfaces. Thus, $E_W = A_{sl}\sigma_{sl} + A_{lv}\sigma_{lv}$ and $E_{CB} = A_{sl}\sigma_{sl} + A_{sv}\sigma_{sv} + A_{lv}\sigma_{lv}$, where A is the interfacial area and the indices *s*, *l* and *v* indicate, as earlier the solid, liquid and vapour phase, respectively. We used σ_{lv} = 72.8 mN/m for the droplet-air interface and σ_{sv} = 12 mN/m for the FOTS coated SiO_2 surface.[40] Following the approach of Tsai *et al.*,[30] the interface tension σ_{sl} is estimated by a force balance at the contact line using a modified version of Young's equation: $\sigma_{sl} = \sigma_{sv}\text{-}\sigma_{lv} \cos \theta^*$. θ^* was determined from the side view images of the evaporating droplets.

We illustrate this global interfacial energy argument with an example of water droplet evaporation on a substrate with straight micropillars (see the inset in **Figure 7** for a SEM image of the surface). These micropillars have similar height, interspacing and diameter as structures A-D, without added curvature and roughness. The blue open circles in **Figure 7** show the base diameter of the evaporating droplet as a function of time. The CB to W transition occurred at *t* = 2300 s when the base diameter had increased from 395 μm to 483 μm. This moment is marked by the vertical line and the grey ellipses. Using the base diameter and the contact angle as extracted from the side view images we calculated E_{CB} and E_W for each moment of the droplet's lifetime. The energy difference E_{CB}-E_W is plotted as the closed triangles in **Figure 7**. From the beginning of the evaporation process until t = 2300 s the energy difference E_{CB}-E_W is negative, since the CB state has a lower energy than the W state and, hence, the droplet is in the CB state. After t = 2300 s the W state has the lowest energy. The CB to W transition is occurring when E_{CB} = E_W, i.e. at t = 2300 s, which is exactly the moment when the CB to W transition is observed in the side view images of the droplet.

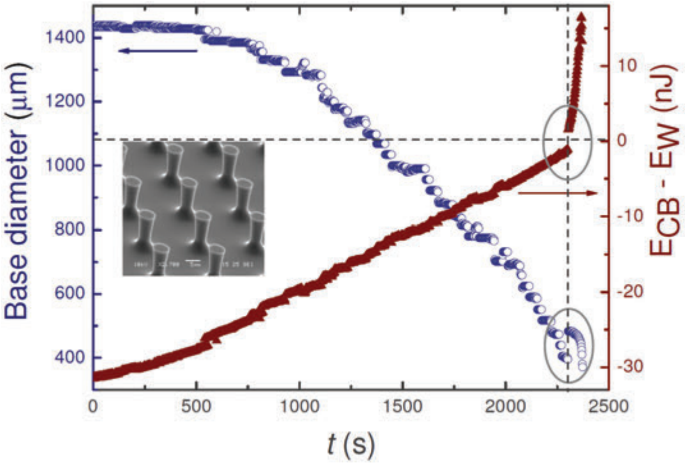

Figure 7. Illustration of the global interfacial energy argument on a substrate containing micropillars with straight interfaces and sharp edges (see the inset for a SEM micrograph). The open circles (referring to the left-hand ordinate) represent the base diameter of the evaporating water droplet as a function of time. The closed triangles (referring to the right-hand ordinate) show the calculated interfacial energy difference E_{CB}-E_W. The horizontal line is positioned at E_{CB}-E_W = 0 and the vertical line marks the time when the CB to W transition occurs, exactly when E_{CB}-E_W = 0.

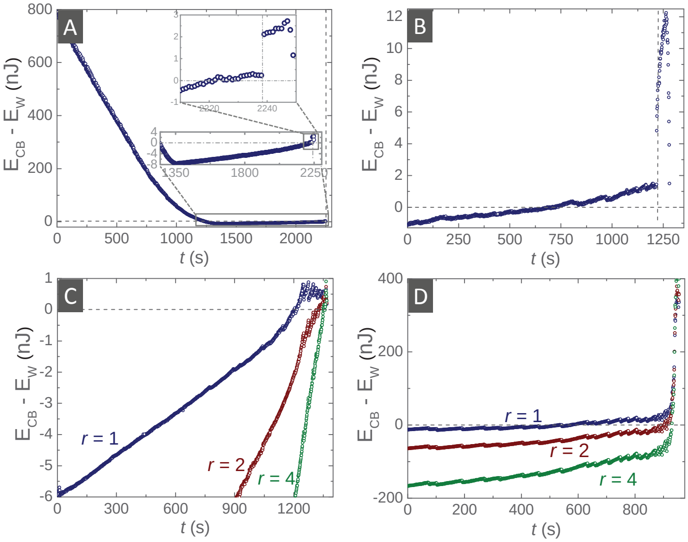

Figure 8. Calculated interfacial energy difference E_{CB}-E_W for the evaporating water droplets on the substrates A-D as a function of time. The vertical lines in graph A and B mark the time when the CB to W transitions occur. For substrates C and D the exact surface roughness on the sides of the pillars is unknown. The energy difference E_{CB}-E_W is calculated for three roughness values, namely $r = 1$ (blue), $r = 2$ (brown) and $r = 4$ (green). The dotted horizontal lines are positioned at E_{CB}-$E_W = 0$.

Figure 8 displays the calculated energy difference E_{CB}-E_W for the evaporating droplets on the substrates A-D as a function of time. For the droplet on substrate A the energy difference E_{CB}-E_W is positive until $t = 1250$ s, indicating that in this period the W state has the lowest energy. This observation is in agreement with findings of Kwon *et al.*[23] for larger droplets. From $t = 1250$ s until $t = 2220$ s, the energy difference E_{CB}-E_W is negative, while from $t = 2220$ s, the CB state becomes lower in energy again. Note that the CB to W transition occurred at $t = 2238$ s on substrate A. The calculated lowest energy state in the initial stages of the droplet evaporation on substrates B-D is the CB state. During the evaporation process of each droplet, the calculated energy difference E_{CB}-E_W equals zero at some moment. This moment is, however, not in agreement with the experimentally observed CB to W transition on substrates A and B and with the absence of a transition on substrates C and D. Note that for substrates C and D the exact surface roughness of the walls of the micropillars is unknown. Calculations were therefore performed at different roughness values, namely for $r = 1$, $r = 2$ and $r = 4$, with r defined as in **Equation 1**. In all cases the calculated energy difference E_{CB}-E_W goes through zero during the evaporation of the droplet, but no CB to W transition is experimentally observed.

3.3.5. The global energy argument crises

The presented global interfacial energy argument obviously fails to predict the CB to W transitions on our substrates: For the droplet on substrate A it predicts the CB to W transition at $t = 2220$ s, while in the earlier stages of the evaporation process (from $t = 0$ to $t = 1250$ s), the W state was calculated to be the lowest in energy. Experimentally it was observed that the droplet was in the CB state till $t = 2238$ s. For the droplet on substrate B the global interfacial energy argument predicts a transition at $t = 650$ s, while the observed transition occurred at $t = 1220$ s. For the droplets on substrates C and D the all the calculations predict a CB to W transition, while such a transition was never observed on these substrates.

Why is the global interfacial energy argument, as presented above, insufficient to explain the experimental observations for our substrates A-D? In the above described interfacial energy argument only the interfacial energies are taken into account. The positions of the (global) energy minima may be correctly determined from such a calculation. Possible barriers to the CB to W transition, are, however, not taken into account. When the CB to W transition is kinetically hindered, barriers should be taken into account and the above described interfacial energy argument fails to describe the transition. The possible existence of an energy barrier between the CB and the W state is, among others, described by Patankar[39,41] and Gao and McCarthy.[42] Koishi *et al.* [38] calculated a barrier on the basis of statistical-mechanics. Savoy and Escobedo[43] reported detailed information about the transition kinetics and mechanism for small droplets on the basis of molecular dynamics (MD) simulations. Nosonovsky[44] reported the existence of energy barriers for surfaces with a re-entrant surface curvature. The variation in the sharpness of the edges and the surface roughness of the micropillars on substrates A–D results in different energy barriers which must be overcome by the evaporating droplet in order to reach the energy minimum in the W state. The development of a model to predict the CB to W transition that includes the possible energy barrier between the CB and the W states is needed. MD simulations seem promising to fill this gap.[43] Our findings emphasize that to design omniphobic substrates not only the geometrical shape and arrangement of the microstructures but also the (nano)roughness and edgecurvature should be taken into account.

3.3.6. Colloidal fakir droplets leading to microsoccerballs

Evaporation-driven particles may show self-assembly, as for example, shown in evaporating droplets of a colloidal dispersion[45], where a capillary flow drags the particles toward the contact line to form a ring-shaped stain. Such a flow not only aggregates the particles, but is also able to organize them in crystalline phases.[46–49] Similar mechanisms such as the convective assembly[50] are currently successfully used to produce two-dimensional colloidal crystal films. To obtain three-dimensional clusters of microparticles, colloidal dispersion droplets can be dried suspended in emulsions,[51–52] in spray dryers,[53] or kept in Leidenfrost levitation.[54, 55] The main drawback of these three-dimensional assembly techniques, is the lack of control on both the amount of particles and the particle arrangement in the remaining structures. Here we illustrate that the use of our omniphobic surfaces for self-assembly of spherical microstructures via droplet evaporation can result in a much more accurate control of both the amount and particle arrangement.[56]

In **Figure 9** a water droplet with polystyrene particles is placed on a superomniphobic surface (see (**1**)). After gently deposition, we wait until the water is evaporated (see (**2**)). We observe that a lumpy ball that looks like a soccer ball is created, together with small microparticles "clustering", excitingly, exclusively on top of the microstructures in a "confined" way (see (**3**) and (**4**)). Despite the lack of directional bonds on the particles, the use of the driving forces between liquid and interface opens the opportunity to control the amount of particles, which leads us to the possibility to use such surfaces to develop simple coating methodologies.

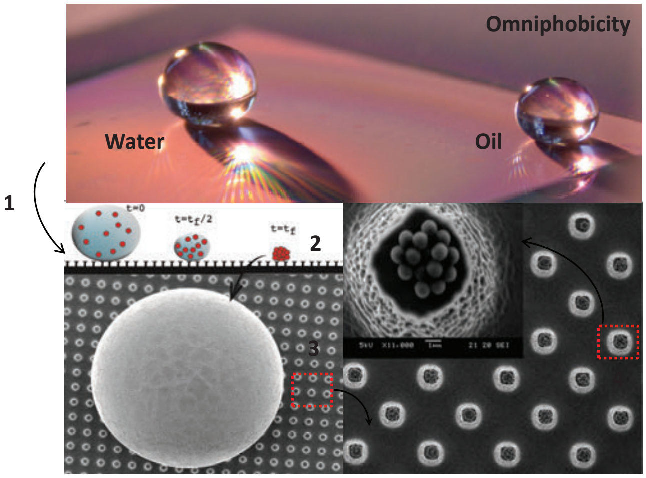

Figure 9. Picture of a superomniphobic surface (see (**1**)) which has been used to evaporate a colloidal fakir droplet (see (**2**)), leading to the creation of a micro soccer ball (see (**3**)) during evaporation. Note the clusters of small particles assembled along the contact line of the evaporating droplet (see (**4**)).

3.4. Conclusions

In summary, we have produced a series of substrates which display high equilibrium contact angles ($\theta > 150^o$) for both water, *n*-octane and olive oil. We have studied the evaporation-driven wetting transition of water on these substrates. It was found that the CB to W transition can be either substantially delayed or totally avoided by changing the edge curvature of the microstructures and addition of nanoscale roughness to the micropillar walls. We verified that neither a Laplace-pressure driven mechanism, nor a global interfacial energy argument describes the CB to W transition on this surfaces correctly, since they are not able to estimate the energy barrier that separate the CB and the W states. The added roughness and edge-curvature was concluded to be the physical origin of this energy barrier. For pillars with sharp edges and straight interfaces, the global interfacial energy argument can be successfully applied to predict the CB to W transition, indicating the absence of an energy barrier on this substrate. Our results convincingly show that, even though the added edge-curvature and roughness did not significantly change the equilibrium contact angle, they greatly enhanced the dynamical robustness of our omniphobic substrates, which can be used to generate micro soccer balls by evaporation of colloidal fakir droplets.

3.5. References

(1) Quéré, D.; *Annu. Rev. Mater. Res.*, **38**, (2008) 71

(2) Barthlott, W.; Neinhuis, C.; *Planta*, **202**, (1997) 1

(3) Liu, M.; Zheng, Y.; Zhai, J.; Jiang, L.; *Acc. Chem. Res.*, **43**, (2010) 368

(4) Bush, J.W.M.; Hu, D. L.; *Annu. Rev. Fluid Mech.*, **38**, (2006) 339

(5) Blossey, R.; *Nature Mater.*, **2**, (2013) 301

(6) Rothstein, J.; *Annu. Rev. Fluid. Mech.*, **42**, (2010) 89

(7) McHale, G.; Newton, M.; Shirtcliffe, N.; *Soft Matter*, **6**, (2009) 714

(8) Meuler, A.; McKinley, G.; Cohen, R.; *ACS Nano*, **4**, (2010) 7048

(9) Varanasi, K.; Hsu, M.; Bhate, N.; Yang, W.; Deng, T.; *Appl. Phys. Lett.*, **95**, (2009) 094101

(10) Tuteja, A.; Choi, W.; Ma, M.; Mabry, J. M.; Mazella, S. A.; Rutledge, G. C.; McKinley, G. H.; Cohen, R. E.; *Science*, **318**, (2007) 1618

(11) Susarrey-Arce, S.; Marín, A. G.; Schlautmann, S.; Lefferts, L.; Gardeniers, J. G. E.; van Houselt, A.; *J. Micromech. Microeng.*, **23**, (2013) 025004

(12) Wu, W.; Wang, X.; Wang, D.; Chen, M.; Zhou, F.; Liu W.; Xue, Q.; *Chem. Commun.*,**1043**, (2009) 1045

(13) Cao, L.; Price, T. P.; Weiss M.; Gao, D.; *Langmuir*, **24**, (2008) 1640

(14) Zhao, H.; Law, K.-Y.; Sambhy, V.; *Langmuir*, **27**, (2011) 5927

(15) Dufour, R.; Brunet, P.; Harnois, M.; Boukherroub, R.; Thomy, V.; Senez, v.; *Small*, **8**, (2012) 1219

(16) Wenzel, R. N.; *Ind. Eng. Chem.*, **28**, (1936) 988

(17) Cassie and S. Baxter, A. D. B.; *Trans. Faraday Soc.*, **40**, (1944) 546

(18) Bonn, D.; Eggers, J.; Indekeu, J.; Meunier, J.; Rolley, E.; *Rev. Mod. Phys.*, **81**, (2009) 739

(19) Erbil, H. Y.; Cansoy, C. E.; *Langmuir*, **25**, (2009) 14135

(20) Sbragaglia, M.; Peters, A. M.; Pirat, C.; Borkent, B. M.; Lammertink, R. G. H.; Wessling, M.; Lohse, D.; *Phys. Rev. Lett.*, **99**, (2007) 156001

(21) Pirat, C.; Sbragaglia, M.; Peters, A. M.; Borkent, B. M.; Lammertink, R. G. H.; Wessling, M.; Lohse, D.; *Europhys. Lett.*, **81**, (2008) 66002

(22) Peters, A. M.; Pirat, C.; Sbragaglia, M.; Borkent, B. M.; Wessling, M.; Lohse, D.; Lammertink, R. G. H.; *Eur. Phys. J. E*, **29**, (2009) 391

(23) Kown, H.-M. Paxson, A. T.; Varanasi, K. K.; Patankar, A.; *Phys. Rev. Lett.*, **106**, (2011) 036102

(24) Manukyan, G.; Oh, J. M.; van den Ende, D.; Lammertink, R. G. H.; Mugele, F.; *Phys. Rev. Lett.*, **106**, (2011) 014501

(25) Bartolo, D.; Bouamrirene, F.; Verneuil, É.; Buguin, A.; Silberzan, P.; Moulinet, S.; *Europhys. Lett.*, **74**, (2006) 299

(26) Tsai, P.; Pacheco, S.; Pirat, C.; Lefferts, L.; Lohse, D.; *Langmuir*, **25**, (2009) 12293

(27) Bormashenko, E.; Pogreb, R.; Whyman, G.; Bormashenko, Y.; Erlich, M.; *Appl. Phys. Lett.*, **90**, (2007) 201917

(28) Jung, Y. C.; Bhushan, B.; *Langmuir*, **25**, (2009) 9208

(29) Journet, C.; Moulinet, S.; Ybert, C.; Purcell, S. T.; Bocquet, L.; *Europhys. Lett.*, **71**, (2005) 104

(30) Tsai, P.; Lammertink, R. G. H.; Wessling, M.; Lohse, D.; *Phys. Rev. Lett.*, **104**, (2010) 116102

(31) McHale, G.; Aqil, S.; Shirtcliffe, N. J.; Newton, M. I.; Erbil, H. Y.; *Langmuir*, **21**, (2005) 11053

(32) Reyssat, M.; Yeomans, J. M.; Quéré, D.; *Europhys. Lett.*, **81**, (2008) 26006

(33) Bliznyuk, O.; Veligura, V.; Kooij, E. S.; Zandvliet H. J. W., Poelsema, B.; *Phys. Rev. E*, **83**, (2011) 041607

(34) Gelderblom, H.; Marín, A. G.; Nair, H.; van Houselt, A.; Lefferts, L.; Snoeijer, J. H.; Lohse, D.; *Phys. Rev. E*, **83**, (2011) 026306

(35) Moulinet, S.; Bartolo, D.; *Eur. Phys. J. E*, **24**, (2007) 251

(36) Kusumaatmaja, H.; Blow, M. L.; Dupuis, A.; Yeomans, J. M.; *Europhys. Lett.*, **81**, (2008) 36003

(37) Barbieri, L.; Wagner, E.; Hoffmann, P.; *Langmuir*, **23**, (2007) 1723

(38) Koishi, T.; Yasuoka, K.; Fujikawa, S.; Ebisuzak T.; Zeng, X. C.; *Proc. Natl. Acad. Sci.*, **106**, (2009) 8435

(39) Patankar, N. A.; *Langmuir*, **20**, (2004) 7097

(40) Amassian, A.; Pozdin, V. A.; Desai, T. V.; Hong, S.; Woll, A. R.; Ferguson, J. D.; Brock, J. D.; Malliaras, G. G.; Engstrom, J. R.; *J. Mater. Chem.*, **19**, (2009) 5580

(41) He, B.; Patankar, N. A.; Lee, J.; *Langmuir*, **19**, (2003) 4999

(42) Gao, L.; McCarthy, T. J.; *Langmuir*, **23**, (2007) 3762

(43) Savoy, E. S.; Escobedo, F. A.; *Langmuir*, **28**, (2012) 3412

(44) Nosonovsky, M.; *Langmuir*, **23**, (2003) 3157

(45) Deegan, R.D.; Bakajin, O.; Dupont, T. F.; Huber, G.; Nagel, S. R.; Witten, T. A.; *Nature*, **828**, (1997) 827

(46) Fan, F.; Stebe, K.J.; *Langmuir*, **20**, (2004) 3062

(47) Bigioni, T. P.; Lin, X.-M.; Nguyen, T. T.; Corwin, E. I.; Witten, T. A.; Jaeger, H. M.; *Nat Mater*, **5**, (2006) 265

(48) Harris, D.J.; Hu, H.; Conrad, J. C.; Lewis, J. A.; *Phys. Rev. Lett.*, **98**, (2007) 148301

(49) Marín, A.G.; Gelderblom, H.; Lohse, D.; Snoeijer, J. H.; *Phys. Rev. Lett.*, **107**, (2011) 085502

(50) Velikov, K. P.; Christova, C. G.; Dullens, R. P. A.; van Blaaderen, A.; *Science*, **296**, (2002)106

(51) Velev, O. D.; Lenhoff, A. M.; Kaler, E. W.; *Science*, **287**, (2000) 2240

(52) Manoharan, V.N.; Elsesser, M. T.; Pine, D. J.; *Science*, **301**, (2003) 483

(53) Sen, D.; Spalla, O.; Taché, O.; Haltebourg, P.; Thill, A.; *Langmuir*, **23**, (2007) 4296

(54) Tsapis N, Dufresne, E. R.; Sinha, S. S.; Riera, C. S.; Hutchinson, J. W.; Mahadevan, L.; Weitz, D. A.; *Phys. Rev. Lett.*, **94**, (2005) 018302

(55) Tran, T.; Staat, H. J. J.; Susarrey-Arce, A.; Foertsch, T. C.; van Houselt, A.; Gardeniers, J. G. E.; Prosperetti, A.; Lohse, D.; Sun, C.; *Soft Matter*, **9**, (2013) 3272

(56) Á. G. Marín, H. Gelderblom, A. Susarrey-Arce, A. van Houselt, L. Lefferts, J. G. E. Gardeniers, D. Lohse and J. H. Snoeijer, *Proc. Natl. Acad. Sci.*, **109**, (2012) 16455

4

Combining microreactor technology with ATR-IR

In situ characterization and microreactor system integration

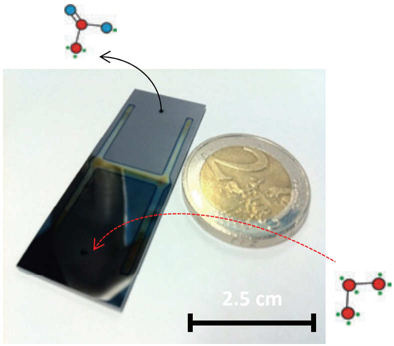

A silicon-based microreactor with a structure that allows in situ characterization by Attenuated Total Internal Reflection Infrared spectroscopy (ATR-IR) of processes driven by an external electric field (E-field) is presented. The microreactor is characterized electrically and spectroscopically. Inevitable artefacts during application of an electric field over a gas or liquid medium in the flow channel of the microreactor are carefully investigated and electrical, mechanical and optical phenomena which may affect the interpretation of the ATR-IR spectroscopy are discussed. Among them are heating of the microreactor as a result of the E-field driven current and the associated phonon generation. Some preliminary results are shown for the detection of CO_2 gas and ammonium ions in solution upon applying an electrical field. The ability to follow liquid phase reactions *in situ* is demonstrated.

Parts of this chapter has been submitted for publication as

A. Susarrey-Arce, R.M. Tiggelaar, E. Karabudak, R.G.P. Sanders, B. Geerdink, S. Schlautmann, L. Lefferts, A. van Houselt and J.G.E. Gardeniers, A new ATR-IR microreactor to study electrical field driven processes (**2014**)

4.1. E-field driven processes in an ATR-IR microreactor

The application of an external electric field (E-field) to matter results in a variety of physical and chemical effects,[1] including changes in H_2 storage capacity[2] or catalytic activity.[3] Depending on the magnitude of the E-field, one can distinguish two different modes of the interaction of the E-field with matter:

High fields, where electrons are extracted from matter and injected into a medium,[4, 5] lead to a steady current through the system, involving processes like excitation,[6, 7] dissociation and cracking,[8, 9, 10, 11] dehydrogenation[12] or synthesis of molecules.[13] Typical examples are electrochemistry in liquids and plasma chemistry in gases.

Low fields, where a redistribution of charges occurs and surfaces and molecules are polarized, may induce a change in reactivity, without direct electron transfer. Redistribution of charge within a molecule positioned in an external E-field may lead to conformational changes[14] which may become visible as a change in the vibration frequency of molecular bonds[15-17] or may induce IR-active vibrations in molecules which would not exhibit any IR absorption bands in the absence of an external field.[18]

A well-known method used to identify and characterize the conformation of adsorbed or free molecules is Attenuated Total Reflection Infrared spectroscopy (ATR-IR).[19, 20] In ATR-IR the highest sensitivity is close to the ATR-IR crystal surface, which opens the opportunity to study the feasibility of applying an external electric field to switch between adsorption and desorption of species on a surface.[21-22] The motivation to use a switchable external electric field originates from our earlier work on selective oxidation of propane at room temperature under influence of the built-in electric field of unshielded Ca^{2+} ions in zeolite-Y.[23] The electrostatic forces generated by the cations are not only responsible for the activation of propane and O_2, but unfortunately also for a strong adsorption of product molecules like acetone.[24] Closing the catalytic cycle at low temperature would be possible, if these electrostatic forces could be turned off, or at least reduced to a value where the adsorbed products can be released from the surface with minor thermal activation.

This contribution, as part of an ongoing study on E-field controlled adsorption/desorption processes in heterogeneous catalysis, describes our efforts to develop a silicon-based microreactor that enables the observation of E-field induced changes in a medium by ATR-IR. After a discussion of design and fabrication issues, followed by a detailed electrical characterization of the microreactor, we will demonstrate and explain the detection of electric field-induced optical phonons in this microreactor and discuss the influence of an external E-field on the decomposition of ammonia, which is an electrochemical process involving the injection of charges in liquid, i.e. an example of the effect of a high E-field. We will also show results for CO_2 gas at high E-field, which results in slight modification of the IR lines of CO_2 which will be discussed in the light of thermal effects.

4.2. Experimental section

4.2.1. Microreactor design and fabrication and characterization of $TiSi_2$ electrodes

Figure 1(a) shows a schematic presentation of the main device used in this study, namely a microreactor with micromachined cylindrical pillars with height h = 15 μm, width (diameter) w = 9 μm, and pitch p = 24 μm, embedded in a flow channel. **Figure 1(b)** shows a SEM image of some of the 1,120,000 pillars. The material chosen for the body of the microreactor is silicon, because of its semiconducting properties and IR transparency. The gap between the top surface of the cylindrical pillars and the flat surface of the bottom half of the microreactor, which serves as an ATR-IR crystal, is 900 nm. This small gap was created by local etching of a thin silicon dioxide layer, which layer also serves as an insulator between the pillar part and the ATR part of the device. Some larger pillars (50 and 100 μm diameter) in a special arrangement (see *Supporting*

Information) were positioned in the microchannel and left with the oxide layer, so that the two parts of the chip, besides on the edges of the microchannel, also become bonded on these pillars. We will refer to these supporting pillars as "columns", to avoid confusion with the pillars with a gap used for E-field enhancement. The columns serve as a means for mechanical enforcement of the chip, to avoid outward bending of the upper and lower microchannel walls due to pressure-driven fluid flow through the chip, and to avoid inward bending which may arise due to the electrostatic forces between top and bottom surfaces of the microchannel. The number of these enforcement columns (see *Supporting Information* for details) was kept to a minimum, to leave as many as possible "active" pillars (i.e. pillars with a gap between their tip and the opposite surface).

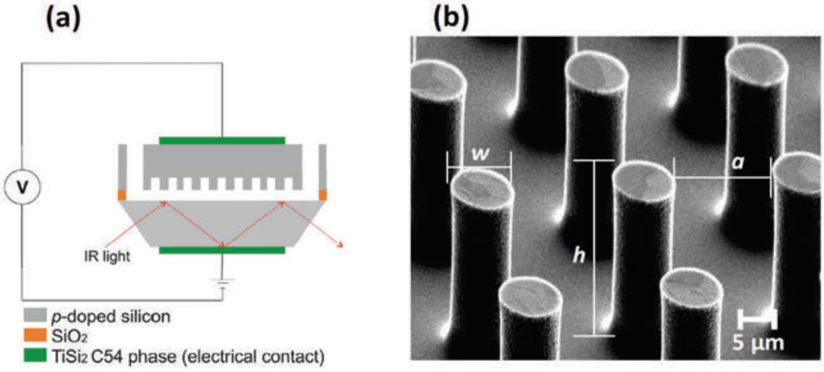

Figure 1. (a) Cross sectional representation of a silicon-based microreactor with micropillars, directly bonded to a micromachined ATR-IR silicon crystal, and with electrodes on either side to apply an electric field across a flow channel. The idea behind this device is that specific probe molecules are directed into the microreactor channel, the electrical field that is concentrated at the top of the micropillars will change the electronic distribution in the molecules, either in their adsorbed or free state, by which the chemical reactivity and/or adsorption/desorption properties of the molecules will change, resulting in a different product distribution or higher conversion. (b) SEM image of realized micropillars; $h = 15$ µm, $w = 9$ µm, distance between pillars $a = p - w = 15$ µm)

The electrodes deposited on the outer surfaces of the device are used to apply an electric field across the microchannel, and more specifically between the pillar tips and the opposite surface. In this way the pillars serve to locally enhance the electric field. Some of the devices used in this study did not have pillars, but a flat surface, with a similar distance of 900 nm to the surface of the ATR crystal.

The choice of electrode material is based on the notion that it should be electrically conductive as well as transparent in the IR range. It was decided to use thin films of $TiSi_2$, a material often used for IR imaging because of its low reflectivity in the wavelength range of 1 μm (5000 cm^{-1}) to 5 μm (1000 cm^{-1}), the mid-ATR-IR working window[25] (see **Figure 2(a)**). We have experimentally verified this by comparing the transmittance of a bare silicon ATR crystal with crystals covered with a thin Ti or a thin $TiSi_2$ film, see **Figure 2(b)**.

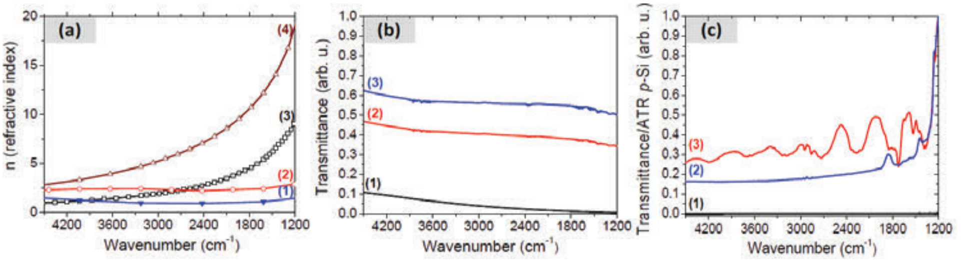

Figure 2. (a) Refractive index as a function of the wavenumber for different metals in the mid IR region: (1) $TiSi_2$, (2) Os, (3) Au and (4) Al. (b) IR transmittance spectra as a function of the wavenumber for (1) ATR-Si crystal coated with Ti, (2) ATR-Si crystal coated with $TiSi_2$ and (3) bare ATR-Si crystal. (c) IR transmittance spectra for (1) ATR-crystal of highly doped p^+-silicon, (2) flat microreactor (MR) and (3) pillared MR. The spectra are normalized to the transmittance of the *p*-type silicon ATR-crystal.

A drawback of $TiSi_2$ as an electrode material is that it forms a Schottky barrier with *p*-type silicon, with a work function of *ca.* 0.6 eV.[26, 27] Applying $TiSi_2$ on highly doped silicon (p^+-Si) would avoid the Schottky contact.[26, 28] To check this option, the total internal reflection of an IR beam passing through an ATR-crystal was recorded for a microfabricated highly doped *p*-type silicon crystal. The resulting transmittance spectra in **Figure 2(c)** show that for our ATR-IR microreactors with an ATR-crystal of normal *p*-type silicon (carrier concentration *ca.* 2x1015 cm^{-3}) *ca.* 20-30% of the IR light is collected. On the other hand, the p^+-silicon (carrier concentration *ca.* 5x1018 cm^{-3}) specimen shows no IR transmittance, which agrees with the results of Engstrom,[29] who reported a loss of transmittance for increased carrier concentrations in silicon. For our ATR crystals therefore low-doped silicon is preferred, and the voltage losses over the Schottky barrier are taken for granted.

The thickness of the $TiSi_2$ films used in this study was estimated from TEM images to be 18 ± 2 nm, with a well-aligned monocrystalline phase,[30] see *Supporting Information* for details about the structural characterization of the films. The electrical resistivity of $TiSi_2$ films, obtained by means of four-point probe measurements, is 15 ± 2 Ω-cm, which is in agreement with reported values of the $TiSi_2$-C54 phase.[31, 32]

4.3. Results and discussion

4.3.1. Electrical characterization of E-field controlled microreactors

Figure 3(a) shows current (i) - electric field (E) log-log plots for five different devices: (**1**) a micromachined *p*-type ATR crystal directly bonded to a silicon piece, with an intermediate silicon dioxide layer of 900 nm thickness; (**2**) a *p*-type microreactor with a microchannel height of 900 nm; (**3**) a *p*-type microreactor with pillars with a 120 nm SiO_2 layer on the ATR crystal, (**4**) a similar *p*-type microreactor with pillars, without SiO_2 layer on the ATR crystal, and (**5**) a p^+-type microreactor with a 120 nm SiO_2 layer on the ATR crystal. In microreactors (**2**) to (**5**) the two silicon pieces are electrically insulated in regions where there are no pillars or gaps, by a 900 nm thick SiO_2 layer. For all five devices an electric field across the device is established by applying a negative potential to the top electrode of the chip, whereas the bottom electrode (the one on the ATR-crystal) is connected to ground. All reactors were filled with 1 atm of He gas (water content 5 ppm). All current is assumed to run through the inside of the microreactor (possible outside current paths were avoided, see *Supporting Information*).

The values mentioned in **Figure 3** are the *applied* electric fields. For the reactor types **3** and **5** with a silicon dioxide layer of 120 nm between pillar tips and opposite surface, the applied voltage should in principle be corrected because the voltage will divide as V(gas) : V(SiO_2) = 25 : 1 (based on a simple electronic circuit model of two capacitors in series), implying that 96% of the applied voltage is over the gas gap. We ignored this small correction in plotting the curves in **Figure 3**, because the reproducibility in current values between similar microreactors was typically within *ca.* 20%. We attribute this to variations in the contact between the copper electrodes in the chip holder and the thin film contacts on either side of the microreactor chip (see *Supporting Information* for a detailed description of the experimental setup).

Comparison of the curves in **Figure 3(a)** for the different devices shows that for low E-fields the currents for devices (**2**), (**4**) and (**5**) exhibit V^n behavior, with n between 1.5 and 2. At high E-fields. For type (**3**) the low E-field relation is more Ohmic, with n approaching 1. At high E-fields, curves (**1**), (**3**) and (**4**) show a change in slope in the i-V curves, where for curve (**3**) possibly a second slope change may be visible, close to 10^6 V/cm. Since the slope changes are gradual in some case, the suspicion arises whether the behavior at high E-fields becomes exponential.

Exponential current-voltage behavior could be indicative of field electron emission, and in order to investigate whether this is the case, the i-E curves are represented as Fowler-Nordheim (FN) graphs (ln (i/E^2) *vs.* E^{-1})[33] in **Figure 3(b)**. FN conduction describes tunneling of electrons from a semiconductor conduction band into the conduction band of a dielectric, through part of the potential barrier at the semiconductor-dielectric interface, or from the Fermi level of a metal into vacuum, both due to the application of a high electric field. For emission from a flat surface or film, the electric field must be of the order of 10^7 V/cm for a typical electron affinity of 4 eV. Field electron emission is therefore mostly only achieved with surface protrusions with high curvatures, e.g. Spindt-type emitters,[34] or nanostructures like nanorods and nanotubes.[35, 36]

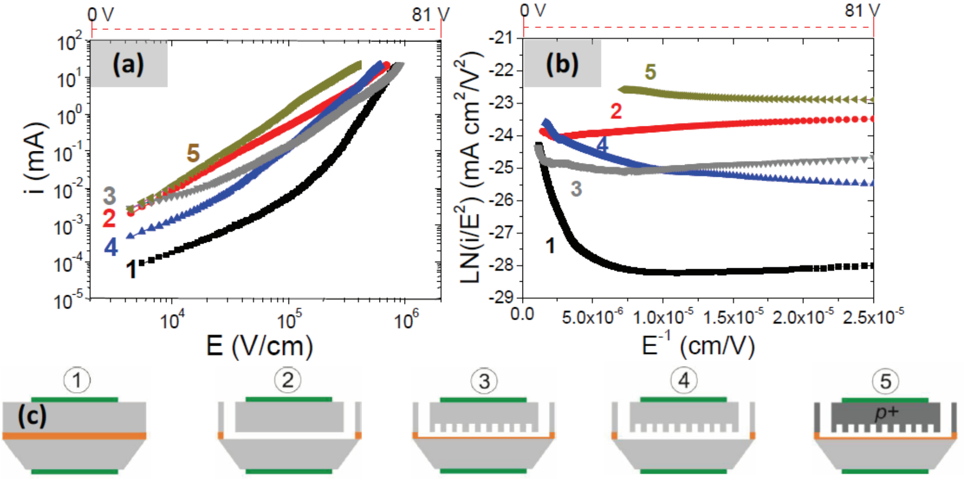

Figure 3. (a) Log-Log plots of current versus electrical field for (**1**) a fusion bonded *p*-type Si–SiO_2–Si stack with 900 nm SiO_2 thickness, (**2**) a *p*-type microreactor with a 900 nm high channel without micropillars (flat microreactor); (**3**) a *p*-type microreactor with 15 µm high micropillars with a gap of 780 nm between the pillar tips and the ATR crystal, which has a 120 nm thick SiO_2 layer coated on its surface; (**4**) a *p*-type microreactor with 15 µm high micropillars and a gap of 900 nm between the pillar tips and the opposite surface; (**5**) a *p*+-type microreactor with similar configuration as reactor (**3**), i.e. with a SiO_2 layer of 120 nm on the ATR crystal. The measurements were done with 1 atm of pure He gas in the microchannel. All measurements were performed at room temperature. (b). The corresponding Fowler-Nordheim (FN) plots for the devices (**1**)-(**5**). (c) Schematic representations of the devices (**1**)-(**5**).

In **Figure 3(b)** it can be seen that device (**1**) shows a change in slope at low E^{-1} values, which could be indicative of field emission through the silicon oxide layer. The slope derived from the curve for high E-fields gives a value of -1.5 MV/cm, which is 2 orders of magnitude lower than typical values reported in literature.[33] This makes FN tunneling an unlikely explanation for the current in this device. For the devices (**3**)-(**5**), where pillars are present, the graphs do not show any indication for FN behavior.

When similar experiments as above are carried out with a reversed electrical field (positive potential on pillars), for devices type **1** and **2** the voltage characteristics are symmetric, for the other types the current at reversed voltages is a factor of **2** - **3** lower. The latter could be due to local E-field enhancement at the pillar rims, which may have an asymmetric effect on the movement of electrons in the gas gap.

One of the special features in our devices is the extremely small gap between the two differently charged silicon electrodes. Already in papers from the 1950's it was discussed that for microscale electrode gaps the well-known Paschen curve for electrical breakdown of gases should be corrected. Boyle and Kisliuk state that in atmospheric gas for extremely small electrode separations (which in their case means a few hundred micrometers): "the breakdown is sufficiently great to draw measurable field-emission current from the cathode, which produces a relatively small number of ions".[37] In the work of Slade and Taylor[38] it is demonstrated that in small (up to 40 μm) atmospheric pressure air gaps breakdown occurs at very much the same voltages as in vacuum, and follows a similar linear relation between breakdown voltage and electrode gap. This linearity for gas gaps holds up to *ca.* 5 μm, from whereon the Paschen curve becomes valid again. Slade and taylor state that the reason for the similarity is that the mean free path of electrons in 1 atm air is *ca.* 0.5 μm, implying that electrons emitted from the cathode will collide with gas molecules only a limited number of times before reaching the anode, therefore the presence of gas will have a minor effect on the breakdown process. Go *et al.* have recently studied breakdown in microscale gaps in great detail and developed a comprehensive model that takes into account both Townsend ionization (the origin of the Paschen curve, for higher electrode gaps) and ion-enhanced field emission mechanisms (responsible for the breakdown in the smallest gaps).[39] From their theoretical work it can be derived that over a distance of 2 μm only a fraction of the electrons (estimated to be 30-40% from the electron energy distribution in **Figure 1(b)** in ref. [40, 41]) have collided with gas molecules, and generated ions. This is consistent with the mean free path of electrons in the argon gas they studied, which we estimate at 0.18 μm (using collision diameter data from ref. [42]). For the helium gas in our case we calculate that (for typical electron kinetic energies of 10 - 20 eV) the electron mean free path is between 1.0 and 2.0 μm (again using data from ref. [42]), which would imply that for a gap of 0.9 μm electrons hardly collide with helium gas atoms. Furthermore, since the ionization potential of He is relatively high (almost twice that of the Argon gas studied by Li and Go [40]), negligible gas ionization is predicted for our experiments, so that the electrons carry all the current in the sub-micron gap. The latter is in line with the Monte Carlo collision simulations of Semnani *et al.* who find that for a 0.5 μm gap with Ar gas *ca.* 90 % of the current is carried by electrons.[43]

The literature cited above, and similar publications, discusses electrical conduction through microgaps as being the result of Fowler-Nordheim field emission. Above we have already established that this mechanism probably is not present in our devices, because the corresponding plots in **Figure 3(b)** should have a significant (negative) slope, proportional to the local thermodynamic work function to the power 3/2.[33, 44, 45] The slope in our FN plots is almost negligible (except for device (**1**)). We could only find one other report of nearly horizontal FN-plots, by Strong *et al.* who have studied planar suspended polysilicon electrodes with gaps of 2 to 7 μm.[46] There is a peculiar difference between our results and theirs, in that their FN-plots show three horizontal lines, with distinct jumps between them, which these authors, unfortunately without definitive proof, attribute to transitions between different discharge processes.

Our conclusion from the above, and our own experimental data is that it is as yet unclear what the exact mechanism is for the current-voltage behavior in our microreactor types (**2**) - (**5**).

4.3.2 Infrared measurement of effects introduced by the application of an electric field

The experiments discussed in this paragraph are performed to test the ATR-IR response of the microreactors to an applied electric field and more specifically, determine the borders of the electric field regimes (polarization vs. electron emission) in which these microreactors can be operated.

4.3.2.1. Optical interference effects

In ATR-IR experiments with the microreactors, fringes are observed in the IR transmittance spectra, which are very pronounced for the microreactor with the micropillars. They are best observed at the highest spectral resolution settings (6 cm^{-1} and below, where the 1 cm^{-1} resolution setting gives the highest amplitude fringes), and depend on the strength of the electric field applied to the microreactor. **Figure 4** gives representative examples of the effects. The periodicity of the fringes is 9.7 cm^{-1} at the highest available spectral resolution of 1 cm^{-1}. This corresponds to a wavelength of 1030 μm, which accidentally is very close to twice the thickness of the ATR silicon crystal used in this study (525 ±25 μm).

The fact that these fringes are *exclusively* observed (see **Figure 4(b-d)**) in the microreactor with the micropillars, indicates that the internally reflected IR light interacts with the pillars, or a phenomenon related to the pillars. Such an interaction will occur via the evanescent field of the light transmitted in the silicon crystal. The value of the penetration depth (d_p) of the IR light into the microchannel as it is commonly calculated,[47, 48] is found to range from *ca.* 150 nm at 4000 cm^{-1} to *ca.* 530 nm at 1200 cm^{-1}. In this calculation, a slope angle and incident angle of 54.7° are considered, which corresponds to the {111}-planes which are created at the sides of the Si specimen by the micromachining process.[49, 50] These depth values are smaller than the gap between pillar top and ATR crystal, however, it has to be noted that the penetration depth d_p is defined as the distance required for the amplitude of the electric field contribution to the electromagnetic wave to fall to 1/e, or *ca.* 37%, of its value at the surface. The evanescent field equation, $E = E_{surface} \exp\left(\frac{-z}{d_p}\right)$, with z the direction perpendicular to the surface and $E_{surface}$ the electric field at the surface of the ATR crystal, allows us to calculate that at a depth equal to the gap between pillar tips and opposite surface, i.e. 900 nm, this field has decayed to *ca.* 17% at 1200 cm^{-1}, which is still a substantial value. Therefore, an interaction of the tail of the evanescent wave of the IR-radiation in the silicon crystal with the micropillar tips may indeed be a likely process.

The fact that the intensity of the observed fringes depends on the magnitude of the electric field applied to the microreactor (and in fact only occurs when the E-field is above *ca.* 20 V/cm) is another important observation. A possible cause for this effect is mechanical deformation of the microreactor due to the electrostatic attraction between the pillar tips and the opposite silicon part. Thus, it could be that, despite the additional supporting columns implemented in the microreactor, the electrostatic force decreases the gap between pillar tips and ATR crystal surface. This leads to an effect similar to the "nanomechanical integrated-optical effect" first described by Lukosz *et al.*,[51] which consists in the modulation of light transmittance through planar optical waveguides caused by moving an element (e.g., a dielectric) in the evanescent field of the guided light. The effect has, for example, been used in a microphone with optical read-out[52] and in a mechano-optical waveguide intensity on-off switch.[53] In the work of Lukosz *et al.* changes in the width of the gap between element and waveguide of a few nanometer were found to induce measurable changes in the effective refractive index of a guided wave, which then leads to phase and/or amplitude modulation.

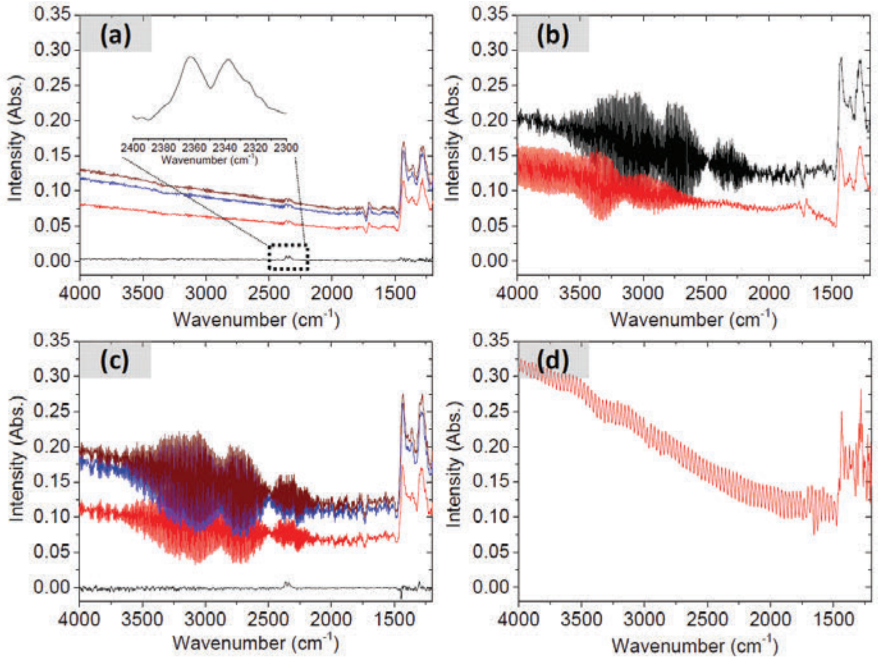

Figure 4. Room temperature ATR-IR spectra, recorded at resolution of 4 cm^{-1}, of: (a) Flat *p*-type microreactor i.e. type (**2**) in **Figure 3(c)**, filled with 1 atm of pure CO_2 gas, at voltages of (from bottom to top) -10 V, -60 V, -70 and -75 V; the inset shows the asymmetric stretch vibration of CO_2 in gas phase; (b) Microreactors with micropillars; the black top curve is for reactor type (**4**), the red bottom curve for type (**3**), see **Figure 3(c)**; filled with 1 atm He. (c) Microreactor type (**4**) with 1 atm of pure CO_2 gas, at (from bottom to top) -10 V, -60 V, -70 and -75 V. (d) Microreactor type (**5**) with 1 atm He, at -75 V.

We suspect that we have observed a similar effect in our devices, where displacement of the pillar tips towards the surface of the ATR crystal modulates the transmittance of IR light in that crystal, to an extend depending on the size (but not on the sign, as indeed was observed) of the applied E-field. In **Figure 4 (c)** it can be seen that the amplitude of the fringes increases with applied E-field. As elaborated in detail in the *Supporting Information*, two mechanical deformation mechanisms may occur, which both have as a result that the pillar-to-ATR crystal-gap decreases with E-field: compression of the supporting columns and bending of the silicon material into which the pillars are micromachined. For an applied voltage of 50 Volts, we calculate that the two deformation mechanisms lead to a gap decrease of 0.8 nm and 3.9 nm, respectively (or, since the original gap is 900 nm, to relative gap decreases of 0.1 and 0.4 %, respectively).

We furthermore speculate that the observed fringes are caused by light diffraction by the grating that is formed by the regular pattern of the pillars (note that the studied wavelength range is 1 - 9 μm, whereas the smallest pillar-to-pillar distance and the pillar array pitch are 10 and 20 μm, respectively). This is supported by the data in **Figure 4(b)**, which shows that a SiO_2 layer on the ATR crystal, which changes the refractive index of the medium in which the evanescent field is active, and therewith modifies the grating properties, leads to a shift of the fringes to lower IR wavelengths. In the IR spectrum presented in **Figure 4(d)**, of a p^+-microreactor, the amplitude of the fringes is significantly reduced, which we think is due to the higher IR reflection and absorption in the p^+-material (**Figure 2(c)**), which damps the diffraction, but also leads to a loss in IR transmittance of 40% compared to microreactors type (**2**) and (**4**) which are composed of low-doped silicon. Also, as we will discuss in the following section, a temperature increase due to thermalization of phonons plays a role in enhancing the amplitude of the diffraction pattern with increasing E-field over microreactor of type (**3**) and (**4**) in **Figure 3(c)**, as well as in other data obtained under high voltages, as follows from the negative slope that is observed for these IR spectra when going from 4000 cm^{-1} to 1200 cm^{-1}. Finally, it is not unlikely that the interference is not caused by the presence of the pillars themselves, but by the space charge around them under electron emission conditions, so that the fringes are a result of electro-optic coupling of the periodic space charge with the evanescent field of the waveguiding ATR crystal.

Since for the purpose of this study it is acceptable to acquire IR spectra at a lower spectral resolution, for which setting the fringes are hardly visible (see *Supporting Information* for additional experimental data on this topic), we decided to refrain from a detailed analysis of the fringes.

4.3.2.2. Phonon generation and relaxation

At electrical potentials above -50 Volts, generation of phonons is observed. The phonon absorption lines are in agreement with recent findings of Karabudak *et al.* who reported silicon photo-excitation in a thin (*ca.* 554 μm thick) ATR-IR crystal by using a Casix Nd-YAG laser source of 1064 nm (~9398 cm^{-1}, ~1 μm) with phonon absorption peaks at 1448 cm^{-1}, 1370 cm^{-1} and 1300 cm^{-1}.[54] Different from the work of Karabudak *et al.*, the mechanism by which phonons are excited in the present study is by electronic processes. We have studied the phonon excitation by applying different voltages (-40 V, -50 V and -75 V) to microreactor type **4**, the results of which are presented in **Figure 5(a)-(c)**. All spectra were optimized and recorded with a resolution of 4 cm^{-1} and 64 scans. The results are presented as a function of time for wavelengths 1485-1200 cm^{-1} in contour plots. **Figure 5(d)** displays the relative IR intensity (at 1431 cm^{-1}) as a function of the potential, at a time of 30 minutes when a steady-state phonon signal is observed, while in the relative IR intensity of the bands at 1431 cm^{-1}, 1357 cm^{-1} and 1290 cm^{-1} during application of a -50 V block pulse is shown as a function of time in **Figure 5(e)** and as function of the measured current in **Figure 5(f).** From **Figure 5(a)-(d)** it is evident that there is a threshold voltage for phonon excitation around -50 V. Clearly ~20 min are needed in **Figure 5(b), (c), (e)** to reach a steady phonon signal, most probably due to resistive heating of the Si. The intensities of the phonon bands during that pulse, shown in **Figure 5(f)**, increase with increasing current, which may be an indication of Joule heating. For a separate experiment in which a -75 V pulse was applied, we have measured (via a thermocouple connected to the chip) that the temperature had increased from 25 °C to 48 °C after application of the pulse.

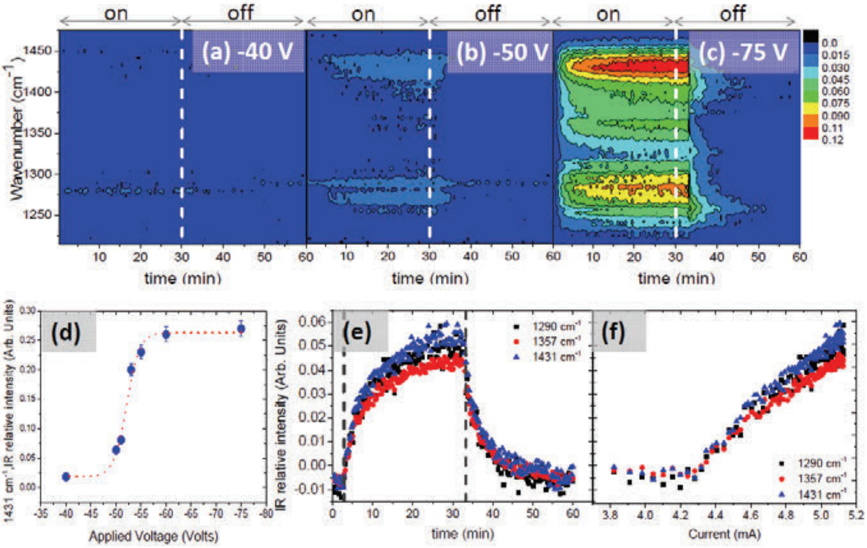

Figure 5. (a)-(c) Contour plots of the ATR-IR intensity from 1485-1200 cm^{-1} during application of a block-pulse as a function of time, for microreactor **4** with 1 atm He gas. The applied potentials during the "on-period" are (a) -40 V, (b) -50 V and (c) -75 V. Each contour plot has the same intensity scale. (d) The relative ATR-IR intensity at 1431 cm^{-1} after reaching steady state as a function of the applied voltage. (e) The relative ATR-IR intensity measured during an applied potential of -50 V as a function of time. (f) The relative ATR-IR intensity measured during an applied potential of -50 V as a function of the current. The green line is a fit to the square-root of the current.

4.3.2.3 Decrease of the 1727 cm^{-1} interstitial oxygen band

With increasing voltage over the microreactors, an increasing negative peak at 1727 cm^{-1} is observed (see for instance **Figure 4(a)** or **Figure 6(b)**). This peak, which is ascribed to interstitial oxygen in the Si lattice, arises due to a rise of temperature during application of an external voltage over the microreactors.[55] For a detailed discussion we refer the reader to *Chapter 5*.

4.3.3. Infrared measurement of gases and liquids under application of an electric field

4.3.3.1. CO_2

Since the optical path-length in ATR-IR experiments is purposely short, CO_2 is selected to test the microreactor's response to gases, because of its relatively high IR absorption scattering cross-section. CO_2 is also of interest from a chemical point of view, since, in the presence of surface oxides it may lead to carbonate species, with characteristic absorption[56-60] at the frequencies were we observe phonon absorption lines (see paragraph 4.2).

Important to note here is that the CO_2 experiments performed here will not reveal information about the feasibility of our long-term goal stated in the introduction, i.e. to control desorption of products by application of an electric field. CO_2 in the gas phase is a linear molecule with zero dipole moment, on which an electric field will not be effective. The situation is different for adsorbed species, however, the E-field expected to have a significant effect on adsorbed CO_2 (or CO) is of the order of 2 to $6 \cdot 10^7$ V/cm,[61-62] whereas in some publications even higher numbers, of the order of 1 to $3 \cdot 10^8$ V/cm, are mentioned.[63-64] These field values, as was discussed above, are much higher than the E-fields at which significant currents start to flow in our microreactor designs.

For ATR-IR microreactor experiments a total flow of 30 μL/min of CO_2 (99.99% purity) from Praxair is used at room temperature. The ATR-IR measurements presented henceforth are recorded against a background signal that is recorded with a total flow of 30 μL/min of He (99.99% purity, specified water content: 5 ppm) from Praxair at room temperature. Since we do not expect that the other microreactors will give different results for the chemical experiments in this section and the next, we have focused on microreactor type **4**.

ATR-IR spectra were measured at 0 V and -75 V in a microreactor with micropillars (type **4**), filled with CO_2 (**Figure 6**; note that the negative potential is on the micropillars). As long as no electric field is applied, clearly no changes with time were observed in the double lobed asymmetric stretch vibration of CO_2 around 2350 cm^{-1} in **Figure 6(a)**, indicating a stable performance of the microreactor. However, in case a potential of -75 V (which is in the electron conduction regime) is applied after 30 min in **Figure 6(a)**, the contour plot changes significantly during the 30 minutes of application of the voltage pulse and the IR absorption increases over the complete spectral range. Individual ATR-IR spectra before (red), during (green) and after (blue) application of the – 75 V block pulse are shown from 2400 cm^{-1} to 1200 cm^{-1} in **Figure 6(b)**. The positions of the asymmetric CO_2 stretch vibration around 2350 cm^{-1} and the interstitial oxygen absorption at 1727 cm^{-1} are indicated with dashed lines. Clearly an increase in the background absorption is observed upon application of the -75 block pulse, while a disappearance (a negative absorption band) of the interstitial oxygen absorption at 1727 cm^{-1} develops. At low wavenumbers (1450 cm^{-1} to 1200 cm^{-1}) the phonon absorption bands can be observed upon application of the voltage pulse. In addition to the CO_2 absorption around 2350 cm^{-1} many absorption signals with a slightly higher intensity can be observed in the window from 2400 cm^{-1} to 1450 cm^{-1} upon application of the voltage pulse. The increase in background absorption and the increase in intensity of the phonon adsorption lines[54] as well as the decrease of the interstitial oxygen absorption[55] are attributed to the rise of temperature due to heating of the silicon during application of the voltage pulse. After correction for these major temperature induced changes in the background signal (not shown), no significant changes in the asymmetric stretch vibration of CO_2 around 2350 cm^{-1} were observed.

An important point to note here is the following: It has been reported that in He and CO_2 gas at atmospheric pressure, conditions as studied here, at an electric field of $1 \cdot 10^4$ V/cm and higher, Dielectric Barrier Discharge (DBD) occurs (see e.g. [65]; note that these authors have worked with discharge gaps of 100 μm). Some of our measurements were performed in the same range of E-fields, so gas discharge could be a possibility. A similar calculation as was done above for He, using data from ref. [42], leads to a mean free path of electrons in atmospheric CO_2 of

0.2 - 0.3 μm, which is substantially smaller than the gap over which electrons pass in the device studied. Although therefore in this case gas discharge effects cannot be neglected, we did not find evidence in our IR spectra for species which would derive from the ionization of CO_2.

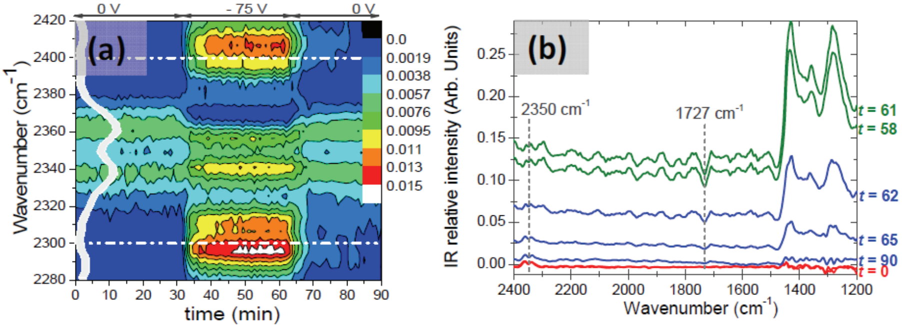

Figure 6. (a) Contour plot of CO_2 absorption lines (2280 to 2420 cm^{-1}) when a -75 V block pulse is applied from t = 30 min to t = 61 min. (b) Individual IR spectra measured during the experiment shown in (a) with an indication of the measurement time. The red spectra are taken before application of the – 75 V block pulse, the green spectra during application of the pulse and the blue ones after application of the pulse. The positions of the asymmetric CO_2 stretch vibration around 2350 cm^{-1} and the interstitial oxygen absorption at 1727 cm^{-1} are indicated. Note the different background levels (the contour plot in (a) has been corrected for these background changes). All measurements were carried out in microreactor type **4**.

4.3.3.2. Decomposition of ammonium

As an example of a case in which electrons are injected into a liquid, we have studied the decomposition of ammonium ($NH_4^+{}_{(aq)}$) upon application of an external potential in microreactor type **4**, through which a 0.25 M solution of NH_4Cl (99.999% purity from Alfa Aesar) in water was flown (30 μL/min). ATR-IR spectra were recorded with a resolution of 8 cm^{-1} with voltage pulses ranging from ± 1 V to ± 50 V. Note that for voltages exceeding ± 15 V we observed a decrease in the OH stretching vibration intensity of water around

3400 cm^{-1} (not shown), most probably due to hydrolysis of water at these voltages (as deduced from the observation of gas bubbles at the reactor exit).

We used the integrated area of the ammonia band located at 1452 cm^{-1} (the inset in **Figure 7(a)** depicts the absorption band at 1452 cm^{-1}), which has been assigned to a symmetric bending mode of the hydrated ion in water[20] to follow the ammonium concentration during the experiment. In **Figure 7(a)** the integrated peak area (open circles, left ordinate) and the current density through the microreactor during application of a -7 V block pulse (solid line, right ordinate) are shown as a function of time. An steep initial increase in the current density is observed when the potential is switched on at $t = 0$, followed by a slight linear increase to ~24.5 $\mu A/cm^2$ between $t \approx 2$ min and $t \approx 30$ minutes, at which moment the potential is switched back to zero, resulting in a sudden sharp decrease in the current density. The intensity of the 1452 cm^{-1} ammonium peak decreases initially, but levels off and reaches a steady value after ~12 minutes. In **Figure 7(b)** the integrated intensity of the peak located at 1550 cm^{-1} (see *Supporting Information* for an ATR-IR spectrum) is shown as a function of time during the experiment (left ordinate). For comparison the integrated intensity of the ammonium band located at 1452 cm^{-1} is shown as well (right ordinate). The integrated area of the 1550 cm^{-1} increases initially, but levels off and reaches a steady value after 12 minutes. The absorption band at 1550 cm^{-1} is attributed to adsorbed NO arising from NH_4^+ decomposition.[20, 66, 67] This attribution is supported by trends in **Figure 7(b)**, suggesting that the disappearing ammonium (decrease of the ammonium peak at 1452 cm^{-1}) is indeed converted to NO (increase of the 1550 cm^{-1} absorption).

In future work we intend to use a microreactor with a thicker electrically insulating layer on the surface of the ATR crystal, to reduce electron transport through the medium in the microreactor. This would allow us to generate new insights in E-field driven acid-base chemistry, like the (NH_3+ HCl)/(NH_4Cl) system, for which recently a theoretical study was reported.[68]

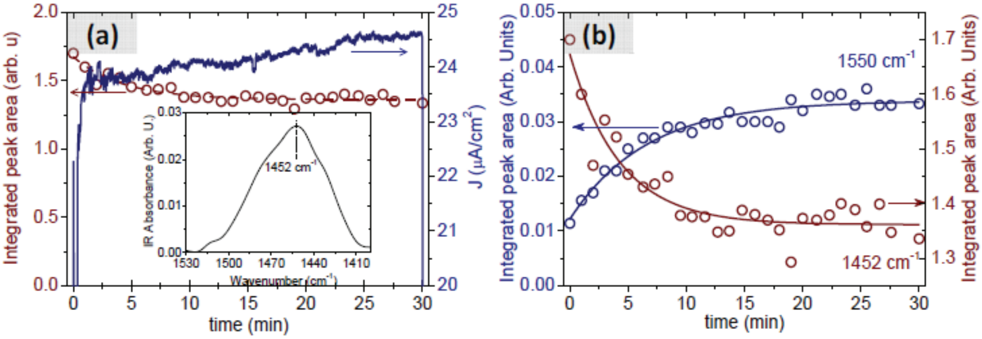

Figure 7. (a) Integrated peak area (open circles, left ordinate) of the NH^{4+} absorption band at 1452 cm^{-1} (see the inset) and the current density through the microreactor (solid line, right ordinate) during application of -7 V. (b) Integrated area of the peak located at 1550 cm^{-1} as a function of time (left ordinate). For comparison the integrated intensities of the ammonium band located at 1452 cm^{-1} is presented as well (right ordinate). The experiments were accomplished in microreactor type **4**.

4.4. Conclusions and outlook

In this work we have shown the fabrication, characterization and application of ATR-IR microreactors in which an electric field can be applied over a gas or liquid medium. Electrical, mechanical and optical phenomena that may affect the interpretation of data from IR spectroscopy in the presence an electric field were highlighted. In particular, an in situ IR study of the dynamics of phonon excitation by E-field emitted electrons in gas and liquid phase was discussed. It was pointed out that the generation of phonons should not be confused with formation of species from a chemical reaction. Finally, some preliminary results were shown for the detection of CO_2 gas and ammonium ions in solution in presence of an electric field. The response of the CO_2 filled microreactor is dominated by temperature effects and no significant influence of the E-field on the CO_2 absorption band is found. It is demonstrated that it is possible to follow liquid phase reactions in situ, like the decomposition of ammonium to NO under influence of an electric field.

To be able to study the effect of E-field controlled surface polarization on desorption and adsorption processes relevant in heterogeneous catalysis, the microreactor has to be optimized further in order to prevent field electron emission from one electrode to the other. To this end, a thicker and better insulating layer should be applied on one of the electrode surfaces. It is trivial that the insulating layer cannot be on the surface where the ATR-IR is applied, because that would prevent the extension of the evanescent field of the attenuated IR beam into the reaction medium. The ratio of the E-fields over gap and insulator will be equal to the ratio of their dielectric constants. In case of silicon dioxide as the insulator, with a dielectric constant of *ca.* 3.9, and a dielectric strength of *ca.* 8.8×10^6 V/cm,[69] the E-field over the gap cannot be made higher than 3.43×10^7 V/cm, in order to avoid dielectric breakdown of the insulator film. As was discussed in this paper, literature on charged cationic central in e.g. zeolites indicates that the desired electric fields close to the surface should be in the range 6 to 30×10^7 V/cm. It is unlikely that E-fields with values at the high end of this range can be achieved with insulator materials known in microelectronics technology, but the lower end of this range may be feasible.

4.5. References

(1) Kreuzer, H. J.; *Surf. Interface Anal.*, **36**, (2004) 372

(2) Zhou, J.; Wang, Q.; Sun, Q.; Jena, P.; Chen, X. S.; *Proc. Natl. Acad. Sci.*, **107**, (2010) 2801

(3) Peineke, C.; Davoodi, P.; Seipenbusch, M.; Weber, A.; Schmidt-Ott, A.; *J. Nanosci. Nanotechnol.*, **11**, (2011) 8628

(4) Simmons, J. G.; *J. Appl. Phys.*, **34**, (1963) 1793

(5) Suchorski, Y.; Schmidt, W. A.; Block, J. H.; *App. Surf. Sci.*, **76**, (1994) 101

(6) Stipe, B.C.; Rezaei, M.A.; Ho, W.; *Phys. Rev. Lett.*, **81**, (1998) 1263

(7) Saedi, A.; van Houselt, A.; van Gastel, R.; Poelsema, B.; Zandvliet, H.J.W.; *Nano Lett.*, **9**, (2009) 1733

(8) Stipe, B.C.; Rezaei, M.A.; Ho, W.; Gao, S.; Persson, M.; Lundqvist, B.I.; *Phys. Rev. Lett.*, **78**, (1997) 4410

(9) Lee, J.; Sorescu, D.C.; Deng, X.; *J. Am. Chem. Soc.*, **133**, (2011) 10066

(10) Calvaresi, M.; Martinez, R. V.; Losilla, N. S.; Martinez, J.; Garcia, R.; Zerbetto, F.; *J. Phys. Chem. Lett.*, **1**, (2010) 3256

(11) Agiral, A.; Trionfetti, C.; Lefferts, L.; Seshan, K.; Gardeniers, J. G. E. (Han); *Chem. Eng. Technol.*, **31**, (2008) 1116

(12) Gaudioso, J.; Lee, H. J.; Ho, W.; *J. Am. Chem. Soc.*, **121**, (1999) 8479

(13) Concepcion, J. J.; House, R. L.; Papanikolas, J. M.; Mayer, T. J.; *Proc. Natl. Acad. Sci.*, **109**, (2012) 15560

(14) Le Saux, A.; Ruysschaert, J.-M.; Goormaghtigh, E.; *Biophys. J.*, **80**, (2001) 324

(15) Saggu, M.; Levinson, N. M.; Boxer, S. G.; *J. Am. Chem. Soc.*, **133**, (2011) 17414

(16) Handler, P.; Aspnes, E.; *J. Chem. Phys.*, **47**, (1967) 473

(17) Handler, P.; Aspnes, D. E.; *Phys. Rev. Lett.*, **17**, (1966) 1095

(18) Courtois, D.; Jouve, P.; *J. Mol. Spectrosc.*, **55**, (1975) 18

(19) Andanson, J.-M.; Baiker, A.; *Chem. Soc. Rev.*, **39**, (2010) 4571

(20) Mojet, B. L.; Ebbesen, S. D.; Lefferts, L.; *Chem. Soc. Rev.*, **39**, (2010) 4643

(21) Visart de Bocarmé, T.; Chau, T.-D.; Tielens, F.; Andrés, J.; Gaspard, P.; Wang, R. L. C.; Kreuzer, H. J.; Kruse, N.; *J. Chem. Phys.*, **125**, (2006) 054703

(22) Visart de Bocarmé, T.; Kruse, N.; Gaspard, P.; Kreuzer, H. J.; *J. Chem. Phys.*; **125**, (2006) 054704

(23) Xu, J.; Mojet, B. L.; Lefferts, L.; *Microporous Mesoporous Mater.*, **91**, (2006) 187

(24) Xu, J.; Mojet, B.L.; van Ommen, J.G.; Lefferts, L.; *J. Phys. Chem. B.*, **108**, (2004) 218

(25) Rogalski, A.; *Infrared Detectors*, CRC Press Taylor & Francis group, United States of America (2011) Refractive Index Database <http://refractiveindex.info>. Retrieved on Jan. 05, 2013

(26) Sze, S.M.; Ng, K.W.; *Physics of Semiconductor Devices*, John Wiley & Sons., Inc., United States of America, Hoboken, New Jersey, United States of America (2007)

(27) Mallardeau, C.; Morand, Y.; Abonneau, E.; *J. Electrochem. Soc.*, **136**, 238

(28) Shafiei, M.; Yu, J.; Arsat, R.; Kalantar-zadeh, K.; Comini, E.; Ferroni, M.; Sberveglieri, G.; Wlodarski, W.; *Sens. Act. B*, **146**, (2010) 507

(29) Engstrom, H.; *J. Appl. Phys.*, **51**, (1980) 5245

(30) Bhaskaran, M.; Sriram, S.; Short, K. T.; Mitchell, D. R. G.; Holland, A. S.; Reeves, G. K.; *J. Phys. D: Appl. Phys.*, **40**, (2007) 5213

(31) Grimaldi, M. G.; La Via, F.; Raineri, V.; *Europhys. Lett.*, **40**, (1997) 581

(32) Vereshchagina, E.; Wolters, R. A. M.; Gardeniers, J. G. E.; *J. Micromech. Microeng.*, **21**, (2011) 105022

(33) Ravindra, N. M.; Zhao, J.; *Smart Mater. Struct.*, **1**, (1992) 197

(34) Spindt, C.A.; Brodie, I.; Humphrey, L.; Westerberg, E.R.; *J. Appl. Phys.*, **47**, (1976) 5248

(35) Zhai, T.; Li, L.; Ma, Y.; Liao, M.; Wang, X.; Fang, X.; Yao, J.; Bando, Y.; Golberg, D.; *Chem. Soc. Rev.*, **40**, (2011) 2986

(36) Perea-López, N.; Rebollo-Plata, B.; Briones-León, J. A.; Morelos-Gómez, A.; Hernández-Cruz, D.; Hirata, G. A.; Meunier, V.; Botello-Méndez, A. R.; Charlier, J.-C.; Maruyama, B.; Muñoz-Sandoval, E.; López-Urías, F.; Terrones, M.; Terrones, H.; *ACS Nano*, **5**, (2011) 5072

(37) Boyle, W. S.; Kisliuk, P.; *Phys. Rev.*, **97**, (1955) 255

(38) Slade, P.G.; Taylor, E.D.; *IEEE Tr. Comp. Packaging Technol.*, **25**, (2002) 390

(39) Go, D.B.; Pohlman, D.A.; *J. Appl. Phys.*, **107**, (2010) 103303

(40) Li, Y.; Go, D.B.; *Appl. Phys. Lett.*, **103**, (2013) 234104

(41) Li, Y.; Tirumala, R.; Rumbach, P.; Go, D.B.; *IEEE Tr. Plasma Sci.*, **41**, (2013) 24

(42) Franz, G.; Low pressure plasmas and microstructuring technology, Springer 2009, Chapter 2, "Collisions and cross sections"

(43) Semnani, A.; Venkattraman, A.; Alexeenko, A.A.; Peroulis, D.; *Appl. Phys. Lett.*, **102**, (2013) 174102

(44) Chung, M. S.; Yoon, B.-G.; *J. Vac. Sci. Technology B*, **21**, (2003) 548

(45) Forbes, R.G.; *Nanotechnol.*, **23**, (2012) 095706

(46) Strong, F.W.; Skinner, J.L.; Tien, N.C.; *J. Micromech. Microeng.*, **18**, (2008) 075025

(47) Harrick, N.J.; *Phys. Rev. Lett.*, **4**, (1960) 224

(48) Fahrenfort, J.; *Spectrochim. Acta*, **17**, (1961) 698

(49) Karabudak, E.; Mojet, B. L.; Schlautmann, S.; Mul, G.; Gardeniers, H. J. G. E.; *Anal. Chem.*, **84**, (2012) 3132

(50) Herzig-Marx, R.; Queeney, K.; Jackman, R. J.; Schmidt, M. A.; Jensen, K. F.; *Anal. Chem.*, **76**, (2004) 6476

(51) Lukosz, W.; New Nanomechanical Integrated Optical Devices as Modulators, Switches, and Microphones; in: Proc. Micro System Technologies 90, 1st Int. Conf. Micro Electro, Opto, Mechanic Syst. Comp. Berlin, 10-13 Sept, 1990, Ed. H Reichl, Springer Berlin Heidelberg, 1990, pp.725-732

(52) Lukosz, W.; Pliska, P.; *Sens. Act. A*, **26**, (1991) 337

(53) Veldhuis, G.J.; Gui, C.; Nauta, T.; Koster, T.M.; Berenschot, J.W.; Lambeck, P.V.; Gardeniers, J.G.E.; Elwenspoek, M.; *Optics Lett.*, **23**, (1998) 1532

(54) Karabudak, E.; Yüce, S.; Schlautmann, S.; Hansen, O.;. Mul, G.; Gardeniers, Han (J. G. E.); *Phys. Chem. Chem. Phys.*, **14**, (2012) 10882

(55) Susarrey-Arce, A.; Tiggelaar, R.M.; Sanders, R.G.P.;. Geerdink, B.; Lefferts, L.; Gardeniers, J.G.E.; van Houselt, A.; *J. Phys. Chem. C*, **117**, (2013) 21936

(56) Busca, G.; Lorenzelli, V.; *Mater. Chem.*, **7**, (1982) 82

(57) Yang, C.-C.; Yu, Y.-H.; van der Linden, B.; Wu, J. C. S.;. Mul, G.; *J. Am. Chem. Soc.*, **132**, (2010) 8398

(58) Collins, S. E.; Baltanas, M. A.; Bonivardi, A. L.; *J. Phys. Chem. B*, **110**, (2006) 5498

(59) Khanna, R. K.; Moore, M.H.; *Spectrochim. Acta A*, **55**, (1999) 961

(60) Zhang, Y.; Bell, A. T.; *J. Catal.*, **255**, (2008) 153

(61) Dunne, J. A.; Rao, M.; Sircar, S.; Gorte, R. J.; Myers, A. L.; *Langmuir*, **12**, (1996) 5896

(62) Lamberti, C.; Bordiga, S.; Geobaldo, F.; Zecchina, A.; Otero Areán, C.; *J. Chem. Phys.*, **103**, (1995) 3158

(63) Blatter, F.; Moreau, F.; Frei, H.; *J. Phys. Chem.*, **98**, (1994) 13403

(64) Jousse, F.; Cohen De Lara, E.; *J. Phys. Chem.*, **100**, (1996) 233

(65) Kraus, M.; Eliasson, B.; Kogelschatz, U.; Wokaun, A.; *PhysChemChemPhys*, **3**, (2001) 294

(66) Hadjiivanov, K. I.; *Catal. Rev.*, **42**, (2000) 71

(67) De, D.; Kalu, E. E.; Tarjan, P. P.; Englehardt, J. D.; *Chem. Eng. Technol.*, **27**, (2004) 56

(68) Zhou, Z.-J.; Li, X.-P.; Liu, Z.-B.; Li, Z.-R.; Huang, X.-R.; Sun, C.-C.; *J. Phys. Chem. A*, **115**, (2011) 1418

(69) Osburn, C.M.; Ormond, D.W.; *J. Electrochem. Soc.*, **119**, (1972) 591

Supporting Information

1. Fabrication of microreactors with E-field

Figure SI-1 shows the schematic fabrication sequence of the microreactors. The process is performed on a set of two silicon wafers ((100)-oriented, double side polished, 5-10 Ω cm resistivity, 525 (±25) μm thickness, Okmetic Finland) of 100 mm diameter. At the bottom side of the top wafer an array of microdots is defined in Olin 907-17 photoresist, using mid ultraviolet (UV) photolithography (EVG 620, Electronic Vision). The resulting resist pattern is used as a protective pattern during deep reactive ion etching of silicon (DRIE, SF_6/C_4F_8 Adixen AMS100-SE) to fabricate arrays of 15 μm high micropillars (diameter 5 μm, pitch 20 μm) The process is described in detail in.[1, 2] Microfluidic access holes, defined with photolithography in photoresist (Olin **908-35**), were DRIE-etched (Adixen AMS100-SE) from the topside of the top wafer completely through the substrate. After each DRIE-step the photoresist was removed from the wafers with HNO_3 and H_2SO_4:H_2O_2 (3:1).

On the bottom side of the bottom wafer, which was coated with 300 nm silicon-rich silicon nitride (SiRN) deposited by a LPCVD process, a pattern is defined by mid-UV-photolithography in an Olin 907-17 photoresist layer. The SiRN layer is locally removed by reactive etching with an Elektrotech Twin system PF 340 (CHF_3/O_2), and after removal of the photoresist the SiRN acts as mask for anisotropic silicon etching in a 25 wt. % aqueous KOH solution at 75 °C for *ca.* 8 hours. This yields the side slopes composed of Si{111} planes which are needed to couple in the IR light. RCA cleaning (HCl:H_2O_2:H_2O, 1:1:5 vol.%) is carried out to remove residues left after etching in the KOH solution. After removal of the remaining SiRN coating in a 50 wt-% aqueous HF solution, a layer of 900 nm SiO_2 is deposited on the bottom wafer.

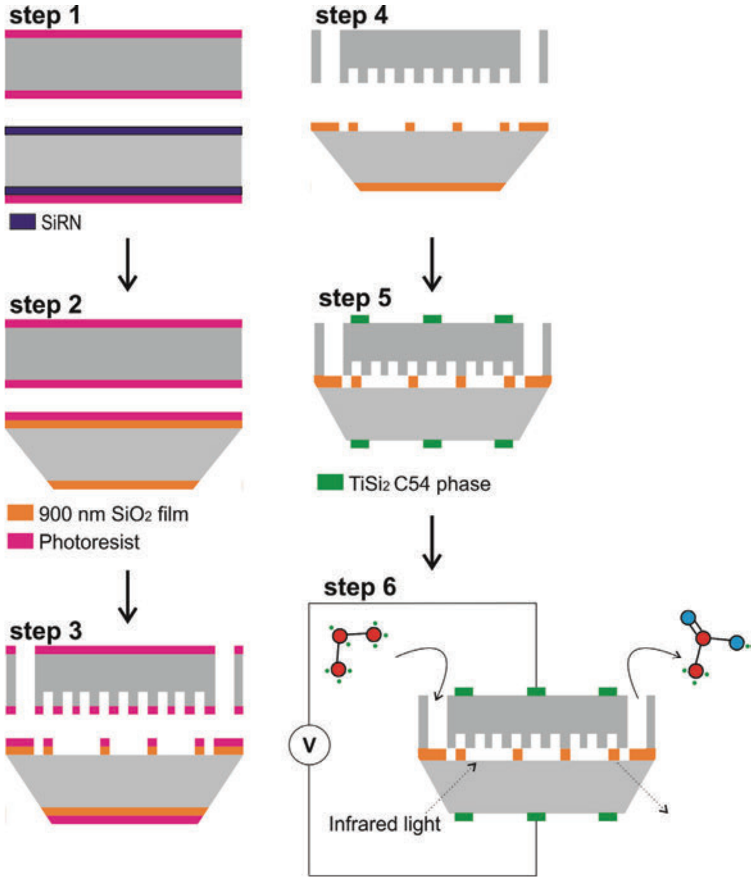

Figure SI-1. Schematic cross section of microreactor fabrication process (not on scale)

The topside of the bottom wafer is coated with photoresist Olin 907-17, which is photolithographically patterned to define a flow channel of *width* = 1.8 cm, *length* = 4.4 cm and *height* = 900 nm. The thickness of the SiO_2 layer defines the height of the flow channel. This layer is selectively removed by plasma etching (Adixen, AMS100-DE;C_4H_8/CH_4). In order to avoid bending or closure of the shallow flow channel during fusion bonding, a series of SiO_2 microstructures with a diameter of 50 to 100 μm and 900 nm height are embedded in the SiO_2 channel (see **Figure SI-1, step 3)**. After fabrication of the microchannel the photoresist is removed using HNO_3 and H_2SO_4:H_2O_2 (3:1; known as "Piranha" cleaning solution).

Ellipsometry measurements revealed that after Piranha cleaning *ca.* 10 nm of native oxide has formed on the exposed silicon areas. In addition, a pair of highly doped p^+-type silicon ATR-crystals is made from highly doped silicon substrates ((100)-oriented, double side polished, 0.01-0.02 Ω cm resistivity, 525 (±25) μm thickness, Okmetic Finland), following the same procedure as above, but with a KOH etching time of 9 hours.

After alignment and prebonding, fusion bonding was done at 1100 °C with a temperature ramp of 10 °C/min from 400 to 1100 °C under pure N_2 atmosphere (15 mL/min).

Prior to fabrication of the Ohmic contacts on the device, native oxide was removed by dipping the wafer stacks in 50% HF for 60 sec. The fluidic access holes were covered with blue tape (Adwill) to prevent access of HF solution which would damage the interior of the flow channel in SiO_2. A pattern of titanium (Ti) is sputter-deposited on top- and -bottom side of the stack by means of double-sided shadow-masking. Sputtering is done in a home-built system in argon atmosphere at a pressure of 0.66 Pa. After Ti deposition the wafer stacks are annealed in N_2 to obtain Ohmic $TiSi_2$ contacts (temperature ramp of 10 °C/min from 400 to 800 °C and constant at 800 °C for 30 min). Subsequently, the excess of Ti is removed with reactive ion beam etching (RIBE) in an Oxford i300 system (3.1×10^{-5} Pa in Ar), in which the amount of removed material is monitored with a mass spectrometer.

Finally, the wafer stacks are diced into individual microreactors of 2 cm x 5 cm with a DCD 321-Disco dicing machine.

To compare the electrical and optical properties of the fabricated devices, we also made two additional sets of ATR-IR microreactors by following the described recipe. After the growth of the 900 nm layer the wafers were dipped in 1 wt.-% HF aqueous solution to define the microreactor flow channel. However compared to the previous process, we have left a SiO_2 layer of ~120 nm ± 20 nm (see main article **Figure 3(3)**), which leads to a small change in the height of the nanochannel, making it *ca.* 800 nm high. In addition, the material of the top electrode containing the periodic array of micropillars was exchanged by highly boron doped (*p*$^+$-type) silicon (see main article **Figure 3(5)**).

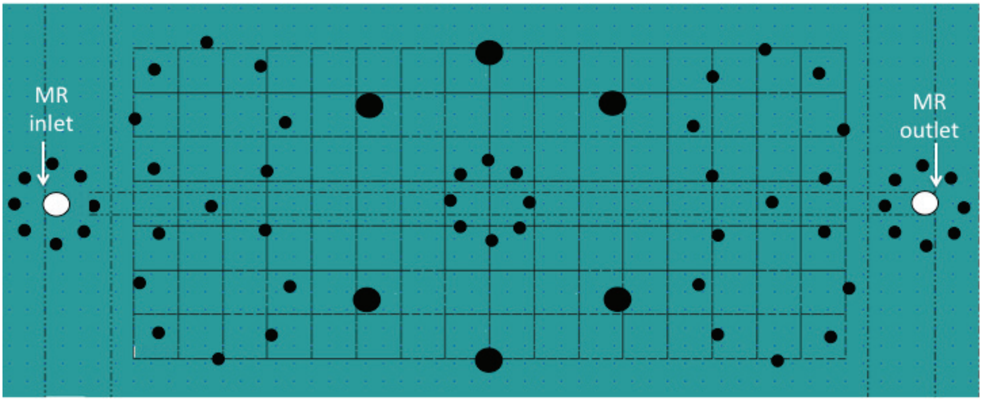

Figure SI-2. Schematic top view of the design of the microreactor (not on scale). The black closed circles are the supporting columns, which are either 50 μm (smaller circles) or 100 μm (larger circles) in diameter. The micro pillars are located within the area indicated by the grid (total area: 14 mm x 32 mm, grid size: 2 mm x 2 mm). The distance between the inlet and outlet holes (white circles) is 40 mm.

2. $TiSi_2$ structural characterization

The $TiSi_2$-C54 low resistivity phase is characterized by X-ray diffraction (XRD, X-pert IMS, Philips) and Raman spectroscopy (Senterra Raman microscope spectrometer). Results are given in **Figure SI-2**. XRD data show that annealing of the Ti thin film deposited on *p*-type silicon converted it to $TiSi_2$ by a solid state reaction, which is well-reported in literature.[3-6] Two crystalline phases are observed after annealing at 800 °C, see **Figure SI-2 (a)** spectrum (**1**). Furthermore, a Ti/Ti-Si mixed phase can be distinguished, which indicates that not all Ti is converted into $TiSi_2$. In order to remove either the remaining Ti or other undesired Ti-Si phases, the annealed film was etched for 10 minutes by RIBE with Ar-ions, leading to a specimen giving spectrum (**2**) in **Figure SI-2(a)**. This spectrum shows that after etching the film is more pure in terms of crystalline phases, but still shows diffractions of a Ti or Ti-Si phase. Therefore RIBE is continued for another 10 min, which results in a pure $TiSi_2$ phase, spectrum (**3**) in **Figure SI-2(a)**.

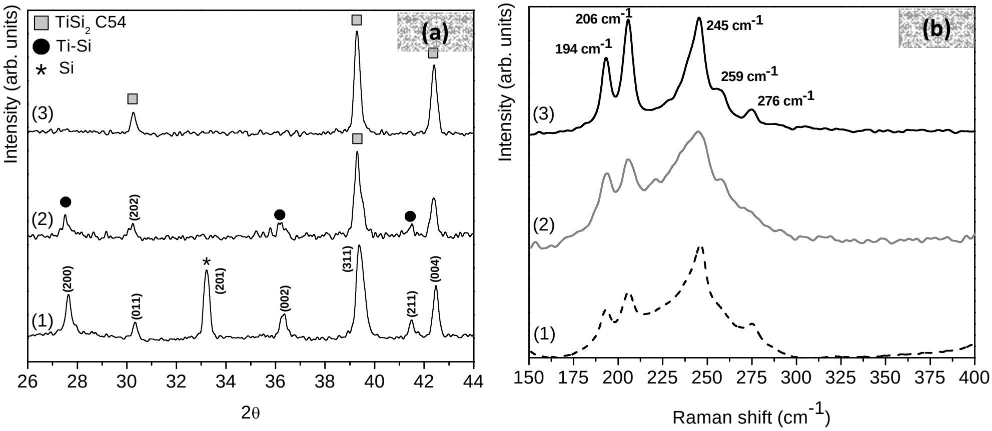

Figure SI-2. X-ray diffraction results (a) and Raman spectra (b) of Ti-films after annealing and RIBE-etching: (1) annealed Ti-film on Si (no RIBE-etching), (2) after 10 min RIBE-etching, and (3) after 20 min RIBE etching.

The same three film situations were studied by Raman spectroscopy. Curves (**1**) and (**2**) in **Figure SI-2(b)** show broad peaks can be observed, suggesting the presence of multiple crystalline phases.[7, 8] After 20 min RIBE curve (**3**) is obtained, which gives evidence for the formation of C54, with two narrow bands at ~190-206 cm^{-1} and a peak around 245 cm^{-1}, in agreement with reported values.[9] Also two small peaks located at 259 cm^{-1} and 276 cm^{-1} are found, which might indicate a remainder of the C49 phase.[8]

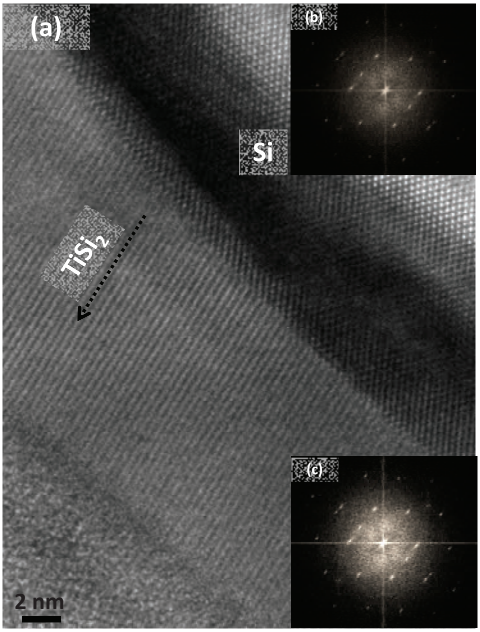

Figure SI-3. (a) TEM image showing a large crystal grain of C54 phase in a $TiSi_2$ thin film. (b) Fast Fourier Transform (FFT) of the image of the Si area, indicating the presence of Si{111} planes. (c) FFT of the $TiSi_2$ crystal phase.

TEM images of $TiSi_2$-C54 made with the electron beam parallel to the Si[011] zone axis are presented in **Figure SI-3.** From this and other images the $TiSi_2$ film thickness was estimated to be 18 ± 2 nm.

3. Experimental set-up for ATR-IR with or without applied E-field

The ATR-FTIR microreactor measurements are carried out in a Fourier Transform Infrared (FT-IR) spectrometer, Tensor 27, from Bruker Optics with a MCT D316/6-L detector. The microreactor is placed in a special cell, which allows to apply electrical connectors for the application of an electrical potential (**Figure SI-4**).

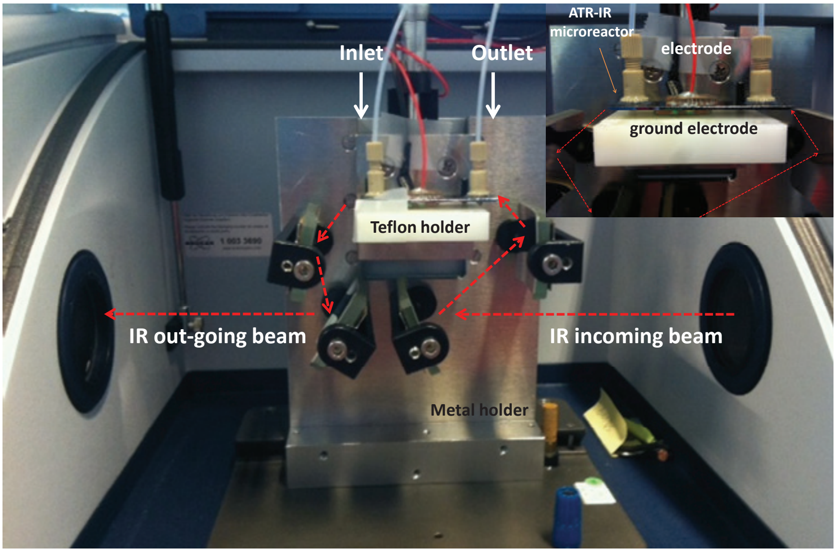

Figure SI-4. Photo of the ATR-IR microreactor mounted in an ATR-cell

The ATR cell consists of four concave polished mirrors mounted in a metal holder. Centered on the upper part of the metal holder, a Teflon chip holder is placed in-between the mirrors, which allows to connect PEEK microfluidic connections (Upchurch, Inacom Instruments). UV-curable glue (Nano-470 company) is used to fix the connections in order to realize gas-tight microfluidic accesses. To supply the E-field to the microreactor, two polished copper electrodes (2 cm x 2 cm, and 1 mm thick) are glued on the top-and bottom side of the microreactor with conductive silver glue (Sigma-Aldrich). The electrodes are aligned with the microfluidic channel and the $TiSi_2$ Ohmic contacts on the outside of the microreactor chip. It was verified that the presence of the metal layer combination $TiSi_2$/Ag/Cu decreases IR transmission by *ca.* 15% compared to only the $TiSi_2$ layer (**Figure 2**, *main chapter*). A Keithley 2410 combined source and measuring unit is used for applying electrical voltage and current sweeps and pulses. A Lab-View script is used to control the electrical field, as well as to read out the electronic measurement circuitry.

4. Options to reduce interference fringes as observed in IR spectra for microreactors with micromachined pillars

As described in the *main chapter*, fringes are observed in IR spectra for microreactors with pillars to which an electric field is applied. The intensity of the fringes depends on the applied electric field. These fringes obscure the parts of the spectrum above *ca.* 2000 cm^{-1}, and complicate the interpretation of this part of the spectrum. Two possible routes to avoid these complications have been identified:

i. Decrease the acquisition resolution to 8 cm^{-1} . The effect is shown in **Figure SI-5**.
ii. Use a Fast Fourier Transform filter, of which the result is shown in **Figure SI-6**.

Similar gas conditions as in **Figure SI-5** were used during FFT filtering of the IR signal. For the gas mixture a water absorption band is identified at 3256 cm^{-1}, which is in agreement with reported values for –OH stretching. The CO_2 peak cannot be distinguished at 1 cm^{-1}, neither in the CO_2 experiments for 4 cm^{-1} and 8 cm^{-1} at -75 V. Note that the applied potential plays a role in enhancing phonon absorption: the absence of phonon absorption at a voltage less than 40V (negative voltage) is therefore beneficial for CO_2 detection (**Figure SI-6**).

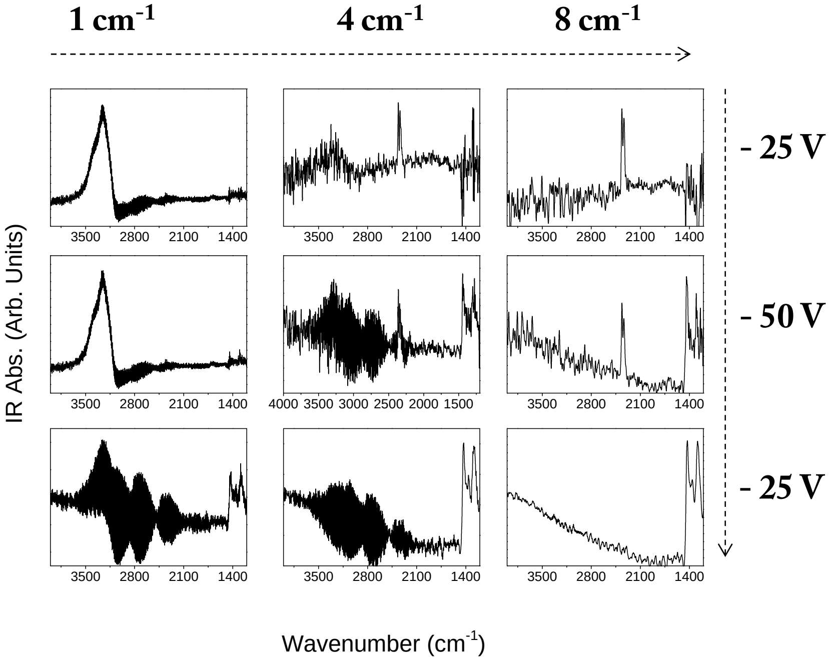

Figure SI-5. IR spectra at different potentials and spectral resolutions. From top to bottom: IR spectra at -25 V, -40 V and -75 V; from left to right resolutions of 1 cm^{-1}, 4 cm^{-1} and 8 cm^{-1}. A gas mixture of CO_2 with saturated H_2O vapor was used for recordings at 1 cm^{-1}, and pure CO_2 gas (99.9% purity) for the measurements at 4 cm^{-1} and 8 cm^{-1}.

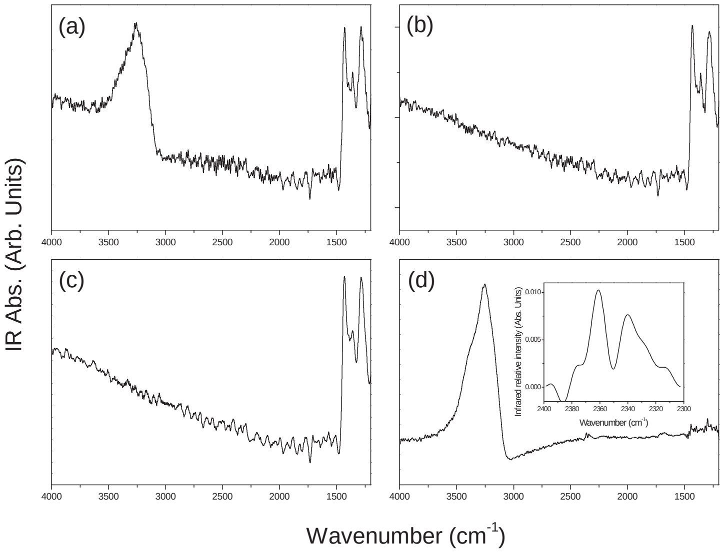

Figure SI-6. IR spectra at -75 V recorded at 1 cm^{-1} (a), 4 cm^{-1} (b) and 8 cm^{-1} (c). In (d) we present a -40 V collected at 1cm^{-1}

5. Mechanical deformation of the microreactor due to electrostatic forces

As discussed in the *main chapter*, a possible cause for the observed dependence of the intensity of the observed fringes on the magnitude of the electrical field applied to the microreactor may be the mechanical deformation of the microreactor due to the electrostatic attraction between the pillar tips and the opposite silicon part. The electrostatic attraction decreases the gap between pillar tips and ATR crystal surface, giving a "nanomechanical integrated-optical effect" by which the transmittance of IR light in our ATR crystal is modulated by the displacement of the pillar tips into the evanescent field of the IR light. As outlined in **Figure SI-7**, two mechanical deformation mechanisms can be identified:

i. **Compression of the supporting columns**;

ii. **Bending of the silicon material into which the pillars are micromachined**.

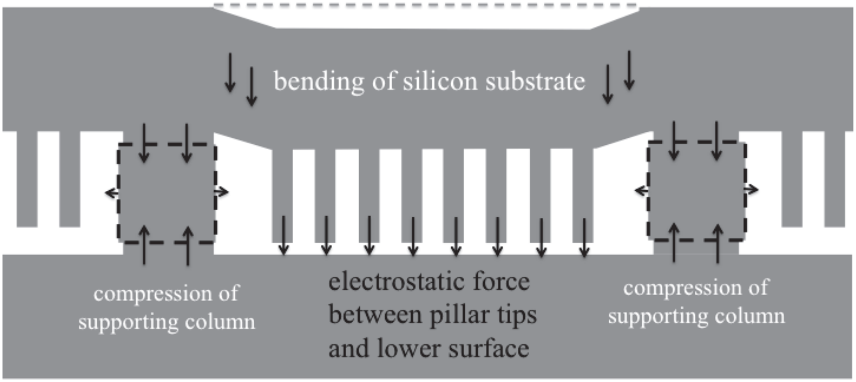

Figure SI-7. Schematic drawing (not on scale) of the two deformation mechanisms discussed in the text: bending of the silicon substrate, and compression (accompanied by a small lateral expansion due to Poisson effect) of supporting columns.

Below we will estimate how much these two effects will decrease the gap between the pillar tips and the opposite surface. We start by calculating the electrostatic force per unit area P_0 (in N m^{-2}) that the pillar tips will experience when an electric field is applied across the microreactor.

Following the method described in previous work from our institute,[10] the force per unit area is given by:

$$P_0 = \frac{\varepsilon_0 V^2}{2\left(d^0_{eff} - \delta\right)^2} \qquad \text{(SI-1)}$$

with ε_0 the dielectric constant in vacuum, V the voltage over gap and insulator (gas or gas + dielectric), δ the unknown final gap distance and d^0_{eff} the effective distance between the two plates (which is the original gap over which the voltage is applied, corrected for the dielectric constants of the materials in the gap), given by:

$$d^0_{eff} = \frac{d^0_{air}}{\varepsilon_{r,air}} + \frac{d^0_{SiO_2}}{\varepsilon_{r,SiO_2}} = d^0_{air} + \frac{d^0_{SiO_2}}{4.4} \qquad \text{(SI-2)}$$

The value of d^0_{eff} is 900 nm in case there is no silicon oxide present (the native oxide layer of *ca.* 3 nm can be neglected here), and 807 nm in case there is a silicon oxide layer of 120 nm present (leading to an air gap of 780 nm). This corresponds to microreactor types **4** and **3**/**5**, respectively (see *main chapter*).

We will assume an applied voltage V of 75 Volts, which was the highest voltage studied in our work, and this therefore is our "worst case" scenario in terms of microreactor deformation. For that voltage, with silicon oxide present between pillar tips and opposite silicon, and as a first approximation assuming that the deformation is so small that the change in the gap will be negligible (we will see later that this is a correct assumption), eq. (SI-1) gives a force/unit area of P_0 = 38.24 kPa. Note that this is the force exerted per unit of pillar tip surface area.

Based on the design of the microreactor and the micropillars and supporting columns micromachined in it, we calculate the following relevant surface areas:

$\boldsymbol{A_1}$ = total area of the micropillar tips = 21.95 mm^2 (this is also the area used in the calculation of current density from measured current values)

$\boldsymbol{A_m}$ = area of the "membrane", i.e. the maximum area of silicon substrate suspended by a certain number of supporting columns (a worst case situation) = 50 mm^2

$\boldsymbol{A_2}$ = total surface area of pillars present on the "membrane" = pillar density x $\boldsymbol{A_m}$ = 2.21 mm^2

$\boldsymbol{A_3}$ = total cross-sectional area of the supporting columns = 0.126 mm^2

$\boldsymbol{A_R}$ = total area on which pillars or columns are located, taken as the length times the width of the microreactor cavity = 448 mm^2.

i. **Compression of the supporting columns.**

We take a simple model in which a number of supporting columns are axially loaded by the compressive force given by **eq. (SI-1)**. The original total cross-sectional area of the bars is $\boldsymbol{A_3}$, the axial force (assumed equally distributed over this area $\boldsymbol{A_3}$) applied on the bars is P_0 $\boldsymbol{A_1}$ (here we take all the supporting columns and all the pillars present in the microreactor, and we neglect any effect of the supporting frame of the microreactor). The compression of the bars is given by:

$$\delta = \frac{P_0 A_1 L}{E A_3} \qquad \text{(SI-3)}$$

with E the Young's modulus of silicon in the direction perpendicular to a Si{100} surface, i.e. 130 GPa, and L the original length of the columns, i.e. 15.9 μm. Inserting the calculated force per unit area, and the estimated respective surface areas, leads to a gap change δ of 0.81 nm, or 0.10 % of the original gap.

ii. Bending of the silicon substrate.

We approximate the bending of the substrate by the deflection of a clamped circular flat (i.e. we neglect the presence of the pillars) plate under a uniform applied pressure P, which is given by Ref. [11]:

$$w(r) = \frac{Pa^4}{64D}\left\{1-\left(\frac{r}{a}\right)^2\right\}^2 \quad \text{(SI-4)}$$

with r the radial coordinate ($r = 0$ at the center of the plate), a the radius, and D the flexural rigidity of the plate, which is given by:

$$D = \frac{Eh^3}{12(1-\nu^2)} \quad \text{(SI-5)}$$

with h the thickness of the plate, E the Young's modulus (here we take 150 GPa[12]) and ν the Poisson's ratio of silicon (0.17), respectively. The silicon wafers from which the microreactors are fabricated are *ca.* 525 μm thick, so that with a pillar height + gap of 15.9 μm the value of h becomes 509.1 μm. The maximum deflection of the plate will be at the center, i.e. for $r = 0$.

The force applied on the membrane (assumed equally distributed over the membrane area $\boldsymbol{A}_m$) is $P_0\, \boldsymbol{A}_2$, therefore P in Eq. (SI-4) equals $P_0\, \boldsymbol{A}_2 / \boldsymbol{A}_m = 1.69$ kPa. Filling in all the numbers in Eqs. (SI-5) and (SI-4) leads to $w = 3.94$ nm or 0.44 % of the original gap of 900 nm.

6. IR absorption spectra of adsorbed NO compounds

We have studied the decomposition of ammonium ($NH_4^+{}_{(aq)}$) upon application of an external potential to microreactor type **4** through which a solution of NH_4Cl in water was flown at a rate of 30 μL/min. IR spectra were recorded with a resolution of 8 cm^{-1} and displayed from 1720 cm^{-1} to 1520 cm^{-1} in **Figure SI-9**.

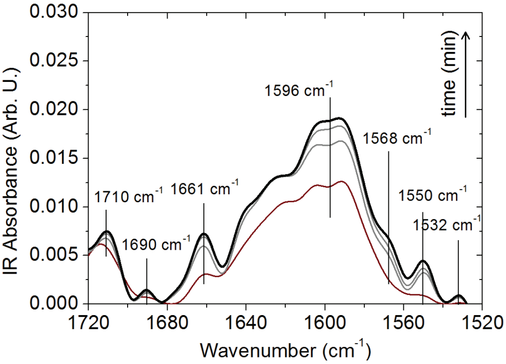

Figure SI-8. Recorded IR spectra employed to calculate the integrated area of the band at 1550 cm^{-1} assigned to the IR absorption of NO in the ATR-IR microreactor. The other observed peaks will be discussed elsewhere. For more insights in the assignment of the peaks consult reference [13-14].

References

(1) Susarrey-Arce, A.; Marín, Á. G.; Schlautmann, S.; van Houselt, A.; Lefferts, L.; Gardeniers, J.G.E.; *J. Micromech. Microeng.*, **23**, (2013) 025004

(2) Tran, T.; Staat, H. J. J.; Susarrey-Arce, A.; Foertsch, T. C.; van Houselt, A.; Gardeniers, J. G. E.; Prosperetti, A.; Lohse, D.; Sun, C. *Soft Matter*, **9**, (2013) 3272

(3) Yang, J.-M.; Park, J.-C.; Park, D.-G.; Lim, K.-Y.; Lee, S.-Y.; Park, S.-W.; *J. Appl. Phys.*, **94**, (2003) 4198

(4) Mann, R. W.; Miles, G. L.; Knotts, T. A.; Rakowski, D. W.; Clevenger, L. A.; Harper, J. M. E.; D'Heurle, F. M.; Cabral, C. Jr.; *J. Appl. Phys.*, **67**, (1995) 3729

(5) Chenevier, B.; Chaix-Pluchery, O.; Matko, I.; Madar, R.; La Via, F.; *Microelectronic Engineering*, **55**, (2001) 115

(6) Vereshchagina, E.; Wolters, R. A. M.; Gardeniers, J. G. E.; *J. Micromech. Microeng.*, **21**, (2011) 105022

(7) Tan, S. C.; Liu, L.; Zeng, Y. P.; See, A.; Shen, Z. X.; *Journal of the Electrochemical Society*, **152**, (2005) G754

(8) Meinardi, F.; Moro, L.; Sabbadini, A.; Queirolo, G.; *Europhys. Lett.*, **44**, (1998) 57

(9) Fringeli, U. P.; *Encyclopedia of spectroscopy and spectrometry* (Ed. John C. Lindon), Academic Press 2000, United States of America, San Diego California, 58-74

(10) Veldhuis, G.J.; Gui, C.; Nauta, T.; Koster, T.M.; Berenschot, J.W.; Lambeck, P.V.; Gardeniers, J.G.E.; Elwenspoek, M.; *Optics Letters*, **23**, (1998) 1532

(11) Timoshenko, S.; Woinosky-Krieger, S.; *Theory of Plates and Shells*, McGraw Hill, Classic Textbook Reissue, 1987, 2nd ed.

(12) Spiering, V.L.; Bouwstra, S.; Spiering, R.M.E.L.; *Sens. Act. A*, **39**, (1993) 149

(13) Medernach, J. W.; *Handbook of Vibrational Spectroscopy* (Ed. John M. Chalmers, Peter Griffiths), John Wiley & Sons Inc., Germany 2006, Vol. 4

(14) Hadjiivanov, K. I.; *Catal. Rev.*, **42**, (2000) 71

5

A newly developed ATR-IR Microreactor

The study of interstitial oxygen (O_i) defects

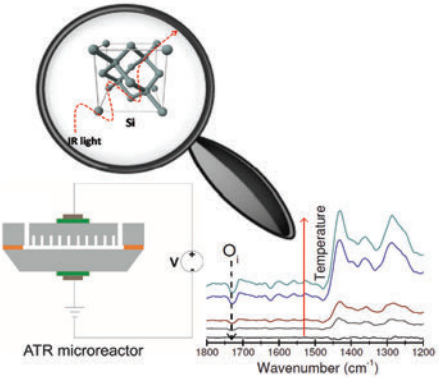

In this work we study oxygen interstitial defects (O_i) in a silicon-technology-based microreactor with an integrated attenuated total internal reflection (ATR) crystal as a function of an externally applied potential by means of attenuated total internal reflection infrared spectroscopy (ATR-IR). A reduction of the 1727 cm^{-1} O_i IR absorption band is observed with increasing potential. We evidence that this band is related to the presence of O_i, which enables detection of O_i by ATR-IR spectroscopy. The observed reduction with increasing potential is ascribed to an increase in temperature, due to resistive heating of the silicon.

Parts of this chapter has been published as

A. Susarrey-Arce, R.M. Tiggelaar, R.G.P. Sanders, B. Geerdink, L. Lefferts, J.G.E. Gardeniers and A. van Houselt, Temperature Dependence of the 1727 cm^{-1} Interstitial Oxygen Absorption Band Studied by ATR-IR in a Newly Developed Microreactor, *J. Phys. Chem. C*, **117**, (2013) 21936

5.1. O_i in silicon

Silicon is a widely used material in the semiconductor manufacturing of electronic devices like solar cells,[1, 2] transistors[3, 4] and power devices.[5] A critical issue for the performance of silicon based devices are the oxygen and carbon impurities in the crystal lattice. The presence of oxygen in silicon may be both beneficial and detrimental for the performance of silicon based devices. The presence of oxygen can improve the mechanical strength of the silicon and oxygen precipitates act as trapping centers for undesired (metal) impurities. The oxygen precipitates, on the other hand, can dramatically lower the electrical properties of the silicon, resulting in low efficiency or the failure of the device.[3, 4] Czochralski grown Si (Cz-Si) is the common method used for manufacturing the high quality silicon needed for microelectronic devices. The method consists of holding molten Si in a crucible, dipping a single-crystal silicon seed into the melt, and then slowly withdraw vertically, whereby the liquid Si crystallizes around the seed, thus forming a large (current target: 450 mm diameter) single crystal.[4] During the growth process oxygen and carbon from the quartz crucible and graphite heaters diffuse into the molten silicon and are, hence, built in into the Si crystal. Using the float-zone (FZ) growth technique, in which a radio-frequency coil is used to melt a narrow zone in a vertically mounted polycrystalline silicon rod, wafers of a very high purity can be produced.[6] Common techniques that have been used to measure the concentration of O_i include gas fusion analysis, mass spectrometry and infrared (IR) detection.[6]

The use of vibrational spectroscopy to study interstitial oxygen (O_i) was initiated by Kaiser *et al.*[7] These authors studied the temperature dependence of the most pronounced IR vibrational absorption band at 1108 cm^{-1} and attributed this to the asymmetric stretching mode of the nonlinear Si-O-Si quasimolecule with C_{2v} symmetry. Their model was used intensively to explain the observed O_i infrared absorption bands.[4, 8-10] Within their model the weak absorption band at 1720 cm^{-1}, which is observed around 1748 cm^{-1} at cryogenic temperatures,[11] is explained as a combination of the asymmetric mode at 1108 cm^{-1} and a transverse acoustic + transverse optical two-phonon combination.[9] It has, however, lately been calculated[12-14] that a linear $Si_3{\equiv}Si{-}O{-}Si{\equiv}Si_3$ quasimolecule (with D_{3d} symmetry) describes the O_i defect more accurately. Based on these calculations, combined with a study of isotope effects on O_i,[15] the O_i absorption at 1720 cm^{-1} is attributed[11, 14] to a combination of the O_i asymmetric stretching mode of A_{2u} symmetry and the O_i symmetric stretching of A_{1g} symmetry around 600 cm^{-1}. The latter mode is Raman active, but infrared inactive and only indirectly observed in combinations with other infrared active modes.[11, 15]

We have developed a silicon based microreactor with integrated electrodes for the application of electrical fields (E-fields) and an integrated Si ATR crystal that allows *in situ* characterization of processes driven by an externally applied potential. We envision applications of this microreactor in the field of (photo)catalytic chemistry and photovoltaics.

In this study this microreactor is used to follow the time course of the induced O_i asymmetric vibration (A_{2u}) during an externally applied electrical potential. We observe a decrease in the weak ~1720 cm^{-1} absorption band with increasing potential. We evidence the assignment of this peak to the presence of O_i and explain the decrease with increasing voltage as a consequence of temperature rise due to resistive heating of the silicon.

5.2. Experimental section

5.2.1. Fabrication of the internal reflection elements and ATR-IR microreactors

This study is performed using Cz-Si based homemade ATR internal reflection elements (ATR-IRE) and microreactors with an integrated ATR-IRE. The trapezoidal ATR-IRE (500 Ω-cm thick, lateral dimensions 50 × 20 mm, *p*-type Si (100), with 5-10 Ω-cm resistivity from Okmetic, Finland) is made after depositing 300 nm of silicon-rich silicon nitride (SiRN).

The IRE facets are defined in Olin 907-17 photoresist, using mid ultraviolet (UV) photolithography. This SiRN layer is patterned by reactive etching with a Elektrotech Twin system PF 340, and after removal of the photoresist this SiRN acted as mask for wet chemical anisotropic silicon etching with 25 w. % KOH at 75 ^{o}C for 8 hours which yielded the IRE facets (which are {111} planes with an angle of 54.7° with respect to the {001} surface plane of the crystal). Subsequently a cleaning step ($HCl:H_2O_2:H_2O$, 1:1:5 vol. %) is performed to remove the residues left after the KOH etching step. After subsequent removal of the SiRN mask layer (50% HF), 2 μm of SiO_2 are deposited on the wafers at 1150 ^{o}C by steam oxidation. Such an oxidation process is known to yield a well-controlled O_i concentration gradient in the Si-IRE4. To remove the grown SiO_2, the ATR crystal is dipped into 50% HF for 60 s. followed by cleaning with deionized water and drying. Finally, the wafers were diced into individual Si crystals of 2 cm x 5 cm with a DCD 321-Disco dicing saw machine. Two flat-polished (2 cm x 2 cm, and 1 mm thick) copper electrodes for application of the voltage are glued on the top and bottom side of the IRE with a conductive silver glue (Sigma-Aldrich).

To fabricate the ATR-IR microreactors a subsequent step, described elsewhere[16, 17] is performed after the growth of a SiO_2 layer which acts as an insulating layer between the two electrodes in the microreactor. The top-electrode of the microreactor contains a periodic array of micropillars (see **chapter 2** and **chapter 3**)[17, 18] which, due to their curvature, enhance the local electric field (see **chapter 4**).[16] The interspace between the top and the bottom electrode, i.e. of the micropillars and the ATR-IRE surface, is 2 μm.

In addition, for comparison measurements with a commercial float-zone (FZ)-Si IRE from Harrick scientific (2 mm thick, lateral dimensions 50 × 20 mm, *n*-type, resistivity > 50Ω/cm) were performed (see the configuration in **Figure 1a(1)**). Prior to the ATR-IR measurements, the commercial ATR crystal was dipped into a 50 % HF solution to remove any naturally formed oxide.

5.2.2. Optical and electrical experiments

The ATR crystal and the microreactor were placed in an ATR unit which consists of four concave polished mirrors mounted on a metal holder. A Keithley 2410 power supply programmed via a home-written Labview script was used to apply the voltage sweeps and pulses and to record the response.

Schematic cross-sections of the ATR-IRE and ATR microreactor are provided in **Figure 1(a)**. In the experiments described the E-field is established by applying a positive potential to the top electrode of the chip, whereas the bottom electrode (the one on the ATR-crystal) is connected to ground. The inversed situation (positive potential on the bottom electrode, the top one grounded) was also checked and significant changes in the infrared spectra were not observed. Hence the measurements shown in this work are obtained with a positive potential on the top electrode. All the measurements were performed under He flow (~ 0.05 mL/min). IR measurements were recorded using a FTIR spectrometer (Tensor 27, Bruker Optics) with a MCT D316/6-L detector with a resolution of 8 cm^{-1}. Raman measurements were performed at room temperature with a resolution of 9 cm^{-1} using the Senterra spectrometer (Bruker Optics) equipped with Peltier cooled CCD detector, using an excitation wavelength of 532 nm (20 mW), a 50 x objective lens with a numerical aperture of 0.75, leading to a spot diameter of ~0.9 μm, a laser irradiance of ~3.4 MW/cm^2 and a penetration depth of ~0.7 μm.

Temperature measurements were performed in static air by placing two thermocouples (Thermocoax-TC standard 2 AB type K) in the inlet and outlet of the flow channel, in contact with the IRE. The temperature values form both thermocouples were similar, indicating the absence of spatial temperature gradients in the IRE.

5.3. Results and discussion

In **Figure 1(b)** the recorded ATR-IR backgrounds (single beam transmittance) obtained with the home-made ATR-IRE (1), the microreactor under ~ 0.05 mL/min He flow (2) and the commercial ATR-IRE (3) are shown. Each spectrum was collected at room temperature with a resolution of 8 cm^{-1}. The ATR-IR measurements presented henceforth are recorded against these background signals.

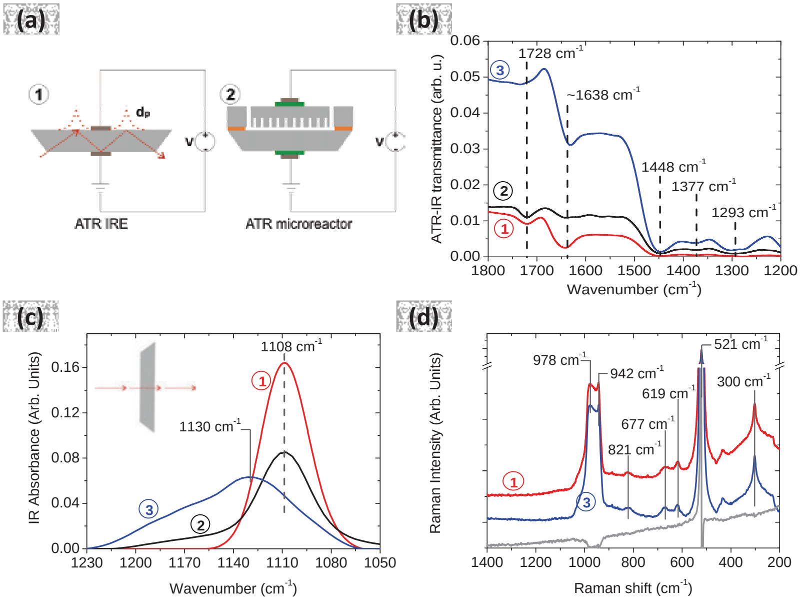

Figure 1. (a) Cross sectional representation of an ATR-IRE crystal (1) and an ATR-IR microreactor (2), with in (1) the incoming and outgoing IR beam represented by dashed (red) arrows and the evanescent wave with a penetration depth (d_p) of *ca.* 500 nm represented by the dotted red line. (b) Single beam background transmittance spectra of (1) the home-made ATR-IRE, (2) the ATR-IR microreactor and (3) the commercial ATR-IRE. (c) IR measurements (absorbance measured with the long axis of the Si samples perpendicular to the propagation direction of the IR beam, see the scheme in the inset) of: (1) the ATR-IR microreactor, (2) the homemade ATR-IRE and (3) the commercial ATR-IRE. In (d) Raman absorption spectra of (1) the home-made ATR-IRE and (3) the commercial IRE are shown from 1400 cm^{-1} to 200 cm^{-1}. The gray line in (d) is the difference spectrum between spectrum (1) and (3).

In all spectra in **Figure 1(b)** a decrease in intensity around 1500 cm^{-1} is observed, which is the onset of the low wavenumber cut-off in the Si IREs. This multi-phonon absorption low wavenumber cut-off is shifted to higher wavenumbers in ATR experiments compared to transmission experiments, as a consequence of the much longer optical pathway due to the multiple internal reflections in ATR mode. Absorption peaks are observed at 1727 cm^{-1}, 1638 cm^{-1}, 1448 cm^{-1}, 1377 cm^{-1} and 1293 cm^{-1}. The IR peaks at 1448 cm^{-1}, 1377 cm^{-1} and 1293 cm^{-1}, which are visible in all the ATR-IR spectra in **Figure 1(b)**, correspond to absorption of phonons in crystalline Si.[16,19] The band at 1638 cm^{-1}, which is also present in all the spectra, corresponds to the H-O-H scissor bending and is attributed to the presence of water at the interface. The absorption band at 1727 cm^{-1}, which is clearly present in spectra 1 and 2 of the Cz-Si devices and virtually absent in spectrum 3 of the commercial FZ-Si IRE, is attributed to the presence of interstitial oxygen (O_i).

In order to substantiate our attribution of the 1727 cm^{-1} absorption to O_i, we performed transmission measurements, in a configuration where the long axis of the IRE or microreactor is perpendicular to the travelling direction of the infrared light, for all three samples (see **Figure 1(c)**). Raman spectra of the home made IRE and the commercial IRE are shown in **Figure 1(d)**. The absorbance spectra in **Figure 1(c)** allow us to verify the presence of the O_i asymmetric stretching mode at 1108 cm^{-1}, which is, due to the low wavenumber cut-off around 1500 cm^{-1}, invisible in the ATR spectra in **Figure 1(b).** Indeed, in the spectra of both Cz-Si devices, i.e. the home build IRE (spectrum 1) and the microreactor (spectrum 2), the O_i asymmetric stretching mode at 1108 cm^{-1} is clearly observable. In spectrum 3 of the FZ commercial Si IRE this peak is not observed. Note that this commercial IRE is 4 times thicker than the home made IREs and also that the spectra in **Figure 1(c)** are not normalized. Spectrum 3 actually shows a distinct peak at 1130 cm^{-1} and weak shoulders around 1170 cm^{-1} and 1190 cm^{-1}, hence confirming the much lower concentration of O_i in the commercial IRE and the assignment of the band at 1727 cm^{-1} to O_i. The peak at 1130 cm^{-1} and the shoulders at higher wavenumbers are usually assigned to SiO_2 vibrations[8] in the native oxide layer and are not discussed here in further detail. The intensity of the 1727 cm^{-1} absorption band in our samples is too low to be observed in transmission measurements.[9]

Raman spectra, shown in **Figure 1(d)**, are recorded to check the presence of the O_i symmetric stretching of A_{1g} symmetry around 600 cm^{-1}, which is only Raman active. The spectra show bands which are characteristic[20-23] of (multi) phonons in silicon at 978 cm^{-1}, 942 cm^{-1}, 521 cm^{-1} and 300 cm^{-1}. The bands at 821 cm^{-1} and 677 cm^{-1} have been assigned to SiO_2 network vibrations[24] and a Si-O stretching mode[25], respectively. The band at 619 cm^{-1} has been assigned to the presence of B dopants[26], although early observations in P doped samples are available,[21, 27] while others assign it to a two-phonon scattering process.[27, 28] The presence of a thin native silica layer makes it worthwhile to mention that also breathing modes of Si-O-Si three-membered rings are observed[29] around 606 cm^{-1}. Note that the combination of the Raman absorption band at 619 cm^{-1} and the O_i asymmetric stretching mode at 1108 cm^{-1}, would exactly result in absorption at 1727 cm^{-1}. In that case, one would expect to observe differences in the Raman spectra for the Cz-Si and the FZ-Si around 600 cm^{-1}. Since we do not observe these differences (see the difference spectrum in **Figure 1(d)**) we find no conclusive experimental evidence for the assignment of the 619 cm^{-1} absorption as the O_i symmetric stretching vibration (with A_{1g} symmetry).

In **Figure 2(a)** representative infrared spectra are shown in the region from 1800 cm^{-1} to 1200 cm^{-1} obtained during the application of an electrical voltage of 100 V over the microreactor gap for 30 min (see the configuration in **Figure 1a(2)**). During the experiment the absorption peaks attributed to phonon-excitations at 1431 cm^{-1}, 1357 cm^{-1} and 1290 cm^{-1} increase. In detail, a red-shift upon applying a potential is observed for the phonons bands in the IR spectra (compare **Figure 2(a)** with **Figure 1(b)**). As will be evidenced below, the temperature is increasing during our experiment. It is known that an increase in temperature results in a red-shift in the phonon absorption bands.[30, 31]

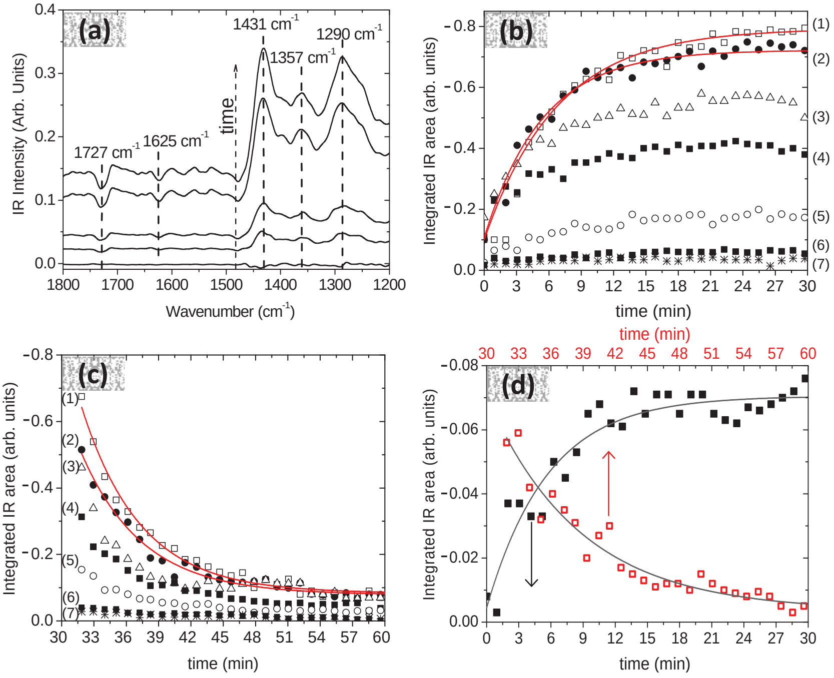

Figure 2. (a) ATR-IR absorption spectra as a function of time for the fabricated microreactor at 100 V. In (b), the integrated peak intensity of the 1727 cm^{-1} O$_i$ absorption peak is plotted as a function of time. From (1) to (7), the applied potentials are 100 V, 85 V, 80 V, 75 V, 65 V, 55 V and 50 V, respectively. In (c), the intensity of the 1727 cm^{-1} O$_i$ absorption peak after switching off the potential is presented as a function of time. In (d) the integrated intensity of the 1727 cm^{-1} O$_i$ absorption peak is shown as function of time for the home-made ATR-IRE during application of 10 V (solid squares) and after switching off the potential after 30 min (empty red squares). Note the negative numbers on the *y*-axes in (b)-(d). Fits to exponential growth or decay are added in (b)-(d) for the most intense plots. The errors in (b)-(d) range from ~5% for the highest intensities to ~40% for the lowest intensities.

It can be observed in the spectra (measured against the background in **Figure 1(b)**) in **Figure 2(a)** that when the phonons bands grow-upwards, the 1625 cm^{-1} and 1727 cm^{-1} peaks grow-downwards, i.e. the phonon absorption increases, while the absorption at 1625 cm^{-1} and

1727 cm^{-1} decreases compared to the respective absorptions in **Figure 1(b)**. The peak at ~1625 cm^{-1} is assigned to water desorbing from the interface of the crystal, and the band at 1727 cm^{-1} is related to O_i, as evidenced above. The decrease in intensity of the peak at ~1625 cm^{-1} is accompanied by a decrease in the intensity of the OH stretching vibration around ~3400 cm^{-1} (not shown). The integrated intensity of this negative absorption peak at 1727 cm^{-1} during experiments of 30 min each at different voltages (ranging from 100 V (curve 1) to 50 V (curve 7)) is shown in **Figure 2(b)**. The intensity curves follow first order growth kinetics, reaching a steady state in about 10 min When the power supply is switched off (after 30 min, see the curves in **Figure 2(c)**) an exponential decay is observed, which is the recovery of the 1727 cm^{-1} absorption peak. For comparison the same experiments as in **Figure 2(b)-2(c)** are performed with a home build Cz-Si ATR crystal at 10 V (in the configuration shown in **Figure 1(a)**). The resulting current (in steady state) reaches a value of 21.1 mA, which is similar to the current through the ATR microreactor when a bias of 100 V is applied (see the upmost curve in **Figure 2(b)**) The integrated intensity of the 1727 cm^{-1} O_i negative absorption peak during this experiment is shown in **Figure 2(d)**. For voltages below 10 V, no decrease in the 1727 cm^{-1} O_i absorption peak intensity was observed with the home build Cz-Si ATR crystal. For an applied potential of 10 V the decrease of the 1727 cm^{-1} O_i absorption peak intensity is roughly 10 times weaker in the home build ATR crystal compared to the microreactor (see **Figures 2(d)** and **(b)**).

In **Figure 3** we present contour plots of the phonon absorption bands when a potential of 100 V is applied for 30 min, followed by an off period of 30 min for the microreactor (**Figure 3(a)**) and when a potential 10 V is applied for 30 min, followed by an off period of 30 min for the home-made ATR-IRE (**Figure 3(b)**). The phonon absorption intensity in **Figure 3(b)**, which is just at the edge of the detection limit, is roughly 10 times weaker compared to the phonon absorption in the microreactor in **Figure 3(a)**. Thus a decrease in the

1727 cm^{-1} O_i absorption peak intensity is accompanied by an increase in the phonon absorption intensity. This observation conflicts with the explanation of the 1727 cm^{-1} O_i absorption peak being a combination of the asymmetric mode (at 1108 cm^{-1}) and a phonon combination,[9] but rather points at a common origin for the decrease in the 1727 cm^{-1} O_i absorption peak and the increase in the phonon absorption intensity in our experiments.

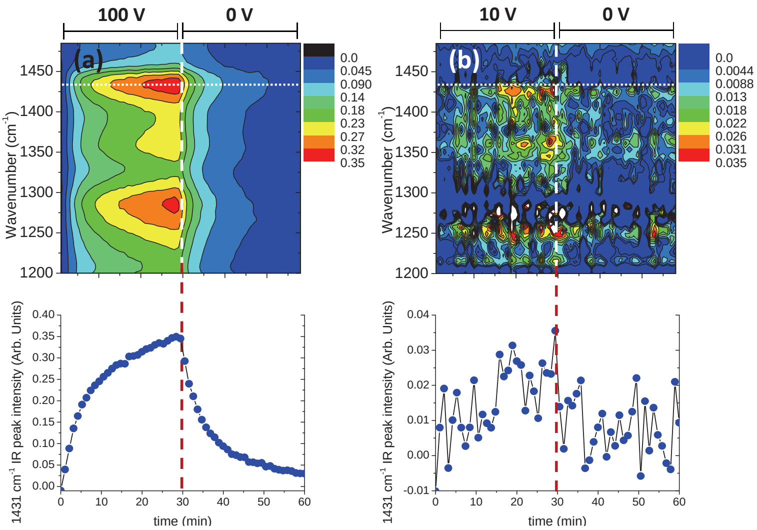

Figure 3. Contour plots of the ATR-IR absorption from 1485-1200 cm^{-1} and line profiles (along horizontal dashed lines) of the 1431 cm^{-1} phonon absorption during phonon excitation as a function of time for the (a) ATR-IR microreactor (voltage difference 100 V) and (b) home-made ATR-IRE (voltage difference 10 V). The vertical dashed line marks the moment at which the potential is switched off.

So what is the origin of the decrease in O_i absorption peak at 1727 cm^{-1} with applied electrical field? An intuitive answer would be that the interstitial oxygen defects drift away. This interpretation is, however, unlikely. Firstly, where should the interstitial oxygen defects go to be not detectable by the IR beam? We probe the interstitial oxygen throughout the ATR-crystal, so even if interstitial oxygen defects would travel, they would remain detectable by the IR beam and there would not be such a significant change in the integrated intensity as we observe. Secondly, to be able to drift in reaction to an applied potential, the interstitial oxygen defects should be charged and we have no indication that this is the case. Thirdly, one would not expect drift-motion to react on the time scale of min to an applied E-field, but rather within seconds.[32] Lastly, we do not observe notable changes when we reverse the E-field direction across the microreactor, which one would expect for E-field driven motion.

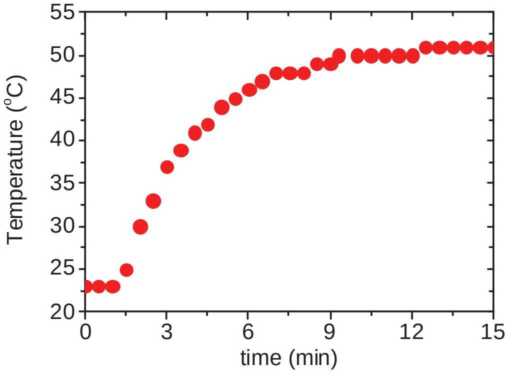

Figure 4. Temperature progress in the ATR-IR microreactor during application of a potential of 100 V.

The observed behavior is better explained as an increase in temperature, due to power dissipation in the microreactor or IRE. An increase in temperature may result in a lower integrated intensity via the thermal depopulation of the ground state of the transition, which is observed for the O_i 1727 cm^{-1} absorption at cryogenic temperatures by Hallberg *et al.*[11] To test this hypothesis the temperature progress in the microreactor, while applying a potential of 100 V, was measured as described in the experimental section. The temperature progress is shown in **Figure 4**. The temperature followed a profile which is very similar to the profiles in **Figure 2b**, reaching a steady value of 51 °C, suggesting a direct relation between the applied potential and the temperature. **Figure 5(a)** shows the measured temperature in the microreactor and the current through the microreactor as a function of the applied potential, confirming that both temperature and current correspond directly to the applied potential. **Figure 5(b)** shows the decrease in intensity of the O_i 1727 cm^{-1} absorption band and the increase in the phonon absorption band as a function of the measured temperature. Both intensities respond directly to a temperature increase: the decrease in the intensity of the O_i 1727 cm^{-1} absorption band due to thermal depopulation of the ground state, the increase in the phonon intensity because the phonon vibrations are thermally excited, hence confirming that the temperature rise is the common origin for both effects. The linear relation between the integrated phonon intensity and the temperature in this temperature window, (see **Figure 5(b)**) allows one to estimate the temperature of a Si-IRE by ATR-IR, using the integrated intensity of the phonon-absorption bands.

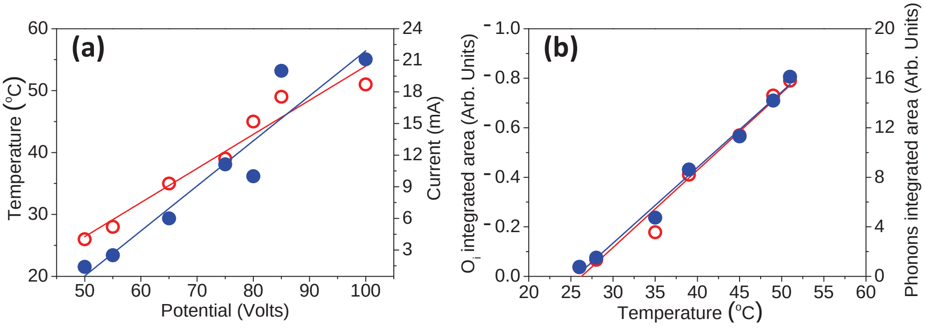

Figure 5. (a) Measured temperature in the microreactor (open red circles, left ordinate) and measured current through the microreactor (closed blue circles, right ordinate) as a function of the applied potential and (b) integrated intensity of the 1727 cm^{-1} O_i absorption peak (open red circles, left ordinate) and the integrated intensity of the phonon absorptions (closed blue circles, right ordinate, integrated from 1500 cm^{-1} to 1200 cm^{-1}) versus the temperature in the microreactor.

Since the electrical resistivity of the microreactor due to the presence of the 2 μm gap is much larger than the resistivity of the home-made IRE, the rise in temperature is larger in the microreactor when the same current is flown through for the same time interval, which is reflected in the higher intensities in **Figures 2(b)** and **3(a)** compared to **Figures 2(d)** and **3(b)**.

With this study we have shown the possibility to study the O_i defects in Si wafers by ATR-IR, using the O_i 1727 cm^{-1} absorption band, while the low wavenumber cut-off in Si prevents one from using the O_i 1108 cm^{-1} absorption band. Since the presence of oxygen impurities is one of the efficiency-limiting factors in the production of solar-cells (the loss in efficiency related to these defects in Cz-Si is about 4% (absolute)[33]) we believe that this method, which enables the *in situ* study of the solar cell performance, can be of added value in Si based device characterization. Furthermore, when applying this device to study the effects of external E-field on catalytic reactions and relevant adsorbed species, the IR signal originated from the Si based microreactor (i.e. phonons band and O_i band) is needed to be carefully separated from the targeted information on adsorbed species and produced species. In addition, the effect of temperature on peaks attributed to phonons can be used to obtain information on temperature in the microreactor.

5.4. Conclusions

We have studied oxygen interstitial defects (O_i) in Si as function of an externally applied potential by means of ATR-IR. We provided evidence that the 1727 cm^{-1} IR absorption band is related to the presence of O_i. With increasing potential we observed a decrease of this 1727 cm^{-1} IR absorption band, accompanied by an increase in the phonon absorption bands. The simultaneous decrease of the O_i 1727 cm^{-1} absorption band and increase of the phonon absorption bands conflicts the assignment of this band as a combination of the asymmetric mode and a phonon combination. Both effects are attributed to an increase in temperature by resistive heating of Si during our experiments. Our experimental procedure enables the *in situ* study of Si based devices like Si solar cells.

5.5. References

(1) Möller, H. J.; Long, L.; Werner, M.; Yang, D.; *Phys. Stat. Sol.* (a), **171**, (1999) 175

(2) Glunz, S. W.; Rein, S.; Warta, W.; Knobloch, J.; Wettling, W.; *Sol. Energy Mater. Sol. Cells*, **65**, (2001) 219

(3) Wang, Q.; Daggubati, M.; Paravi, H.; Yu, R.; Zhang, X. F.; *J. Vac. Sci. Technol.* A, **24**, (2006) 1238

(4) Borghesi, A.; Pivac, B.; Sassella, A.; Stella, A.; *J. Appl. Phys.*, **77**, (1995) 4169

(5) Cheng, C-L; Lu, C-Y; Chang-Liao, K-S; Huang, C-H; Wang, S-H; Wang, T-K; IEEE *Transactions on electron devices*, **53**, (2006) 63

(6) Newman, R. C.; *Rep. Prog. Phys.*, **45**, (1982) 1163

(7) Kaiser, W.; Keck, P.H.; Lange, C.F.; *Phys. Rev.*, **101**, (1956) 1264

(8) Medernach, J. W.; *Handbook of Vibrational Spectroscopy* edited by J. M. Chalmers and P. Griffiths; John Wiley & Sons, Hoboken, New Jersey, USA, (2006)

(9) Pajot, B.; Stein, H. J.; Cales, B.; Naud, C.; *J. Electrochem. Soc.*, **132**, (1985) 3034

(10) Hrostowski, H.D.; Kaiser, R.H.; *Phys. Rev.*, **107**, (1957) 966

(11) Hallberg, T.; Murin, L.I.; Lindström, J.L.; Markevich, V.P.; *J. Appl. Phys.*, **84**, (1998) 2466

(12) Yamada-Kaneta, H.; Kaneta, C.; Ogava, T.; *Phys. Rev.* B, **42**, (1990) 9650.

(13) Artacho, E.; Lizon-Nordström, A.; Yndurain, F.; *Phys. Rev.* B, **51**, (1995) 7862

(14) Artacho, E.; Yndurain, F.; Pajot, B.; Ramirez, R.; Herrero, C.P.; Khirunenko, L.I.; Itoh, K.M.; Haller, E.E.; *Phys. Rev.* B, **56**, (1997) 3820

(15) Pajot, B.; Artacho, E.; Ammerlaan, C. A. J.; Spaeth, J.-M.; *J. Phys. Condens. Matter*, **7**, (1995) 7077

(16) Susarrey-Arce, A.; Tiggelaar, R.M.; Karabudak, E.; Sanders, R.G.P.; Geerdink, B.; Schlautmann, S.; Lefferts, L.; van Houselt, A.; Gardeniers, J. G. E.; A new ATR-IR microreactor to study electrical field driven processes (*submitted*) 2013

(17) Susarrey-Arce, A.; Marín, Á. G.; Schlautmann, S.; Lefferts, L.; Gardeniers, J. G. E., van Houselt, A.; *J. Micromech. Microeng.*, **23**, (2013) 025004

(18) Susarrey-Arce, A.; Marín, Á. G.; Nair, H.; Lefferts, L.; Gardeniers, J. G. E.; Lohse, D.; van Houselt, A.; *Soft Matter* , **8**, (2012) 9765

(19) Karabudak, E.; Yuce, E.; Schlautmann, S.; Hansen, O.; Mul, G.; Gardeniers, Han (J. G. E.); *Phys. Chem. Chem. Phys.*, **14**, (2012) 10882

(20) Russell, J. P.; *Appl. Phys. Lett.*, **6**, (1965) 223

(21) Uchinokura, K.; Sekine, T.; Matsuura, E.; *Solid State Comm.*, **11**, (1972) 47

(22) Temple, P. A.; Hathaway, C. E.; *Phys. Rev.* B, **7**, (1973) 3685

(23) Khajehpour, J.; Daoud, W. A.; Williams, T.; Bourgeois, L.; *J. Phys. Chem.* C, **115**, (2011) 22131

(24) Yoshikawa, M.; Nagai, N.; *Handbook of Vibrational Spectroscopy* edited by J. M. Chalmers and P. Griffiths; John Wiley & Sons, Hoboken, New Jersey, USA, (2006)

(25) Marquez, F.; Morant, C.; López, V.; Zamora, F.; Campo, T.; Elizalde, E.; *Nanoscale Res. Lett.*, **6**, (2011) 495

(26) Nazarewicz, W.; Balkanski, M.; Morhange, J. F.; Sebenne, C.; *Solid State Comm.*, **9**, (1971) 1719

(27) Uchinokura, K.; Sekine, T.; Matsuura, E.; *J. Phys. Chem. Solids*, **35**, (1974) 171

(28) Wei, W.; *Vacuum*, **81**, (2007) 857

(29) Uchino, T.; Kitagawa, Y.; Yoko, T.; *Phys. Rev. B.*, 61, (2000) 234

(30) Tropf, W. J.; Thomas, M. E.; Harris, T. J.; *Handbook of Optics, Devices and Measurements & Properties* edited by M. Bass; McGraw-Hill, New York, USA, (1995)

(31) Gillespie, D. T.; Olsen, A. L.; Nichols, L. W.; *Appl. Opt.*, **4**, (1965) 1488

(32) Jacoboni, C.; Canali, C.; Ottaviani, G.; Alberigi Quaranta, A.; *Solid-State Electron.*, **20**, (1977) 77

(33) Haunschild, J.; Reis, I. E.; Geilker, J.; Rein, S.; *Phys. Status Solidi (RRL)*, **5**, (2011) 199

6

Electric field-induced molecular polarization of *n*-hexane in an ATR-IR microreactor

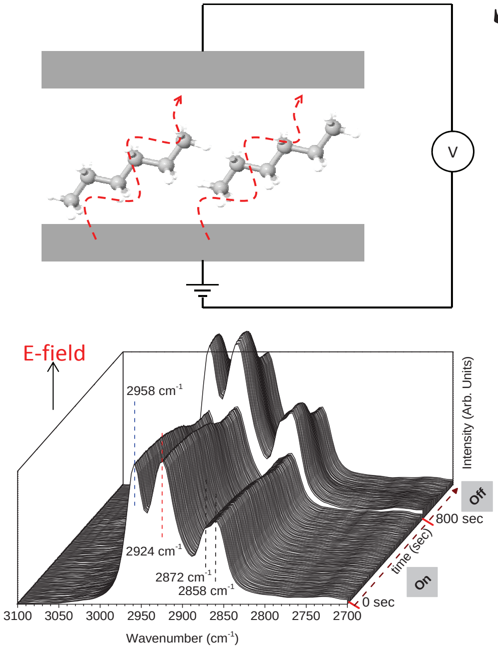

Solvated electrons play an important role in many processes of relevance to physics, chemistry and biology, and in specific synthetic processes in pharmaceuticals as reducing agents in organic synthesis. Among other insulating organic liquids, an interesting example is *n*-hexane. In this work with the help of a home-made fabricated microreactor coupled to ATR-IR, the changes due to electron injection as a function of the applied E-field in *n*-hexane will be discussed. We relate these conformational changes (i.e. changes in the –CH_3 and –CH_2- IR bands) to local changes in the (de)polarization of the *n*-hexane molecules.

In preparation for publication as

A. Susarrey-Arce et al., *Electric field-induced molecular polarization of n-hexane in an ATR-IR microreactor* (**2014**)

6.1. Solvated electrons in *n*-hexane

The aliphatic compound *n*-hexane is known as a non-polar molecule[1] due to its low dipole moment of ca. 0.07 D,[2] produced by the different molecular conformers,[3, 4] see **Figure 1**. Electrical conductivity in a dielectric liquid like hexane is expected to be very low, and any conduction observed is usually attributed to trace amounts of ionic impurities. On the other hand, it has been shown that in liquids of olefinic compounds, like hexene, conductivities are substantially higher,[5] which is thought to be due to electron hopping, attributed to the polarizability of π electrons and the formation of stable negative ion radicals from the molecules that contain the π bonds.[6]

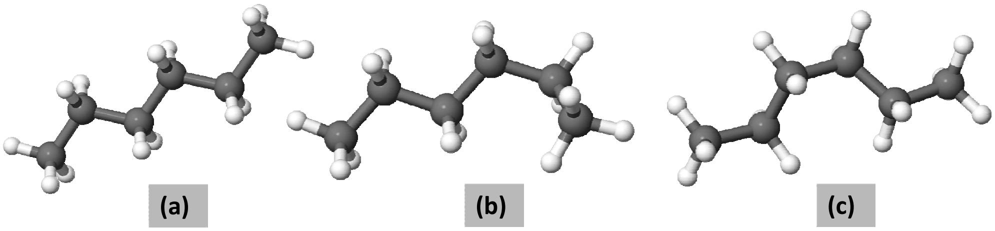

Figure 1. Examples of the different possible conformers of *n*-hexane with different gauche (G) or trans (T) torsion angles: (a) TTT conformer, (b) TTG conformer and (c) TGT conformer; while the TTT conformer has no dipole moment, the TTG and TGT conformer exhibit a small net dipole moment. The formation energies of the TTG and TGT conformer relative to the TTT conformer are in the order of 0.5 kcal/mol. The geometry and numbers are taken from ref.[3].

Gray et al.[7] discuss the mobility of negative charge carriers, i.e. X-ray generated photoelectrons ejected from an electrode into liquid hexane. These authors mention that at low electric fields the charge carriers move as a relatively large clusters, because they exist in a polarized cloud of neighboring molecules. The negative charge carriers in these early studies may have been solvated electrons, the existence of which in hexane, after pulse radiolysis, field injection or photo ionization, has since been reported several times.[8, 9, 10]

The notion that a solvated electron is surrounded by a cluster of polarized solvent molecules may give an opportunity to observe them in situ by InfraRed (IR) spectroscopy. Only a few IR studies are known for solvated electron clusters in water, where the lifetime is extremely short.[11, 12]

In this work we will investigate whether information about solvated electrons in *n*-hexane and 1-hexene can be obtained by means of a home-made microreactor, in which an electric field can be applied over a liquid, and in which IR spectroscopy can be performed via an integrated element for ATR (Attenuated Total Reflectance) IR. Conformational changes in *n*-hexane due to electron transport will be discussed as a function of the applied E-field and time. We will relate the conformational changes to polarization and depolarization of *n*-hexane.

6.2. Experimental section

We study carrier injection into the dielectric liquids *n*-hexane and 1-hexene by applying an external potential to a homemade microreactor of *p*-type silicon containing a 900 nm high flow channel with 15 μm high micropillars which, due to the high curvature at the cylindrical tip edge, enhance the E-field locally. The microreactor is sketched in **Figure 2(a)** and **2(b)** with the E-field oriented upwards (**Figure 2(a)**) or downwards (**Figure 2(b)**). The bottom electrode is shaped as an internal reflection element, enabling in situ attenuated total internal reflection infrared (ATR-IR) spectroscopy. The fabrication of micropillars and ATR-IR microreactor,[13, 14, 15, 16, 17] as well as an extensive investigation of artifacts in the IR spectra that are not caused by chemical effects,[15, 17] have been published previously. A Keithley 2410 power supply programmed via a Labview script was used to control the E-field and record the current-voltage

(I-V) response. Reference ATR-IR measurements under E-field control were performed with He flow (0.05 ml/min) through the microreactor.

The ATR measurements were carried out in a Fourier Transform Infrared (FT-IR) spectrometer, Tensor 27 (Bruker Optics) with a MCT D316/6-L detector. The ATR microreactor was placed in an ATR cell which consists of four concave polished mirrors mounted on a metal holder. The ATR-microreactor channel was filled with *n*-hexane (> 99.00% purity over molecular sieve from Sigma-Aldrich) or 1-hexene (> 99.00% purity from Sigma-Aldrich; purified in-house over molecular sieve). After filling the channel, IR spectra with and without E-field were recorded with a resolution of 8 cm^{-1} and 32 scans, according to our previously reported protocol in **chapter 4**. To estimate the temperature of the ATR-microreactor, the infrared absorption intensity of thermally excited phonons were compared with the calibration curves reported in **chapter 5**.

6.3. Results and discussion

6.3.1. Electron transport in *n*-hexane and 1-hexene

I(V) curves are recorded after the ATR-microreactor was filled with (1) He, (2) *n*-hexane and (3) 1-hexene. The results are shown as current density (J) vs. E-field plots in **Figure 2(c)** and **2(d)**, and as Fowler-Nordheim graphs (ln (J/E2) vs. E-1)[18] in **Figure 2(e)** and **2(f)**. **Figure 2(c)** and **2(e)** are recorded with the E-field pointed upwards (configuration shown in **Figure 2(a)**), while **Figure 2(d)** and **2(f)** are recorded with the E-field directed downwards (configuration shown in **Figure 2(b)**). The two E-field directions upwards and downwards would correspond to electron emission from the pillars and from the flat ATR crystal surface, respectively. In all experiments in this study, care was taken that the E-field conditions remained below the breakdown field of *n*-hexane, which was reported to be 1.3 x 10^6 V/cm.[19]

Insets in **Figure 2(c)** and **2(d)** magnify the low field region from 0 V/cm to -2.5 x 10^4 V/cm (0V to -2.5 V). The current density in **Figure 2(c)** and **Figure 2(d)** was calculated using only the total area of the flat micropillar top surfaces (~ 0.4 cm^2), i.e. the surface area where the electrode gap is 900 nm.

The results in the low field regime (insets in **Figure 2(c)** and **2(d)**) can be listed as a function of the measured current density as follows: J(1-hexene) > J(*n*-hexane) > J(He). The observed higher conduction for 1-hexene is expected based on the presence of the π bond. In *n*-hexane also electron conduction is measured, similar to what was reported earlier.[20, 21, 22] Helium gas, which is used as a benchmark, shows the lowest conduction in the low field regime, but whereas also at the highest field J(1-hexene) > J(*n*-hexane), it is observed that J(He) increases faster with field, and at a negative E-field at absolute values above 3.5 x 10^5 V/cm, it is seen that J(He) > J(1-hexene)> J(*n*-hexane). This increasing slope in J(He) can be described with the Fowler-Nordheim mechanism, as was discussed in our previous report.[17]

In the Fowler-Nordheim (FN) plots in **Figures 2(e)** and **2(f)** it is observed that, with the exception of an off-set difference (1-hexene curves are always above the ones for *n*-hexane), the curves for the two organic liquids are very similar. The fact that, in the case where the E-field is pointed downwards (see **Figure 2(b)**), the slope for 1-hexene is slightly higher at the higher 1/E values (that is, at low E-fields), may be attributed to a lower electrical resistance of 1-hexene[23, 24, 25]. The observation that the FN plots for the downward E-field case show a more distinct Fowler-Nordheim behavior (that is, a clear transition from the low to the high E-field slopes) can be attributed to the expected higher field needed to start electron emission from a flat surface compared to a surface with pillars (the upward E-field case); for the flat surface electron emission is more a stochastic process, starting on randomly positioned sites like asperities on the surface of the ATR crystal, while the relatively sharp edges of the pillar tips[14, 15, 17] lead to local field enhancement and therewith to a lower on-field for field electron emission.

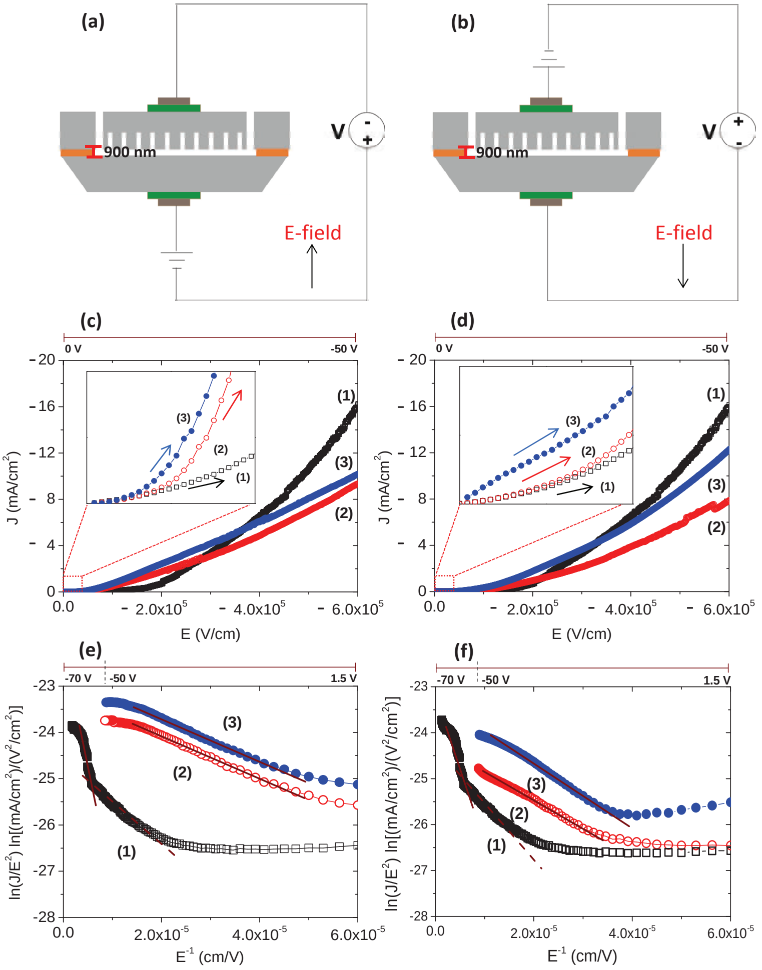

Figure 2. (a-b) Cross sectional representation of the ATR-microreactor. In (c-d) J versus E plots and in (e-f) Fowler-Nordheim plots are shown. In the insets in (c-d), J versus E zoom-in plots at lower potentials are given. In all plots, (1) corresponds to He (black open squares), (2) to *n*-hexane (open red dots) and (3) to 1-hexene (closed blue dots). These data were recorded by increasing the voltage difference between the two elements from 0 V to -50 V, with a sweeping rate of 0.1 V/sec. In the FN plots we have plotted the absolute values of E^{-1}.

6.3.2. Effect of E-field on IR spectra

The IR data in **Figure 3** were obtained with an n-hexane filled ATR-microreactor in which the E-field was oriented upwards (see **Figure 2(a)**), where in **Figure 3(a)** and **3(c)** the voltage difference between the pillars and the ATR crystal was increased linearly with time from 0 to a maximum value of -50 Volts over 800 seconds (labeled **"On"** in **Fig. 3(a)** & **(c)**), and in **Figure 3(b)** and **3(d)** this voltage difference was decreased linearly with time from -50 Volts to 0, also over 800 seconds (labeled **"On"** in **Fig. 3(b)** & **(d)**). In both cases the voltage source was switched off after 800 seconds (labeled **"Off"** in the **figures**). The spectra are plotted in a multiple-curve fashion from 3100 cm^{-1} to 2700 cm^{-1} as a function of the time (y-axis) and the relative IR intensity (z-axis).

In **Figure 3(a)** and **3(c)** in the **"On"** state a decrease in the IR relative intensity can be observed, followed by a substantial increment directly after the E-field was switching off. In the **"On"** state, i.e. for a decreasing voltage, in **Figure 3(b)** and **3(d)**, first a steady increase in IR intensity is seen, followed by a decrease after ca. 380 sec. The IR absorption peaks located at 2958 cm^{-1}, 2924 cm^{-1}, 2872 cm^{-1} and 2858 cm^{-1} are assigned to methyl (-CH$_3$) asymmetric (assym.) stretch, methylene (-CH$_2$-) asym. stretch, methyl symmetric (sym.) stretch and methylene sym. stretch,[26] respectively. No evident changes in the peak shapes or positions of the assigned IR bands were found during the measurements.

The question arises what the origin could be of the intensity increase of the -CH$_3$ and -CH$_2$- IR absorption peaks in **Figure 3(a)**-**3(b)**? A likely answer would be the Kerr electro-optical effect, which implies that a material becomes birefringent in a gradually varied electric field, leading to different light refractive indices parallel or perpendicularly (to the E-field) polarized light. The effect can be substantial for polar liquids, but is also known for dielectric liquids,[27] in which it has been used to determine the E-field distribution from polarized light images.[28] For the infrared range of the optical spectrum, this effect can lead to several scenarios, e.g. changes in the shape of IR absorption peaks[29] or in changes in the relative intensity of IR absorption bands.[30]

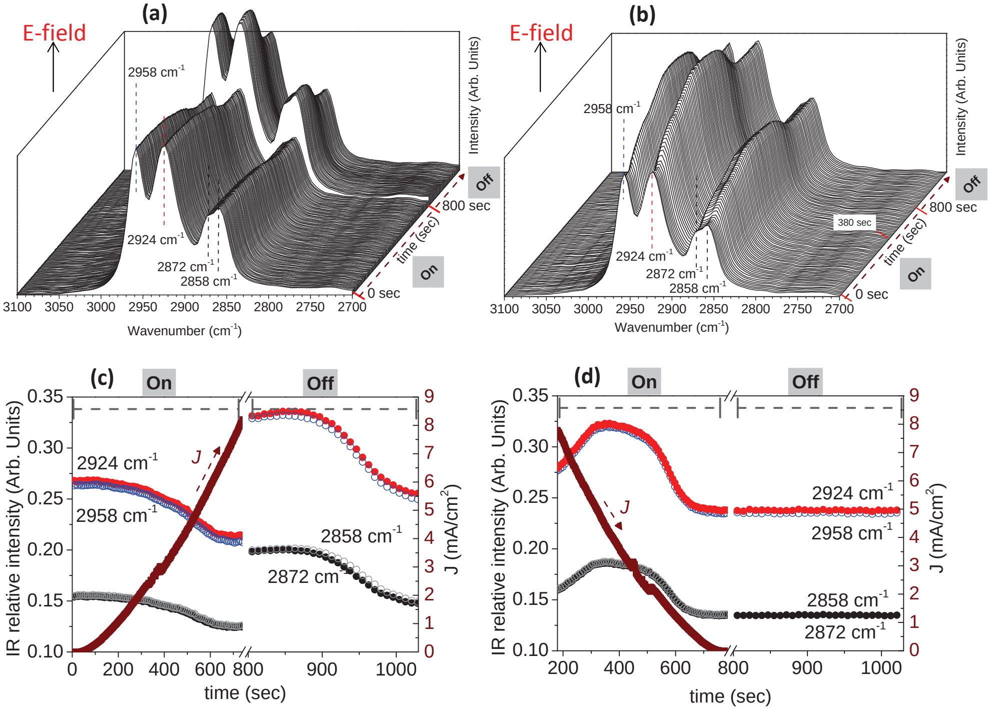

Figure 3. (a-b) ATR-IR absorption of n-hexane from 3100 cm^{-1} to 2700 cm^{-1} and (c-d) line profiles (at the vertical dashed lines in a-b) as a function of time for 2958 cm-1 (blue open dots), 2924 cm^{-1} (red closed dots), 2872 cm^{-1} (black closed dots) and 2858 cm^{-1} (gray open dots) bands during the application of an E-field that linearly varies with time during the first 800 seconds (increasing in (a) & (c), and decreasing in (b) & (d), see text), and is switched to 0 from 800 seconds onwards. In (c-d) the measured current density J is also plotted at the right-hand ordinate.

Based on the agreement of the observed behavior in **Figure 3(b)** and **3(d)** with the latter literature reports, we hypothesize that these data indeed correspond to a Kerr electro-optical effect, which suggests that a polarization of *n*-hexane molecules, and a subsequent field-related orientation of those molecules, must have occurred in the E-field. We also would like to stress here that the measurement principle of ATR is such that IR absorption occurs via the evanescent field of the beam propagating through the ATR crystal, and the penetration depth of that evanescent field is very sensitive to the refractive index of the medium in contact with the crystal. Therefore, changes in the intensity of the absorption lines are consistent with a Kerr electro-optical effect. The temporal trend in the absorption and its dependence of the E-field at this point cannot be explained.

Next, experiments were performed with a downward E-field, in which the potential difference between the electrodes was varied from 0 to -50 Volts, see **Figure 4**. The spectra in **Figure 4(a)** were obtained with a resolution of 8 cm^{-1} averaged over 128 scans. No changes in IR peak shape or position are observed, only a small decay in the relative intensity is seen in **Figure 4(b)** after *ca.* 500 sec and ~800 sec). When the voltage is switched off, an increase of the 2924 cm^{-1} to 2872 cm^{-1} bands, as was observed in **Figure 3(c)**, is not see in **Figure 4(a)-4(b)**, here the ATR-IR intensity slowly relaxes back to the same level as at the start of the experiment. The latter behavior can be interpreted as an effect of the slightly enhanced temperature due to resistive heating when a current is driven across the microreactor, as described earlier in [15]. Alternatively, the observed changes in the IR bands may indicate a molecular relaxation mechanism from molecules oriented with the electric field to their randomly oriented original state. The observed time scale of the relaxation process of 3 - 4 min by far does not agree with such a process, which typically would be picoseconds.[31]

Experiments similar to ones reported for *n*-hexane in **Figure 4**, were performed for liquid cyclohexane. The results revealed identical behavior as for *n*-hexane (*see Supporting Information*).

The clue in understanding the exact behavior of *n*-hexane in an electric field obviously lies in an explanation of the temporal changes in the IR bands. To assess whether there is an electrical circuit effect at the basis of the observed trends, additional experiments were carried out to measure the I(V) transient behavior of the system after shutting off the power supply. A steep current drop to zero was found, after the initial drop no current change over time was recorded. Because of the detection limit of 20 μA in combination with the recording frequency of the source measurement unit used in our work, one cannot exclude that discharging still continues, especially in view of the transient currents of the order of 10-12 measured by LeBlanc in his study of electron drift mobility in *n*-hexane,[21] but we consider it very unlikely that currents of that size would have an influence on the IR absorption bands.

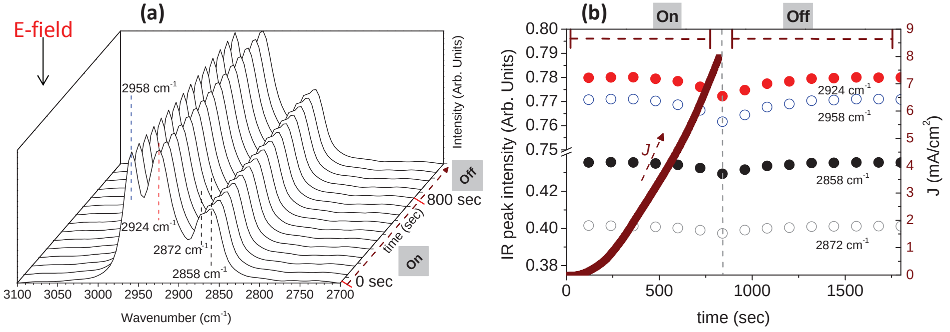

Figure 4. (a) ATR-IR absorption curves plot for n-hexane from 3100 cm^{-1} to 2700 cm^{-1}, and (b) the ATR-IR intensity at the indicated wavenumbers as a function of time and the current density during a linearly growing applied voltage (downward E-field) from 0 to -50 V (at 800 s).

Electrically induced liquid motion (e.g. electroosmotic flow), possibly related to charge injection, could be another effect that has played a role in our experiments. In previous work[32-37] this effect was studied for different electrode shapes, e.g. planar, trapezoidal and needle-like. These experiments and corresponding theoretical models confirm that the electron mobility measurements in these system are obscured by electro convective processes, like jets and vortices, which drive the electrons emitted from the sculpted electrodes towards the flat countercharged surface. So a likely mechanism then would be the one sketched in **Figure 5**: When electron injection (black arrow) takes place, a dense packing of the liquid molecules close to the flat surface is produced, possibly also leading to polarization of the molecules, while upon switching off the potential, relaxation of the polarized molecules occurs. This mechanism resembles the multilayer molecule structures in a non-polar liquid, proposed by Polyansky *et al.*[36]

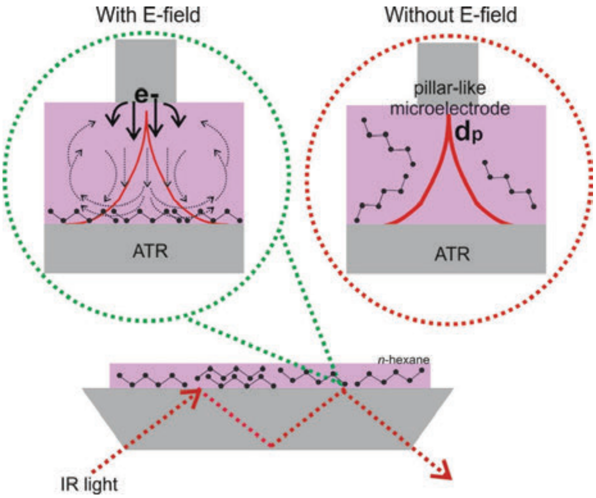

Figure 5. Molecular polarization and relaxation mechanism for *n*-hexane. The moving direction of the electrons is indicated by bold arrows pointing downwards. The motion of the liquid is represented with dashed lines. The calculated d_p for *n*-hexane is about 200 nm to 400 nm (for more details see *Supporting Information*).

6.3.3. Observation of infrared-inactive vibrations

The difference spectra (D_S), defined as the difference between the ATR-IR spectra recorded for *n*-hexane with an applied E-field ($S_{\text{E-field } n\text{-hexane}}$) and without an E-field field ($S_{n\text{-hexane}}$), *i.e.* $D_S = S_{\text{E-field } n\text{-hexane}} - S_{n\text{-hexane}}$, from 3100 cm^{-1} to 2700 cm^{-1} are calculated from the spectra in **Figure 3(a)-3(b)** and presented in **Figure 6(a)** and **6(b)**. Important to mention is that $S_{\text{E-field } n\text{-hexane}}$ and $S_{n\text{-hexane}}$ were normalized to the 2924 cm^{-1} absorption band in **Figure 3** before calculating D_S. The integrated are under the D_S vs. time plots of the peaks indicated in **Figure 6(a)** and **6(b)** are shown in **Figure 6(c)** to **6(f)**. The shape of the spectra in **Figure 6(a)** and **6(b)** resemble the shape of the spectra in **Figure 3**. Also a sudden increase in intensity is observed in **Figure 6(a)** when the E-field is switched off, similar to the behavior in **Figure 3(a)**. The exact peak positions for the D_S in **Figure 6**, are however different from the peak positions observed in **Figure 3**. In **Figure 6** peaks are located at 2967 cm^{-1}, 2942 cm^{-1}, 2906 cm^{-1}, 2873 cm^{-1} and 2860 cm^{-1}. The location of the 2873 cm^{-1} and 2860 cm^{-1} bands was determined by deconvolution of the absorption band present between 2880 cm^{-1} and 2800 cm^{-1}. Line profiles in along the position of the dotted lines in **Figure 6(a)-(b)** are shown in **Figure 6(c)-(f)**. These results are not further discussed in this section. A clear interpretation of the results in **Figure 6(c)-(f)** needs further investigation.

Several of these peaks positions are close to or similar to reported positions in Raman measurements of *n*-hexane in either liquid or solid phase.[38, 39] Cleveland *et al.*[38] reported Raman measurements in liquid phase, with peak positions at 2960 cm^{-1}, 2937 cm^{-1}, 2906 cm^{-1}, 2868 cm^{-1} and 2850 cm^{-1}. Kavitha *et al.*[39] have measured Raman bands at different pressures, in a phase transition study, and found absorption lines, which they attribute to Raman vibrations of the TTT conformer of *n*-hexane, at 2942 cm^{-1} (in-plane asym. methyl ($-CH_3$) stretching), 2906 cm^{-1} (sym. methylene ($-CH_2-$) stretching) and 2873 cm^{-1} (sym. $-CH_2-$ stretching).

We assign the 2942 cm^{-1} and 2906 cm^{-1} absorption bands in **Figure 6(a)** and **6(b)** to the Raman vibration at this positions,[38, 39] while the other bands (i.e. 2967 cm^{-1}, 2873 cm^{-1} and 2860 cm^{-1}) can be attributed to either an IR active band or a combination of both, i.e. Raman active band + IR active band.[40]

Why do we observe Raman active vibrations in an infrared spectrum? The gross selection rule for a Raman active vibration is that its polarizability changes during the vibration. When an external E-field is applied over the vibrating molecule, a dipole is induced, which may vary during the vibration. The latter condition is the gross selection rule for an infrared-active vibration, so these vibration are now also visible in an infrared-spectrum. These E-field induced "IR active Raman vibrations" were predicted by Condon and Woodward[41, 42] and studied in, among others, N_2 by Courtois and Jouve.[43]

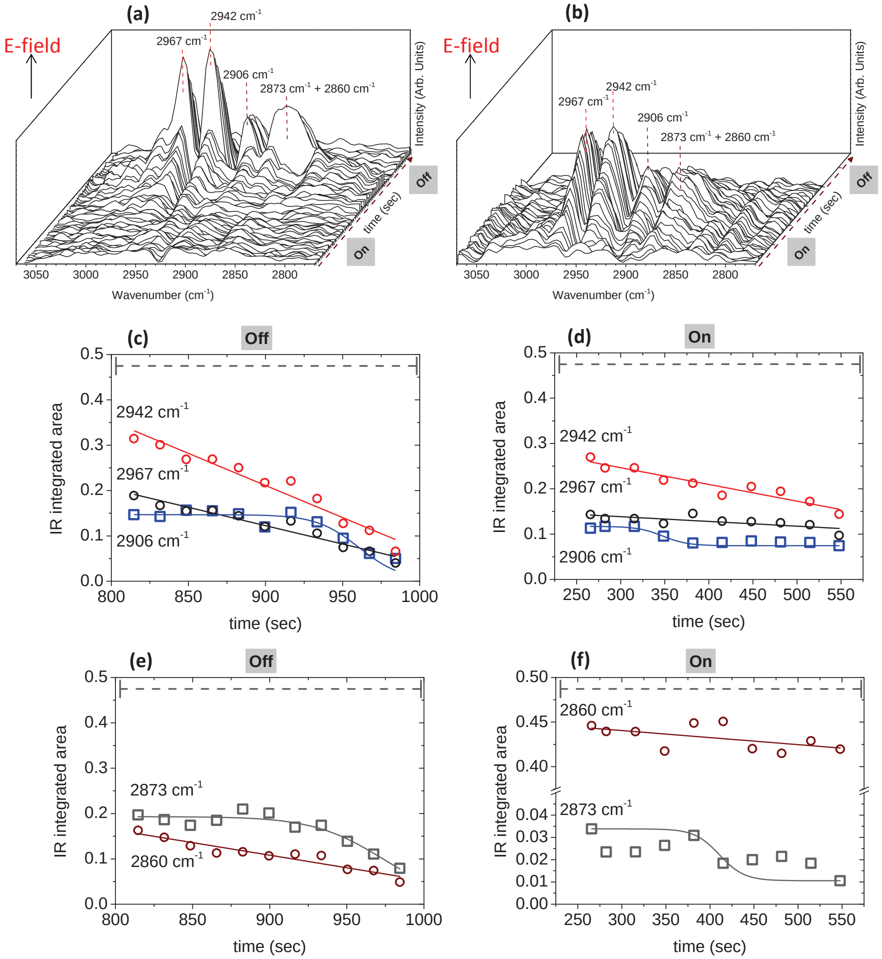

Figure 6. Difference spectra (D_S) in (a-b) of the sym. and assym. streches for *n*-hexane from 3100 cm^{-1} to 2700 cm^{-1} and IR integrated area of the assigned peaks at 2942 cm^{-1}, 2967 cm^{-1}, 2905 cm^{-1}, 2873 cm^{-1} and 2860 cm^{-1} as a function of time are presented in (c and e) for the increasing E-field (increasing J), and in (d and f) for the decreasing E-field (decreasing J).

It is importance to notice that difference spectra derived from the experiments with a downward directed E-field (see **Figure SI-3** *in supporting information*), show adsorption bands at similar position, but with a much lower intensity.

An alternative interpretation for the changes in **Figure 6** could be the CH_3 and CH_2 vibration are excited by the electron motion as proposed by Lewis.[37] In that interpretation it is, however, unclear why the initial intensities in the difference spectra in **Figure 6(b)** are low, while the current density (see **Figure 3(d)**) is monotonically decreasing with time.

6.3.4. Induced -CH_3 bending

The IR spectra of *n*-hexane from 1500 cm^{-1} to 1340 cm^{-1} are shown in **Figure 7**, the E-field was switched on up to 800 sec and switched off after 800 sec (similar to **Figure 2(a)**). In **Figure 7(a)-7(c)** the IR dashed spectra are the last ones recorded before switching off the E-field. The D_S is shown in **Figure 7(b)** and calculated from $D_S = S_{\text{E-field } n\text{-hexane}} - S_{n\text{-hexane}}$. In **Figure 7(c)**, a comparison between a spectrum with (dashed line) and without E-field is given. Moreover, the IR relative intensities of 1460 cm^{-1}, 1435 $cm^{-1}$and 1378 cm^{-1} adsorption bands as a function of time are shown in **Figure 7(d)**. The IR band located at 1460 cm^{-1} can be assigned to either methyl C-H asym. bending or methylene C-H bending vibration, whereas 1378 cm^{-1} is assigned to methyl C-H bending vibration. The 1435 cm^{-1} peak should not be confused with a methyl C-H asym. bending.[26] This peak is, in accordance with earlier work,[15, 17] assigned to increasing phonon adsorption as a consequence of direct heating during application of an E-field over the microreactor. In **Figure 7(b)** a negative peaks at 1466 cm^{-1} and 1447 cm^{-1} are revealed, which can also be assigned to either methyl C-H asym. bending or methylene C-H bending vibration.[26] These negative peaks could also be explained by an slightly increasing temperature due to resistive heating of the Si, leading to a depopulation of the ground state of the vibration and hence to a lower intensity.[15] Comparing the intensity of the phonon adsorption line with the calibration curve in Ref. [15], we estimate a temperature increase of the microreactor of 1-2ºC.

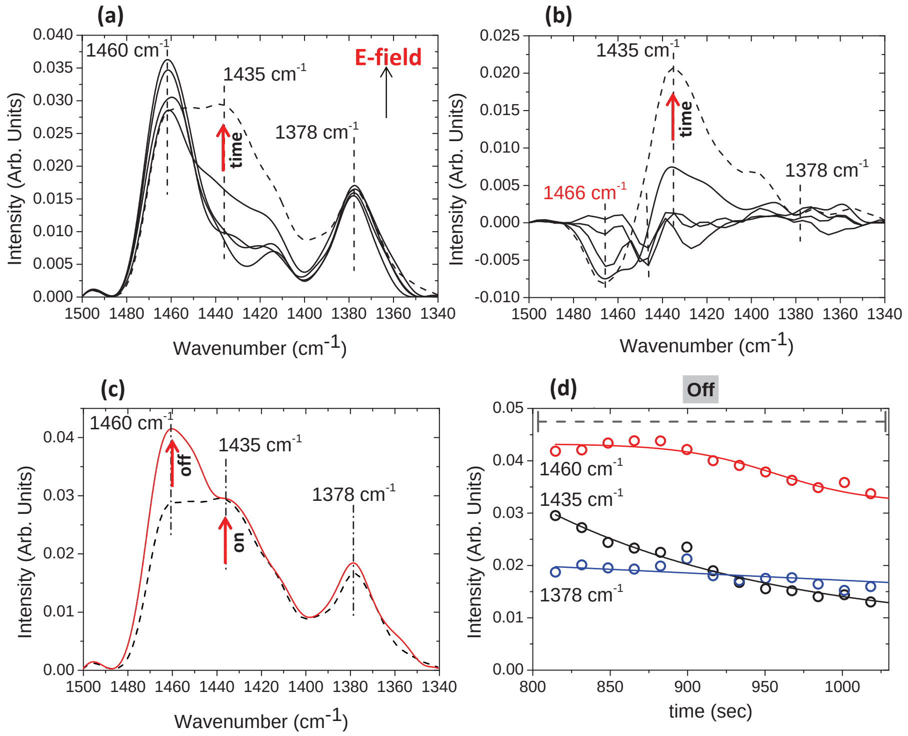

Figure 7. (a) IR spectra of n-hexane from 1500 cm^{-1} to 1340 cm^{-1} as a function of the time (time intervals of ~ 250 sec). (b) difference spectra, and (c) in a comparison with "**On**"/ "**Off**" experiments. (d) profile plot of the 1460 cm^{-1}, 1435 cm^{-1} and 1378 cm^{-1} as a function of time.

6.4. Conclusions and recommendations

For the first time electron transport through *n*-hexane is performed and studied in an ATR-IR microreactor. Based on our results we propose an electron injection mechanism. The enhanced IR relative intensity of the *n*-hexane bands upon/during electron conduction leads to two scenarios: Firstly, electro-optical Kerr effects during applying the E-field (i.e. polarization) and secondly, a relaxation mechanism of the packed molecular layer (i.e. depolarization) after switching off the E-field. Thermal effects indeed occur, but are not significant and clearly do not affect our ATR data.

6.5. References

(1) Leontyev, V.; Tachiya, M.; *J. Chem. Phys.*, **123**, (2005) 224502

(2) Patel, S. A.; Brooks III, C. L.; *J. Chem. Phys.*, **124**, (2006) 204706

(3) Gruzman, D.; Karton, A.; Martin, J. M. L.; *J. Phys. Chem. A*, **113**, (2009) 11974

(4) Smith, G. D.; Jaffe, R. L.; *J. Phys. Chem.*, **100**, (1996) 18718

(5) Forster, E.O.; *J. Chem. Phys.*, **40**, (1964) 91

(6) Forster, E.O.; *J. Chem. Phys.*, **37**, (1962) 1021

(7) Gray, E.; Lewis, T. J.; *Brit. J. Appl. Phys.(J. Phys. D)*, **2**, (1969) 100

(8) Baxendale, J. H.; *Can. J. Chem.*, **55**, (1977) 1996

(9) Taylor, R. J.; *J. Phys. D. Appl. Phys.*, **5**, (1972) 1855

(10) Knoesel, E.; Bonn, Shan, M. J.; Wang, F.; Heinz, T. F.; *J. Chem. Phys.*, **121**, (2004) 404

(11) Ayotte, P.; Johnson, M. A.; *J. Chem. Phys.*, **106**, (1997) 811

(12) Asmis, K. R.; Santambrogio, G.; Zhou, J.; Garand, E.; Headrick, J.; Goebbert, D.; Johnson, M. A.; Neumark, D.M.; *J. Chem. Phys.*, **126**, (2007) 191105

(13) Susarrey-Arce, A.; Marín, Á. G.; Nair, H.; Lefferts, L.; Gardeniers, J. G. E.; Lohse, D.; van Houselt, A.; *Soft Matter*, **8**, (2012) 9770

(14) Susarrey-Arce, A.; Marín, Á. G.; Schlautmann, S.; Lefferts, L.; Gardeniers, J. G. E.; van Houselt, A.; *J. Micromech. Microeng.*, **23**, (2013) 025004

(15) Susarrey-Arce, A.; Tiggelaar, R. M.; Sanders, R. G. P.; Geerdink, B.; Lefferts, L.; Gardeniers, J.G.E.; van Houselt, A.; *J. Phys Chem C*, **117**, (2013) 21936

(16) Tran, T.; Staat, H. J. J.; Susarrey-Arce, A.; Foertsch, T. C.; van Houselt, A.; Gardeniers, J. G. E.; Prosperetti, A.; Lohse, D.; Sun, C.; *Soft Matter*, **9**, (2013) 3272

(17) Susarrey-Arce, A.; Tiggelaar, R. M.; Karabudak, E.; Sanders, R. G. P.; Geerdink, B.; Schlautmann, S.; Lefferts, L.; van Houselt, A.; Gardeniers, J. G. E.; *Sens. Act. B*, (2014)(submitted)

(18) Ravindra, N. M.; Zhao, J.; *Smart Mater. Struct.*, **1**, (1992) 197

(19) Crowe, R. W.; Bragg, J. K.; Sharbaugh, A. H.; *J. Appl. Phys.*, **25**, (1954) 392

(20) Davis, H. T.; *J. Phys. Chem.*, **54**, (1971) 3112

(21) LeBlanc, O. H.; *J. Chem. Phys.*, **30**, (1959) 1443

(22) Minday, R. M.; Schmidt, L. D.; Davis, H. T.; *Phys. Rev. Lett.*, **26**, (1971) 360

(23) Agiral, A.; Eral, H. B.; van den Ende, D.; Gardeniers, J. G. E.; IEEE *Transactions on electron devices*, **58**, (2011) 3514

(24) House, H.; *Proc. Phys. Soc. Section B*, **70**, (1956) 913

(25) Arii, K.; Kitani, I.; Kawamura, M.; *J. Phys: Appl. Phys.*, **12**, (1979) 787

(26) Coates, J.; *Interpretation of infrared spectra, a practical approach*, Meyers, R.A.; (Ed.), Encyclopedia of analytical chemistry, *John Wiley & Sons* Ltd, Chichester (2000)

(27) Hill, C. E.; House, H.; *Electronics Letters*, **3**, (1967) 78

(28) Cassidy, E. C.; Cones, H. N.; *J. Res. Nat. Bur. Stand. C. Eng. Instrum.*, **73C**, (1969) 5

(29) Charney, E.; Halford, R. S.; *J. Chem. Phys.*, **29**, (1958) 221

(30) Kovalevskaya, T. I.; *J. Appl. Spectr.*, **65**, (1998) 459

(31) Kayumova, D. B.; Syrnikov, Y. P.; Penkina, N. V.; Rodnikova, M. N.; *Russian J. Phys. Chem.* A, **80**, (2006) 1634

(32) Gray, E.; Lewis, T. J.; *Br. J. Appl. Phys.*, **16**, (1965) 1049

(33) Daaboul, M.; Louste, C.; Romat, H.; *Dielectric Liquids*, 2008. ICDL 2008. *IEEE Int. Conf. Diel. Liq.*, **4** (2008)

(34) Wu, J.; Traore, P.; Louste, C.; Koulova, D.; Romat, H.; *J. Electrostatics*, **71** (2013) 326

(35) Louste, C.; Daaboul, M.; Romat, H.; *J. Electrostatics*, **67**, (2009) 348

(36) Polyansky, V. A.; Pankratieva, I, L.; *J. Colloid Interf. Sci.*, **230**, (2000) 306

(37) Lewis, T. J.; *Appl. Phys. Lett.*, **27**, (1956) 645

(38) Cleveland, F. F.; Porcelli, P.; *J. Chem. Phys.*, **18**, (1950) 1459

(39) Kavitha, G.; Narayana, C.; *J. Phys. Chem. B*, **111**, (2007) 14130

(40) Cotton, F. A.; *Chemical Applications of Group Theory*, 3rd Ed., *John Wiley*, NY: (1990)

(41) Condon, E. U.; *Phys. Rev.*, **41**, (1932) 759

(42) Woodward, L. A.; *Nature*, **165**, (1950) 198

(43) Courtois D., P. Jouve; *J. Mol. Spectroscopy*, **55**, (1975) 18

Supporting Information

1. IR integrated peaks during the upwards E-field experiments

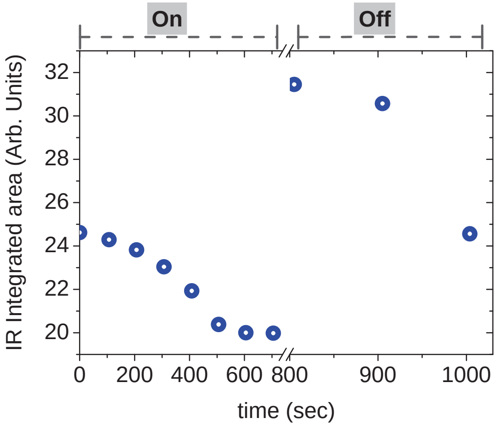

Figure SI-1. The IR integrated peaks from 3030 cm^{-1} to 2750 cm^{-1} as a function of time are shown for the measurements with the E-field oriented upwards.

Thus, similar trends as the reported results in **Figure 3** are found. The results are calculated by integrating the IR -CH_3 and -CH_2- bands from *n*-hexane.

2. Thermalization effects in cyclohexane

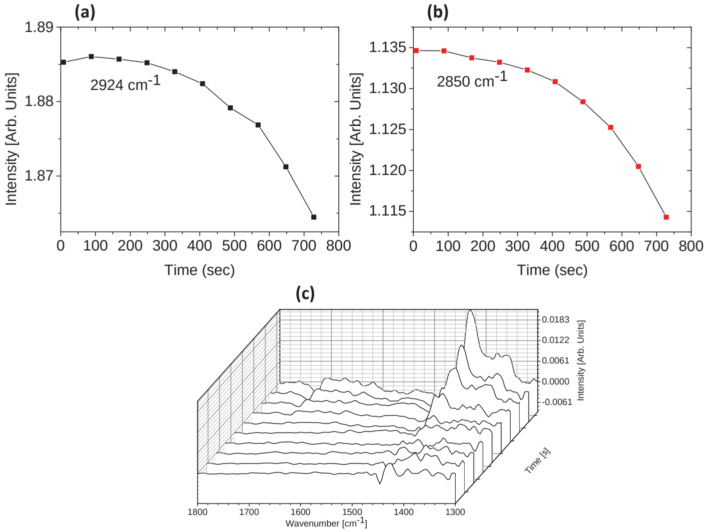

Figure SI-2. (a-b) IR relative intensity as a function of time during applying (a linearly with time increasing, -50 V at 800 s) E-field (in downwards direction) to cyclohexane. A decay in the IR relative intensity is observed for 2924 cm^{-1} and 2850 cm^{-1}, whereas in (c) growth of the phonon absorption band at 1435 cm^{-1} is observed.

3. Difference spectra for *n*-hexane: downwards directed E-field experiments

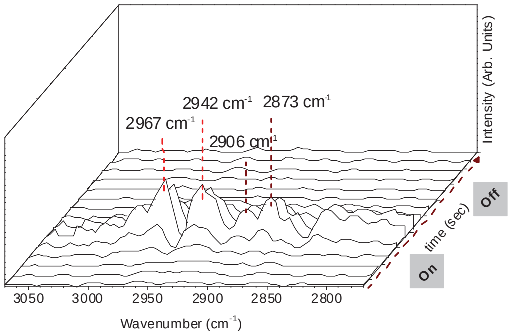

Figure SI-3. Difference spectra of the collected data in **Figure 4(a)**. The spectra substraction is carried out in the same way as for **Figure 6**. Note that the E-field is oriented downwards.

4. Difference spectra for *n*-hexane without E-field (Effect of E-field on IR spectra section)

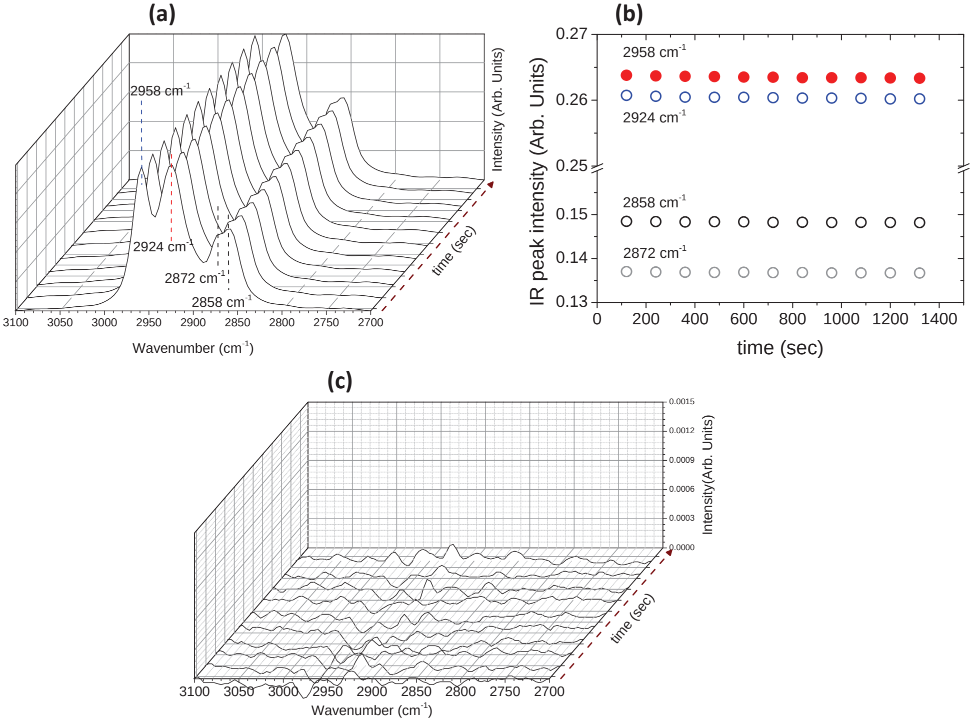

Figure SI-4. (a) IR multi-curve of *n*-hexane from 3100 cm^{-1} to 2700 cm^{-1}. (b) line profiles along the vertical dashed lines indicated in (a) and (c) the difference spectra of the collected results from (a).

No differences were observed for these experiment with respect to experiments in **Figure 3**, **Figure 4** and **Figure 6**.

5. Penetration depth (d_p) for *n*-hexane

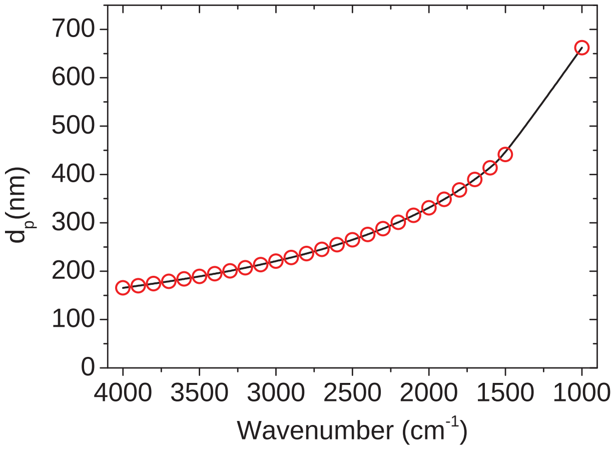

Figure SI-5. Calculated penetration depths (d_p) for *n*-hexane at 25 °C

Table SI-1. Estimation of the critical angle (Θ_c) and penetration depth (d_p) at 25 °C for *n*-hexane. These values have been used to estimate d_p.

Temperature [°C]	***n*-hexane density [g/cm³]**	**Θ_c [°]**	**d_p [nm]**
25	1.372	21.87	~200-400 nm

6. Difference spectra for *n*-hexane (induced -CH_3 bending section): no E-field experiments

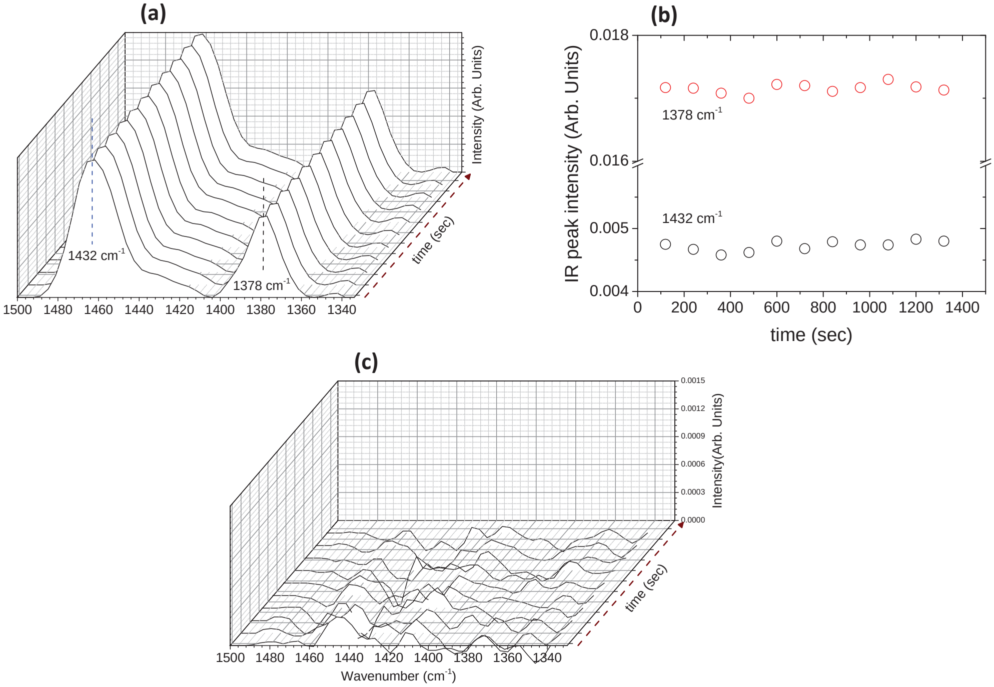

Figure SI-6. (a) IR multi-curve of *n*-hexane from 1500 cm^{-1} to 1340 cm^{-1} (b) line profiles along the vertical dashed lines in (a), and (c) the difference spectra of the collected results from (a).

No differences were observed for these experiment with respect to experiments in **Figure 7**.

7

CO adsorption on Pt nanoparticles in low E-fields studied by ATR-IR spectroscopy

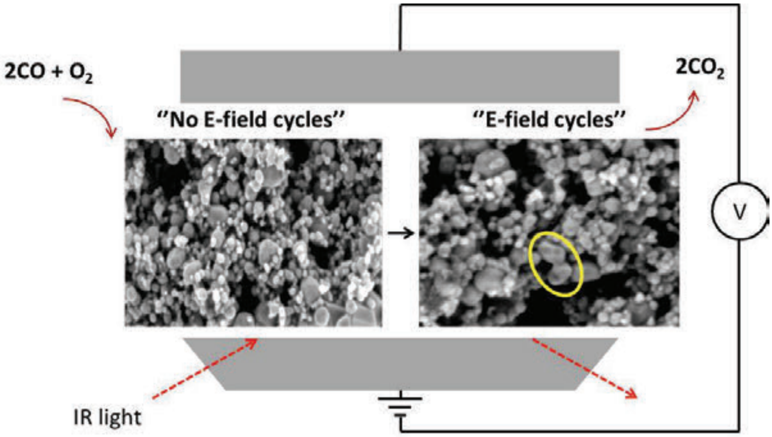

In this chapter we study the adsorption of carbon monoxide on Pt nanoparticles deposited in a microreactor which is designed such that the adsorption reaction can be followed by attenuated total reflection infrared spectroscopy (ATR-IR Spectroscopy), while an external electrical field (E-field) is applied over the reactor. We show that it is possible to deposit Pt nanoparticles on the electrodes of the microreactor and that CO adsorption can be followed by ATR-IR spectroscopy. Linearly, bridged and multiply adsorbed CO was found on the Pt nanoparticles. In a sequence of adsorption experiments the integrated ATR-IR intensity of the adsorption band of the linearly adsorbed CO was found to reach a steady value after an initial decrease. This initial decrease is attributed to a loss of Pt surface area.

In preparation for publication as

A. Susarrey-Arce et al., *CO adsorption on Pt nanoparticles in low E-fields studied by ATR-IR spectroscopy* (**2014**)

7.1. CO adsorption by ATR-IR

CO adsorption on group VIII metal catalysts has been intensively studied over the years, because of its relevance as a probe of the available amount of adsorption sites on surfaces of catalysts as well as it relevance for the catalytic converter for pollution control.[1, 2] In the catalytic oxidation of CO the charge on the surface plays an important role.[3] Because of the vast amount of available literature on CO adsorption and the importance of the charge/surface potential for the adsorption of CO, the adsorption (and oxidation, see **chapter 8**) is used as a test reaction for our newly developed microreactor, in which we are able to vary an external E-field (E-field) over the reactor and monitor the catalyst surface by infrared spectroscopy. The aim in this chapter is to investigate the effects of low E-fields on CO-adsorption by in situ Attenuated Total Internal Reflection Infrared spectroscopy (ATR-IR).

7.2. Experimental section

7.2.1. Fabrication of the ATR-IR microreactors

The main device used in this study is a microreactor designed for simultaneous application of an external (E-field) and in situ ATR-IR. A schematic representation of the microreactor is shown in **Figure 1(a)**. Details of the fabrication and choices of the materials for this microreactor have been described elsewhere (**Chapter 4**).[4-8] In brief, the E-field is applied via Cu/$TiSi_2$ contacts (grey/brown bars in **Figure 1(a)**) to the top and bottom electrode. The bottom electrode, fabricated from a double side polished *p*-type (0.5 mm thickness, 5-10 Ω-cm resistivity, Okmetic Finland), acts as total internal reflection element for the ATR-IR measurements. The top electrode, fabricated from a double side polished *p*+-type silicon (500 μm thickness, 0.01-0.02 Ω-cm resistivity, Okmetic Finland), is micro machined with the cylindrical pillars. The interspace between the top of the micropillars and the ATR-IRE surface is

~ 2 μm. The width and length of the channel are 1.8 and 4.4 cm, respectively, leading to a total volume V of ~1.3 x 10-2 cm^3. The SiO_2 layer terminating the ATR-IRE crystal (colored in orange) is defined by dipping the ATR-IRE processed wafer in 1% HF for about 25 min post to lithography (and prior to thermal bonding), during which the initial ~ 2 μm SiO_2 layer is locally thinned down to 140 nm ± 40 nm.

7.2.2. Coating of the gas flow channel with Pt nanoparticles

Commercially available Pt nanopowder from Sigma-Aldrich (with particle size < 50 nm) was suspended as received in *n*-hexane (> 99.00% purity over molecular sieve from Sigma-Aldrich). The Pt nanoparticle suspension was prepared by adding 50 mg of the nanopowder to 1 mL of *n*-hexane (which would be enough to cover the entire bottom electrode with a ~ 50 nm thick layer of Pt particles when all the particles would be deposited), followed by vigorous ultra-sonication for 3 h. The microreactor was coated three times subsequently by flowing the 50 g/L Pt nanoparticles in *n*-hexane suspension through the microreactor flow channel and dried overnight under 10% O_2/He mixture (99.999% purity from Praxair) with a flow of ~30 μL/min.

7.2.3. Electrical characterization of the Pt coated microreactors

Subsequent to the coating with Pt nanoparticles (see section 1.2) the electrical response of the microreactors upon application of an electrical field over the micoreactors was investiged. A Keithley 2410 power supply programmed via a home-written Labview script was used to apply the voltage pulses and to record the electrical response in the form of I(V) curves.

7.2.4. Pre-treatment of the microreactors

A room temperature pre-treatment to remove any trace of n-hexane from the deposition process and to reach a stable IR signal is performed prior to ATR-IR microreactor experiments, consisting of four cycles of CO chemisorption and subsequent CO oxidation with total flows of 30 μL/min of CO (99.97% purity) and premixed 10% O_2/He mixture (99.999% purity), respectively (all gases from Praxair). During this pretreatment, no E-field is applied to the microreactor.

7.2.5. CO adsorption/oxidation cycles

In a typical experiment CO (99.97% purity, Praxair) was flowed (30 μL/min) for 210 minutes followed by a premixed 10% v/v O_2/He (99.999% purity, Praxair) mixture (30 μL/min) for 360 min to remove the adsorbed CO, preparing the surface of the Pt nanoparticles for the next CO adsorption experiment. This experiment (CO adsorption and subsequent oxidation), hereafter termed as "adsorption cycle", was performed during applying of ± 2.5 V, ± 15 V and ± 25 V over the microreactor, keeping the top electrode connected to earth as indicated in **Figure 1(a)**. In between every two adsorption cycles in which an E-field was applied, an adsorption cycle without E-field was performed as reference.

With a flow rate of 30 μL/min the residence time for CO in the microreactor is in the order of half a minute, while the stoichiometric amount needed to fully cover the available Pt surface is reached within a few seconds.

7.2.6. ATR-IR measurements

During each experiment in situ ATR measurements were carried out in a Fourier Transform Infrared (FT-IR) spectrometer, Tensor 27 (Bruker Optics) with a MCT D316/6-L detector with a resolution of 8 cm^{-1} and 256 scans. The microreactors were positioned in a home-designed ATR cell, which consists of four concave polished mirrors mounted on a metal holder with electrical connectors. ATR spectra are measured against a background in premixed 10% O_2/He mixture, and are shown baseline corrected.

Finally, after the experiments in which an E-field was applied, an ATR-IR spectra were measured using polarized light in a reference experiment (CO was absorbed without applying an E-field) with a resolution of 8 cm^{-1} and 1024 scans by placing a rotatable MIR polarizer (KRS-5) from Bruker Optics in the IR beam between the IR source and the ATR cell. This measurement was repeated using a newly coated (but similarly pretreated) microreactor for comparison.

7.3. Results

7.3.1. Coating the gas flow channel of the ATR-IR microreactor with Pt particles

A representative Scanning Electron Microscope (SEM) image of the deposited Pt nanoparticles after fracturing a freshly coated ATR-IR microreactor into small pieces with a diamond dresser is shown in **Figure 1(b)**. The inset shows an image of the deposited Pt nanoparticles at higher magnification. **Figure 1(c)** shows a SEM image after coating a diced Si substrate with the Pt nanoparticles, following the procedure described in 1.2, with in the inset an image at higher magnification. **Figure 1(d)** shows a SEM image of the deposited Pt nanoparticles after fracturing the microreactor which was used for the experiments described in 1.5. Energy dispersive X-rays spectroscopy reveals a Pt coverage of ~ 0.14 μg/mm^2 (assuming a penetration depth of ~ 5 μm for the e-beam).

All the images in **Figure 1(b)-(d)** show Pt particles on the bottom-electrodes (confirmed by the SEM image of the backscattered electrons, EDX spectroscopy, and X-ray photo-electron spectroscopy (XPS), not shown) on the surfaces with a bimodal distribution, big particles with diameters of 100 to 150 nm are present, as well as small particles with diameters around 10 nanometers. The very small Pt particles (diameter < 10 nm), which are observed frequently in **Figure 1(b)-(c)** are less frequently observed in **Figure 1(d)**. In addition, in **Figure 1(d)** coalesced Pt particles can be observed. For the top electrodes similar results are observed (not shown).

7.3.2. Electrical characterization of the microreactors

I(V) curves are recorded for the Pt nanoparticles coated and non-coated microreactor, while flowing a premixed 10% O_2/He mixture through the microreactor. The results are plotted as current density (J) *vs.* E-field plots in **Figure 1(e)** and **1(f)**, and as Fowler-Nordheim graphs ($\ln(J/E^2)$ *vs.* $1/E$)[9] in **Figure 1(g)** and **1(h)**. **Figure 1(e)** and **1(g)** are measured with the E-field directed downwards (from the top electrode with the pillars to the bottom ATR-IRE electrode), while **Figure 1(f)** and **(h)** are measured with the E-field directed upwards, corresponding to electron emission from the pillars and the flat ATR crystal, respectively. The current density in **Figure 1(f)** was calculated using only the total area of the flat micropillar top surfaces (~ 0.4 cm^2), which is the surface are where the gap between top and bottom electrode is 2 μm.[5]

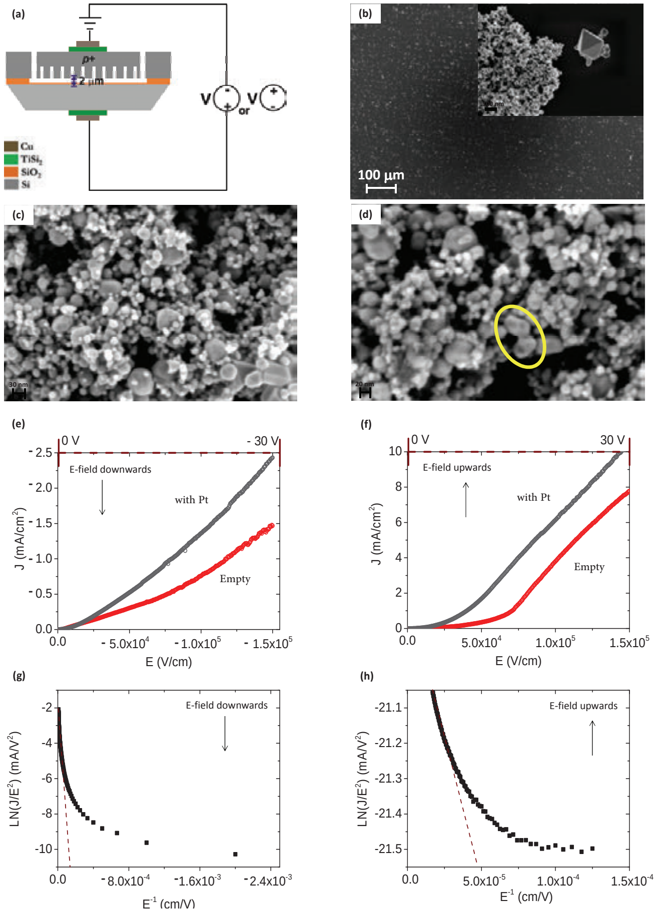

Figure 1. (a) Schematic representation of the microreactor used in this study. On the top electrode of *p*+-type Si 15 μm high micropillars are micromachined (note that the microdevies are not drawn to scale). On the bottom electrode, which acts as an ATR-internal reflection element, 140 nm SiO_2 (orange) is grown. (b)-(d) SEM images of (b) the bottom electrode of a fractured freshly coated microreactor (the inset shows a higher magnification); (c) a coated Si wafer, and (d) a bottom electrode of coated microreactor after having been subjected to CO adsorption studies. In (d) an example of coalesced particles is outlined by the ellipse. (e)-(f) Current densities versus applied E-field curves for Pt nanoparticles coated and non-coated ("empty") microreactors recorded while a 10% O_2 in He mixture was flown through the microreactor. In (e) the E-field is directed downwards (from the top to the bottom electrode), while in (f) the E-field is directed upwards. (g)-(h) Fowler-Nordheim plots extracted from the curves for the Pt nanoparticles coated microreactors in (e) and (f). The dotted lines are linear fits.

7.3.3. CO adsorption ATR-IR measurements

Figure 2 displays some ATR-IR spectra measured during CO chemisorption experiments in which no E-field was applied over the microreactor. Linearly adsorbed CO (hereafter CO_L) on Pt is initially observed at 2068 cm^{-1}, which shifted to 2050 cm^{-1} with increasing surface coverage. Bridging CO (hereafter CO_B) on Pt is observed with low intensity at 1840 cm^{-1} and a broad band (hereafter COM_B) for multiply adsorbed with comparable intensity is observed from 1730 to 1620 cm^{-1}, with a maximum at 1708 cm^{-1}. The weak maximum at 1656 cm^{-1} is attributed to the presence of water in the spectrometer and is corrected for in the inset of **Figure 3**.

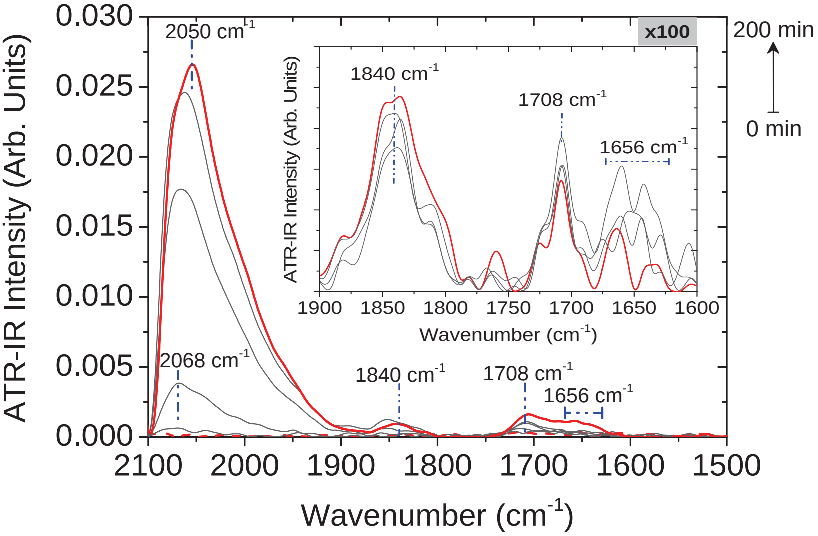

Figure 2. ATR-IR spectra recorded during CO adsorption without an applied E-field. The inset shows a 100x magnification of the signal from 1900 to 1600 cm^{-1} after correction for water absorption, by subtraction of the last spectrum (with the water signal) of a completed adsorption/oxidation cycle.

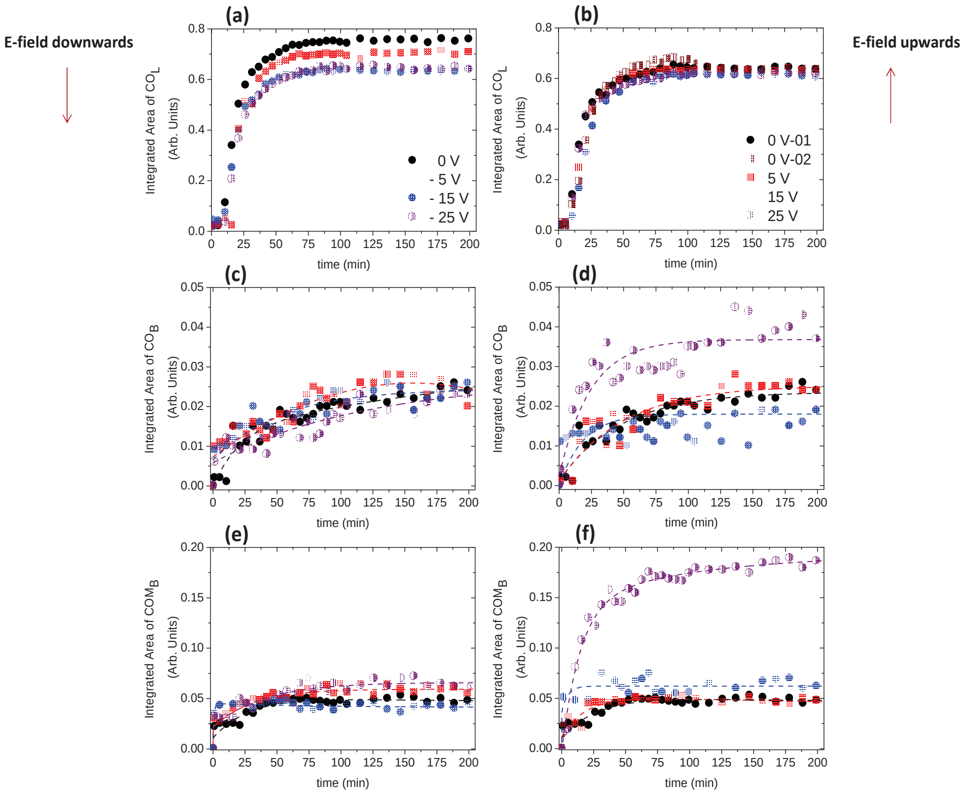

Figure 3. Integrated intensities of the CO$_L$ (a-b), CO$_B$ (c-d) and COM$_B$ (e-f) absorption bands in subsequent adsorption cycles (Sequence: 0 V, -5 V, -15 V, -25 V (in (a), (c) and (e), field downwards), 0 V(1), 0 V(2), 5 V, 15 V, 25 V(in (b), (d) and (f), field upwards)). The legend in (a) is also valid for (c) and (e), the legend in (b) for (d) and (f).

Integrated intensities (after water substraction) of the CO adsorption bands in *subsequent* adsorption cycles are displayed in **Figure 3**. The integration boundaries for the CO$_L$, CO$_B$ and COM$_B$ are 2110 – 1900, 1900 – 1750 and 1750 – 1600 cm^{-1}, respectively. The spectra start at t = 0, the moment that the CO flow through the microreactor is started. **Figure 3(a)**, **(3c)** and **3(e)** show the integrated intensities of the CO$_L$, CO$_B$ and COM$_B$ absorption bands, respectively, in a subsequent set of adsorption cycles for increasing values of an E-field applied in the *downwards* direction, while **Figure 3(b)**, **(3d)** and **3(f)** show the integrated intensities of the CO$_L$,

CO_B and COM_B absorption bands, respectively, in a subsequent set of adsorption cycles for increasing values of an E-field applied in the *upwards* direction. In **Figure 3(a)** and **3(b)** the integrated intensity starts to rapidly increase after a few minutes and levels off to a constant value after ~80 minutes. This constant value is higher in the first two experiments (with applied voltages 0 and – 5 V) in **Figure 3(a)** and has a similar values for the other experiments in **Figure 3(a)** and **3(b)**.

The signal-to-noise ratio in **Figure 3(c)-(f)** is much lower, due to the lower peak intensities of the CO_B and COM_B adsorption bands. In **Figure 3(c)-(f)** the increase in the integrated intensities starts right from $t = 0$ and they seem to level off to a constant value around $t = 100$ min. Note that in the experiment with 25 V applied over the microreactor the trends in the integrate intensity in **Figure 3(d)** and **(f)** is always significantly larger than the others.

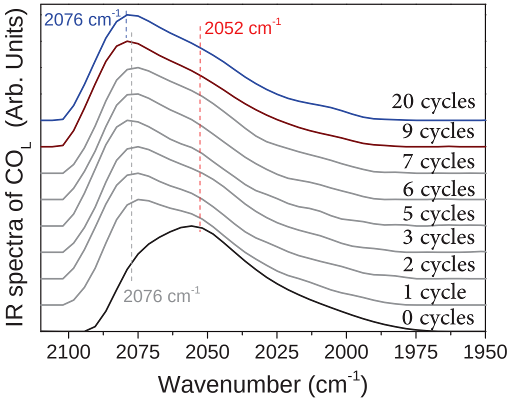

Figure 4. ATR-IR CO adsorption spectra after 200 min. exposure to CO of the reference measurements (i.e. measurement without applied E-field, V = 0) performed within two CO adsorption cycles in which an E-field was applied.

In between every two CO adsorption cycles in which an E-field was applied, and adsorption cycle without an applied E-field was performed as reference. ATR-IR adsorption spectra at *t* = 200 min. of these reference measurements are shown in **Figure 4**. The broad and strongly asymmetric CO_L absorption band has initially a maximum at 2052 cm^{-1} (after 0 cycles, only pretreated), which shifts to ~2076 cm^{-1} after 20 CO adsorption cycles, accompanied by a ~25% decrease of the integrated signal.

The ATR-IR CO_L adsorption spectra measured using polarized light are shown in **Figure 5**, for the microreactor after more than 20 adsorption cycles in **Figure 5(a)** and for a newly prepared, but pretreated (see section 1.4) Pt nanoparticles coated microreactor in **Figure 5(b)**. In both cases is the spectrum obtained with p-polarized light very similar to the reference spectrum measured with non-polarized light (middle and top curves in **Figure 5**)**.** The spectrum obtained with s-polarized light, which is enlarged for comparison, is clearly different with a much smaller and more symmetric peak at 2091 and 2076 cm^{-1} in **Figure 5a** and **5b**, respectively.

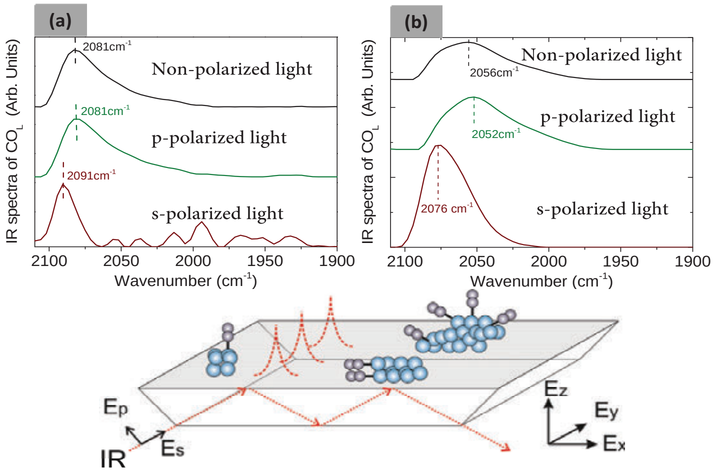

Figure 5. ATR-IR CO_L adsorption spectra measured in a microreactor after more than 20 adsorption cycles (a) and in a newly prepared, but pretreated microreactor (b). Note that the scale of the spectrum obtained with s-polarized light is enlarged for comparison.

7.4. Discussions

7.4.1. Coating the gas flow channel of the ATR-IR microreactor with Pt particles

From the SEM image of the ATR-internal reflection element in the fractured microreactor in **Figure 1(b)** it can be observed that the Pt nanoparticles are distributed over the entire surface in a square deposition pattern. This square distribution pattern is attributed to the presence of the pillars at a distance of only 2 μm on the opposite top electrode during the drying process, which gives rise to capillary forces during the drying process. We attribute this successful deposition of Pt nanoparticles with hexane as a solvent in the microreactor to its low surface tension, since in trials with water and ethanol the microreactor broke down, while the liquid was flown through, indicating clogging in the microreactor, which might be related to the "omniphobicity" of the top electrode (see **Chapter 1** and **Chapter 2**).[6, 7]

7.4.2. Electrical characterization of the microreactors

The linear behavior at higher E-field values (*i.e.* low 1/E values) in **Figure 1(g)** and **1(h)** is indicative of E-field driven electron emission, giving rise to significant current levels. The onset field strength for field emission can be extracted from the intercept with the 1/E axis in Figure **1(g)** and **1(h)**. A higher field is needed to start emission from the flat surface in Figure **1(h)** compared to emission from the micropillars in **Figure 1(g)**. The relatively sharp edges of the pillar tips[4, 5, 7] locally enhance the E-field, leading therewith to a lower onset E-field value for electron emission from the pillared top electrode. From **Figure 1(g)** and **1(h)** the calculated onset values for electron emission correspond to application of ~ - 1 V and ~ 4 V over the microreactor, respectively.

7.4.3. CO adsorption ATR-IR measurements

The assignments of the CO absorption peaks at 2068-2050 cm^{-1}, 1840 cm^{-1}, 1708 cm^{-1} to linear (CO_L), bridging (CO_B) and other multiply-bonded (COM_B) CO, respectively, is in accordance with literature.[10] The weak 1656 cm^{-1} (for which is corrected in the inset of **Figure 2**) is probably due to presence of water. The exact structural assignment of the adsorption configuration for the 1708 cm^{-1} absorption band remains unclear, but likely candidates are a long 2-fold bridge (which could occur between 2 adjacent ridges of the missing row reconstructed (110) surface) or CO molecules σ-bonded to one Pt atom and σ or π bonded to a second one.[10]

A clear interpretation for the red-shift from 2065 cm^{-1} to 2050 cm^{-1} in **Figure 2** needs further investigation. An increasing dipole-dipole interaction strength would show up as a blue-shift in the spectra, which we would expect. The increasing dipole-dipole interaction is, however, apparently compensated by another effect in our measurements. A higher degree of back-donation to the π* CO orbitals would result in a blue-shift. A possible reason for this higher degree of back donation could be the co-adsorption of water, which is present as impurity in the CO feed. Water adsorbs via the oxygen and is able to donate electrons to the Pt. As a consequence, the back donation from Pt to CO increases, leading to a blue-shift. Indeed is co-adsorbing water reported to cause a blue-shift of ~20 cm^{-1} in the CO_L adsorption peak.[11, 12]

In **Figure 3(a)** we observe a leveling off of the final integrated intensities in the first experiments. After the decrease in the first two adsorption cycles, we do not observe a further decrease of the integrated CO_L absorption intensity in **Figure 3(a)** and **3(b).** We assign this decrease in intensity to a decrease in available adsorption sites during the experiments as a consequence of particle restructuring during CO exposure. The enhanced particle restructuring in ambient CO pressure is observed and documented before.[13, 14] After the first two CO adsorption/oxidation cycles the integrated CO_L absorption intensity does not change further, independent of the presence or absence of an E-field (see **Figure 3(b)**). A initial rapid decrease of surface area, followed by a long period in which the area tends to approach a limiting value is characteristic for coarsening controlled by particle migration and coalescence.[15] Indeed, clearly coalesced particles are observed after 20 CO adsorption/oxidation cycles in **Figure 1c**. Due to the lower signal-to-noise ratio in **Figure 3(c)-(f)** it is not possible to observe a similar decay in the integrated intensities after the first experiments.

In the reference measurements performed in between two E-field measurements (**Figure 4**) the same trend is observed: the CO_L ATR-IR adsorption spectra show significant changes in the first experiments. The adsorption maximum is blue shifted from 2052 cm^{-1} in the first spectrum to 2076 cm^{-1} in the last spectra. This shift is consistent with an interpretation in terms of ripening, since a blue shift for the CO_L adsorption band for larger Pt particles compared to smaller ones is well documented.[16] In addition also the decrease in integrated intensity in **Figure 4**, is consistent with a ripening mechanism, leading to a lower surface area for CO adsorption.

In the spectra obtained with polarized light (**Figure 5**) the s-polarized light probes purely the vibration parallel to the surface (in the XY plane), while the p-polarize light excites vibrations with a more (but not necessarily exclusively) perpendicular character.[17] It is therefore not surprising that the spectra obtained with the p-polarized light and the non-polarized light in **Figure 5(a)** and **5b** resemble each other closely. The differences in these spectra are included above in the discussion of **Figure 4.** Remarkably the spectrum obtained with s-polarized light differs significantly, showing a significant peak at 2091 cm^{-1} in **Figure 5(a)**, for a microreactor after more than 20 CO adsorption cycles, and a clear peak at 2076 cm^{-1} in **Figure 5(b)**, for a newly coated microreactor. The presence of the 2091 cm^{-1} adsorption peak in **Figure 5(a)** might be consistent with the presence of larger particles (due to the ripening) since this peak has been attributed to the vibration of islands of CO adsorbed on {111} Pt faces,[18] which will be more dominantly present in larger particles.

7.5. Conclusions

In conclusion, we have studied the influence of the presence low strength E-field on CO adsorption on supported Pt particles *in situ* by ATR-IR in a sequence of CO adsorption/oxidation cycles. A decrease of the ATR-IR intensity of the CO_L adsorption band is observed in subsequent CO adsorption/oxidation cycles. This observed decrease in the ATR-IR intensity is caused by a coarsening effect during the experiment and shows no direct influence of direction and magnitude of the applied E-field.

7.6. References

(1) Berlowitz, P. J.; Peden, C. H. F.; Goodman, D. W.; *J. Phys. Chem.*, **92**, (1988) 5213

(2) An, K.; Alayoglu, S.; Musselwhite, N.; Plamthottam, S.; Melaet, G.; Lindeman, A. E.; Somorjai, G. A.; *J. Am. Chem. Soc.*, **135**, (2013) 16689

(3) Mojet, B. L.; Miller, J. T.; Ramaker, D. E.; Koningsberger, D. C.; *J. Catal.*, **186**, (1999) 373

(4) Susarrey-Arce, A.; Tiggelaar, R. M.; Sanders, R. G. P.; Geerdink, B.; Lefferts, L.; Gardeniers, J. G. E.; van Houselt, A.; *J. Phys Chem C*, **117**, (2013) 21936

(5) Susarrey-Arce, A.; Tiggelaar, R. M.; Karabudak, E.; Sanders, R. G. P.; Geerdink, B.; Schlautmann, S.; Lefferts, L.; van Houselt, A.; Gardeniers, J. G. E.; *Sens. and Act. B* (submitted) 2014

(6) Susarrey-Arce, A.; Marín, Á. G.; Nair, H.; Lefferts, L.; Gardeniers, J. G. E.; Lohse, D.; van Houselt, A.; *Soft Matter*, **8**, (2012) 9770

(7) Susarrey-Arce, A.; Marín, Á. G.; Schlautmann, S.; Lefferts, L.; Gardeniers, J. G. E.; van Houselt, A.; *Micromech. Microeng.*, **23**, (2013) 025004

(8) Tran, T.; Staat, H. J. J.; Susarrey-Arce, A.; Foertsch, T. C.; van Houselt, A.; Gardeniers, J. G. E.; Prosperetti, A.; Lohse, D.; Sun, C.; *Soft Matter*, **9**, (2013) 3272

(9) Ravindra, N. M.; Zhao, J.; *Smart Mater. Struct.*, **1**, (1992) 197

(10) De La Cruz, C.; Sheppard, N.; *Spectrochimica Acta A*, **20**, (1994) 271

(11) Rupprechter, G.; Dellwig, T.; Unterhalt, H.; Freund, H.-J.; *J. Phys. Chem B*, **105**, (2001) 3797

(12) Vaarkamp, M.; Mojet, B. L.; Kappers, M. J.; Miller, J. T.; Koningsberger, D. C.; *J. Phys. Chem*, **99**, (1995) 16067

(13) Raskó, J.; *J. Catal.*, **217**, (2003) 478

(14) Berkó, A.; Szökő, J.; Solymosi, F.; *Surf. Sci.*, **337**, (2004) 566

(15) Wynblatt, P.; Gjostein, N. A.; *Prog. Solid State Chem.*, **9**, (1975) 21

(16) Allian, A. D.; Takanabe, K.; Fujdala, K. L.; Hao, X.; Truex, T. J.; Cai, J.; Buda, C.; Neurock, M.; Iglesia, E.; *J. Am. Chem. Soc.*, **133**, (2011) 4498

(17) Ras, R. H. A.; Schoonehdyt, R. A.; Johnston, C. T.; *J. Phys. Chem. A.*, **111**, (2007) 8787

(18) Brandt, R. K.; Hughes, M. R.; Bourget, L. P.; Truszkowska, K.; Greenler, R. G.; *Surf. Sci.*, **286**, (1993) 15

8

CO oxidation on Pt nanoparticles in low E-fields studied by ATR-IR spectroscopy

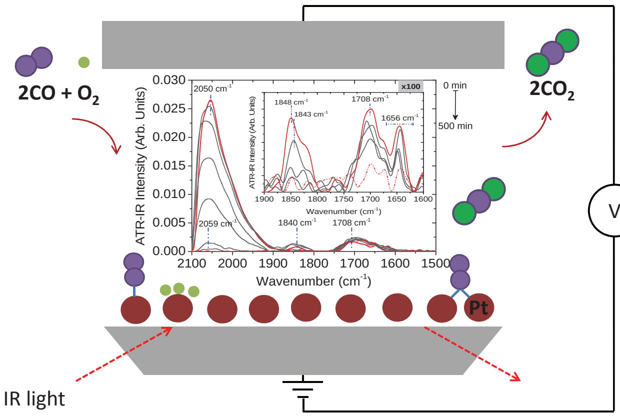

In this chapter we present preliminary data on influence of an external electrical field (E-field) on the oxidation of adsorbed carbon monoxide on Pt nanoparticles deposited in a microreactor which is designed such that the reaction can be followed by attenuated total reflection infrared spectroscopy (ATR-IR Spectroscopy), while an external E-field is applied over the reactor. The intensity of linearly (CO_L), bridged (CO_B) and multiply adsorbed (COM_B) CO on the Pt nanoparticles if followed during the oxidation by ATR-IR spectroscopy. When the surface is fully covered with CO, we observe a poisoning effect of more than 5 hours, during which the surface is exposed to CO, but only gradual changes in the integrated intensities of the adsorbed CO absorption bands are observed. After this long poisoning period a rapid oxidation is observed in which the CO absorption bands disappear completely. Surprisingly we observe no effect of the poisoning time when an E-field is applied during the oxidation, but we do observe an increase of the poisoning time by maximum 2 hours when a (low) E-field is present during the CO adsorption.

In preparation for publication as

A. Susarrey-Arce et al., *CO oxidation on Pt nanoparticles in low E-fields studied by ATR-IR spectroscopy* (**2014**)

8.1. CO oxidation by ATR-IR

CO oxidation on group VIII metal catalysts has been intensively studied over the years, because of its relevance as a model reaction in heterogeneous catalysis as well as it relevance for the catalytic converter for pollution control.[1, 2] In the catalytic oxidation of CO the charge on the surface plays an important role.[3] Because of the vast amount of available literature on CO oxidation and the importance of the charge/surface potential for CO oxidation, the oxidation of CO is used as a test reaction for our newly developed microreactors, in which we are able to vary an external E-field (E-field) over the reactor and monitor the catalyst surface by infrared spectroscopy. The aim in this chapter is to investigate the effects of low E-fields on CO-oxidation by in situ Attenuated Total Internal Reflection Infrared spectroscopy (ATR-IR).

8.2. Experimental section

A schematic representation of the homemade p^+-ATR-IR microreactor is presented in **Figure 1(a)**. The bottom electrode (to which the voltage is applied) is shaped as an internal reflection element, enabling in situ attenuated total internal reflection infrared (ATR-IR) spectroscopy, while the p^+-top electrode with micropillars (15 μm high and 9 μm diameter) is grounded. The ATR-IR microreactor was coated with commercially available Pt nanopowder from Sigma-Aldrich (with particle size < 150 nm). Scanning Electron Microscopy (SEM) of the purchased Pt nanoparticles is presented in **Figure 1(b)**. A detailed description of the coating method is shown in **Chapter 7**. In addition, the fabrication methods of the micropillars and the ATR-IR microreactor are described in **Chapters 2** to **Chapters 4**.

The optical and electrical experiments were carried out by placing the ATR-microreactor in an ATR unit which consist of four concave polished mirrors mounted on a metal holder. A Keithley 2410 power supply programmed via a home-written Labview script was used to apply the voltage pulses and to record the electrical response. A detailed electrical characterization of the microreactor is given in **Chapter 7**.

The IR measurements were recorded using a FTIR spectrometer (Tensor 27, Bruker Optics) with a MCT D316/6-L detector with a resolution of 8 cm^{-1} and 256 scans. ATR spectra are measured against a background in premixed 10% O_2/He mixture (99.99% purity, Praxair), and are shown baseline corrected.

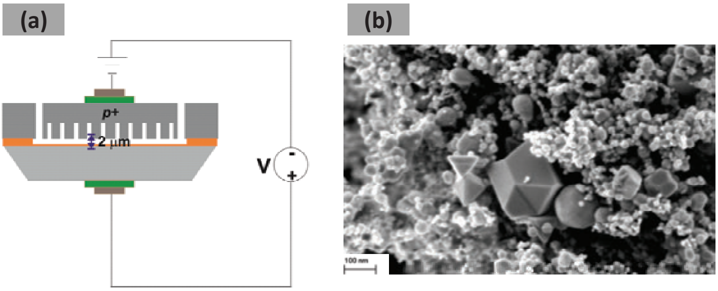

Figure 1. (a) schematic cross section of the fabricated microreactor. In (b) a SEM image of the commercial Pt nanoparticles. The scale bar in the SEM image represents 100 nm.

Prior to ATR-IR microreactor experiments a room temperature pre-treatment to remove any trace of *n*-hexane and to reach a stable IR signal is performed, consisting of four cycles of CO chemisorption and subsequent CO oxidation with total flows of 30 µL/min of CO (99.97% purity) and premixed 10% O_2/He mixture (99.999% purity), respectively (all gases from Praxair).

Three experiments are performed subsequently at room temperature with a total flow of 30 µL/min. Under this circumstances, the stoichiometric amount of O_2 needed to completely oxidize the available adsorbed CO on the Pt surface is reached within a half a minute. The residence time of O_2 in the microreactor is also in the order of half a minute.

A detailed schematic representation of the accomplished steps in the experiments is shown in **Figure 2**. Each experiment is divided in three different subsequent time lapses, which are labeled “CO adsorption”, “CO saturation” and “CO oxidation”, and with durations of 200, 200 and 500 minutes, respectively. CO was flown (30 μL/min) during the “CO adsorption” and “CO saturation” step, followed by a, premixed 10% v/v O_2/He flow (30 μL/min) during the “CO oxidation” step. In between the “CO saturation” and the “CO oxidation” step a premixed 10% v/v O_2/He is flowed (0.5 mL/min) via a bypass for 10 min to exhaust the gas phase CO from the gas lines. The following experiments are performed:

Experiment 1: “CO adsorption” was performed without application of an electrical potential. An electrical potential was applied during “CO saturation” and the subsequent “CO oxidation”.

Experiment 2: “CO adsorption” and “CO saturation” were performed without application of an E-field, followed by the application of the electrical potential during “CO oxidation”.

Experiment 3: “CO adsorption” and “CO oxidation” were performed without application of an E-field, while “CO saturation” was performed with an applied E-field.

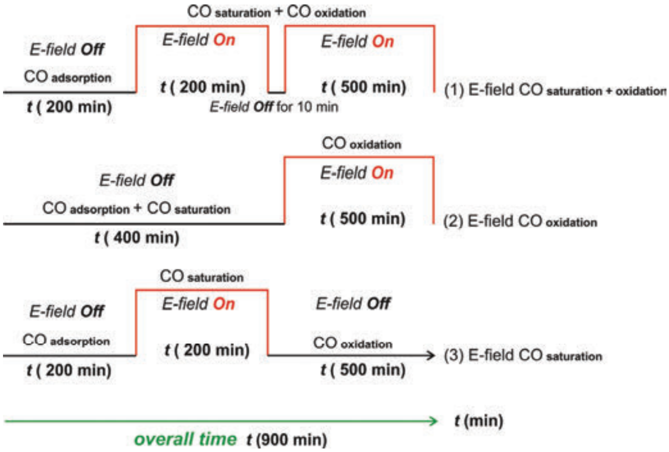

Figure 2. Performed experiments (see text). The red colored lines represent the E-field “On”, while the back lines represent the E-field “off”. (1) E-field CO saturation + E-field CO oxidation; (2) E-field CO oxidation; (3) CO saturation.

8.3. Results

8.3.1. CO oxidation without E-field

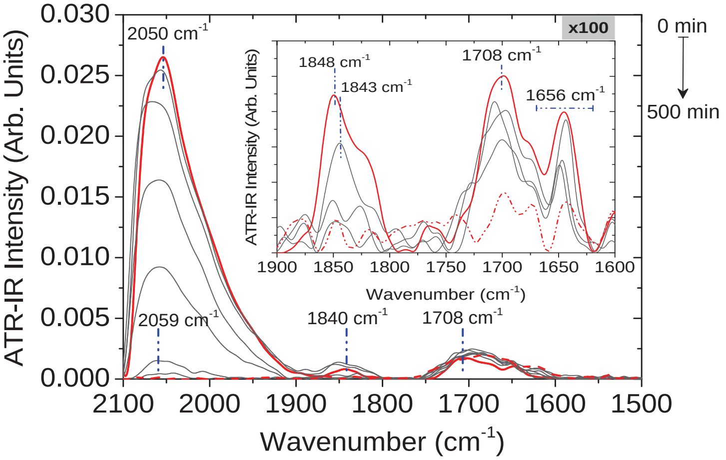

Figure 3. ATR-IR spectra recorded during CO oxidation without an applied E-field. The inset shows a 100x magnification of the signal from 1900 to 1600 cm^{-1} after correction for water absorption, by subtraction of the last spectrum (with the water signal) of a completed adsorption/oxidation cycle.

First we show the results of a reference measurement performed in the absence of an E-field during CO adsorption or oxidation. **Figure 3** displays some ATR-IR spectra measured during CO oxidation experiments in which no E-field was applied over the microreactor. Linearly adsorbed CO (hereafter CO$_L$) on Pt is observed at 2050 cm^{-1}, which shifted to 2059 cm^{-1} with decreasing surface coverage. Bridging CO (hereafter CO$_B$) on Pt is observed with low intensity at 1848 cm^{-1} and a broad band (hereafter COM$_B$) for multiply adsorbed with comparable intensity is observed from 1730 to 1620 cm^{-1}, with a maximum at 1708 cm^{-1}. The weak intensity around 1656 cm^{-1} is attributed to presence of water (as impurity in the feed) and is corrected for in the inset of **Figure 3**.

8.3.2. E-field CO saturation + E-field CO oxidation (experiment 1)

The IR integrated peak areas of CO_L, CO_B and COM_B (see **chapter 7** for the assignments of this bands) as a function of time during the oxidation period in experiment 1 are presented in **Figure 4**. The integration boundaries for the CO_L, CO_B and COM_B are 2110 – 1900, 1900 – 1750 and 1750 – 1600 cm^{-1}, respectively. The spectra start at $t = 0$, the moment that the CO flow through the microreactor is started. In **Figure 4(a)**, **4(c)** and **4(e)** the CO oxidation measurements are given for negative potentials, i.e. 0 V, -2.5 V, -5 V, -10 V and -15 V, whereas for **Figure 4(b)**, **4(d)** and **(f)** the oxidation measurements were performed at positive potentials, i.e. 0 V, 2.5 V, 5 V, 10 V and 15 V. Several differences can be observed between **Figure 4(a)** and **4(b)**. The integrated peak area for CO_L remains steady until 100 min, where a small increases is observed up to 150 min. The integrated peak areas for CO_L start to decrease after ~ 150 min, which continues up to 350 min - 480 min (depending on the applied E-field magnitude and direction), at which point an abrupt decrease to zero occurs that indicates rapid oxidation of the adsorbed CO species.

An increase in the oxidation time is found for both negative and positive potentials. It is observed in **Figure 4(a)** that the time increases (see dashed lines indicating the abrupt decrease in integrated intensity) up to 415 min below -10 V and 465 min for -15 V. Positive E-fields in **Figure 4(b)** have shown an increase up to ~ 460 min for electrical potentials higher than 2.5 V. The signals of CO_B and COM_B in **Figure 4(c-f)** have a much lower signal-to-noise ratio due to the much lower intensities of the CO_B and COM_B adsorption bands. The results reveals comparable oxidation times for CO_B and COM_B as for the CO_L adsorption band in **Figure 4(a-b)**.

To further investigate the effects of the E-field as a function of time, we estimate the delay of initiation of rapid oxidation (i.e. abrupt decrease to zero in **Figure 4**) caused by the applied potential with respect to the results found in the absence of E-field. In **Figure 5**, the time differences ($\Delta t = t_{\text{E-field}}\text{-}t_{\text{no E-field}}$) for CO_L, CO_B and COM_B from **Figure 4** as a function of the applied potential are presented. The Δt-potential graph reveals that for the experiments at positive potentials, the delay in oxidation time increases fast to a value of ~110 min at – 5 V, followed by leveling off around that value, while at negative potentials a the delay in oxidation time increases gradually t_o ~100 min for – 15 V.

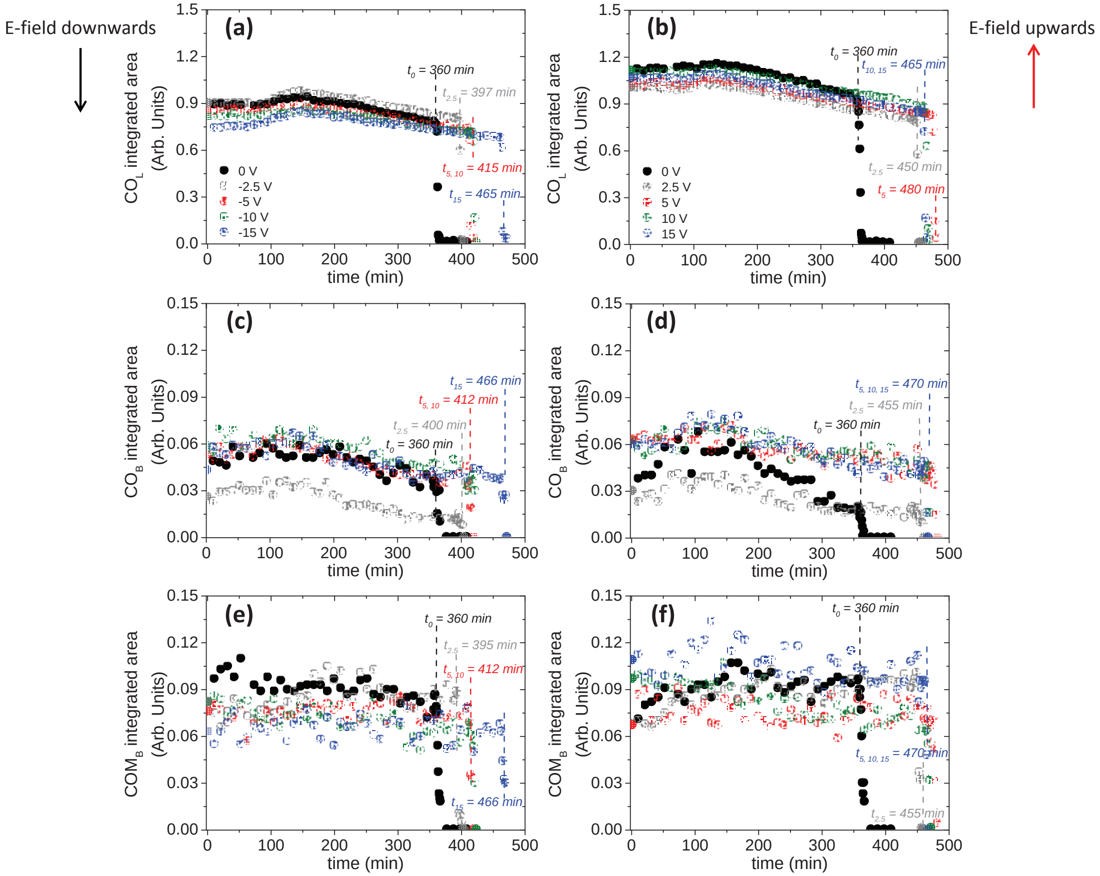

Figure 4. CO_L, CO_B and COM_B IR integrated area from 2110 cm^{-1} to 1900 cm^{-1}, 1900 $cm^{-1}$to 1750 cm^{-1} and 1750 cm^{-1} to 1640 cm^{-1} as a function of time in experiment 1.

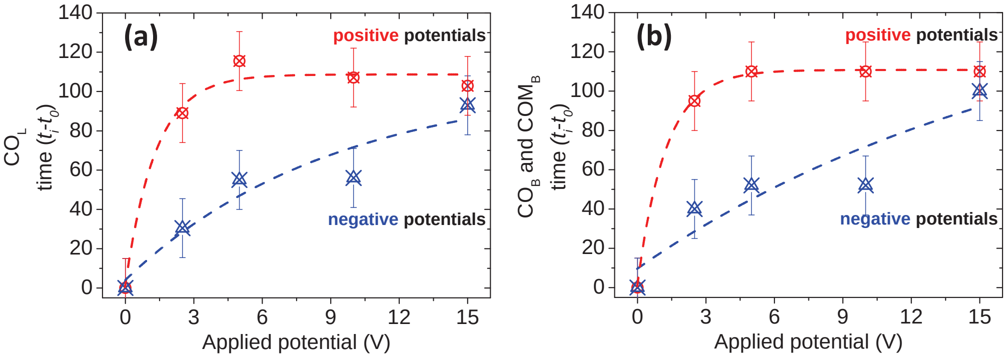

Figure 5. CO_L, CO_B and COM_B time differences ($\Delta t = t_{E\text{-field}}$-$t_{no\ E\text{-field}}$) as a function of the applied potential in experiment 1. Δt is calculated based on the results in **Figure 4**.

8.3.3. E-field oxidation (Experiment (2))

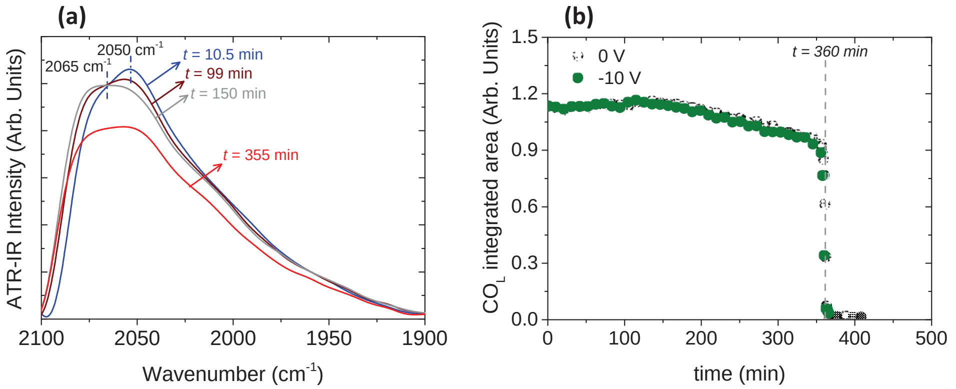

Figure 6. (a) IR spectra of the CO_L band for CO oxidation (without E-field, V = 0) experiment from 2100 cm^{-1} to 1900 cm^{-1} as a function of time. In (b) the CO_L integrated area (from 2110 cm^{-1} to 1900 cm^{-1}) as a function of time for 0 V experiments (as shown in (a)) and -10 V are presented.

The IR spectra and IR integrated peak areas of CO_L as a function of time are presented in **Figure 6**. In **Figure 6(a)**, a blue shift is found from t = 10.5 min to 99 min with the broadening of the CO_L band, followed by small decrease in intensity at t = 150 min and further decreasing at *t* = 355 min is observed. **In Figure 6(b)** the integrated intensity of the CO_L adsorption band is shown for application of 0 V and -10 V (experiment 2). Similar trends are observed as in **Figure 5** with a sharp decay at *t* = 360 min for 0 V and -10 V experiments, but interestingly, no delay in the initiation of oxidation of CO is observed.

8.3.4. E-field saturation (experiment (3))

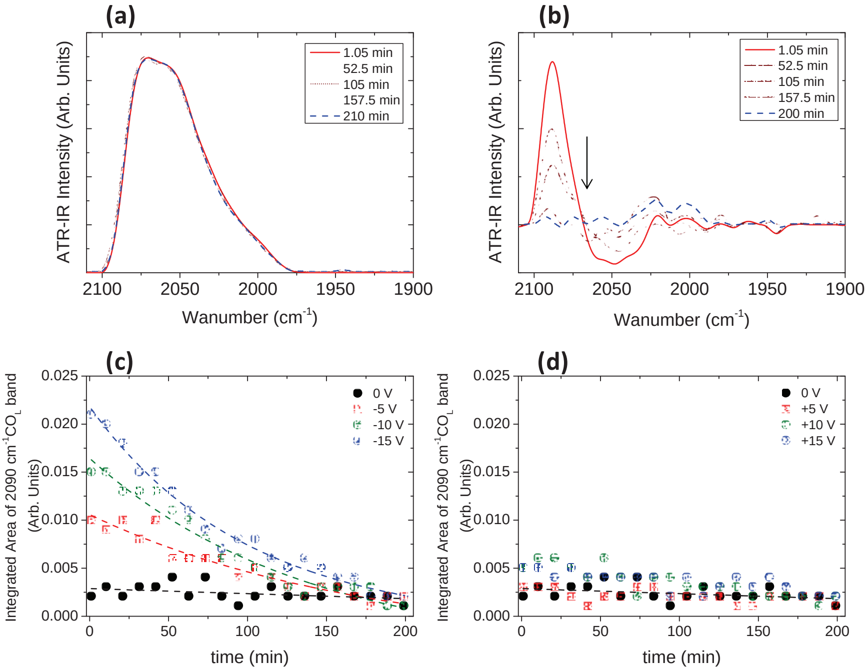

Figure 7. (a) CO_L IR spectra for different times during E-field saturation (-15 V), measured as a function of time over 210 minutes (experiment (3)). (b) Time difference spectra, Ds = $t_i - t_{210}$ min for different times during E-field saturation at – 15 V. The Ds spectra are presented from 2110 cm^{-1} to 1900 cm^{-1}. In (c-d) the integrated intensity of the Ds of the CO_L band are shown after baseline correction and integration from 2110 cm^{-1} to 1900 cm^{-1}.

Figure 7(a) display the ATR-IR spectra during the E-field CO saturation experiments at application of V = - 15 V as a function of time. *t* = 0 at the moment the E-field is switched on. The Ds (difference spectra) in **Figure 7(b)** are calculated from the results in **Figure 7(a)** by substraction of the final spectrum (at *t* = 200 min.) from each individual spectrum, i.e. Ds = t_i - t_f. The integrated area of the observed difference around 2090 cm^{-1} (see **Figure 7(b)**) is presented after baseline correction and integration (from 2110 cm^{-1} to 2070 cm^{-1}) for E-fields directed downwards (**Figure 7(c)**) and upwards (**Figure 7(d)**).

In Figure 7(c) we observe small but significant changes during experiment 3, which scale with the magnitude of the applied negative potentials. The largest changes in the region around 2090 cm^{-1} are observed for the experiment at -15 V, for 0 V and positive potentials (**Figure 7(d)**) no changes are observed.

8.4. Discussions

Although the here presented results are preliminary, we list in this paragraph a set of important observations and questions for this discussion.

8.4.1. E-field saturation + oxidation (experiment (1))

In **Figure 4** and **Figure 5** a strong influence of the E-field during CO saturation + CO oxidation (experiment 1) is observed. For 0 V experiments the oxidation time (time to the initiation of the rapid oxidation) of CO is ~ 360 min, while for the other experiments (i.e. ± 2.5 V to ± 15 V) considerably longer times were before the rapid oxidation of CO started. How could we explain this behavior? Some consideration for the interpretation of the data are given below.

Firstly, we observe that the integrated peak area for CO_L is not constant through the experiment in **Figure 4(a-b)**. The intensity is constant till t ≈ 100 min, then increases (in total roughly 5 – 10 %) to *t* ≈ 150 min, followed by a decrease (in total ~ 20 % of the maximum signal) till the moment that the rapid oxidation sets in. In general we could explain this behavior as a CO self-poisoning as observed on for instance Pt(110)[4] or Pt(001)[5]. The timescales of the oscillations are in the order of 1 or 2 seconds, with a total reaction times amounting up to 10 min. It is important to realize that these oscillations are observed when both dissociated O_2 and adsorbed CO are present in the form of co-adsorbed O_{ads} and CO_{ads}. The decrease from $t \sim 150$ min to the onset of the rapid oxidation could be explained by assuming that O_2 is able to adsorb molecularly on the Pt surface, possibly by removing adsorbed CO, therefore causing the integrated intensity in **Figure 4** to go down. Once, in that picture O_2 is able to dissociate, the oxidation reactions start, thereby generating more empty adsorption sites, which leads to the rapid oxidation. Molecular adsorption of O_2 is, however, not observed at room temperature, but at lower temperatures.[6]

Secondly, the total oxidation time we observed is in the same order of magnitude as reported earlier by our group on thin film of Pt on a ZnSe total internal reflection element.[7] In this study the authors however report a fast initial oxidation rate, which is in contrast to the long oxidation time observed here.

Lastly, the presence of an electrical field in the "saturation time" apparently leads to a "stabilization" of CO, which lasts remarkably long (hundreds of minutes). The exact reason for this "memory effect" is currently unclear and further analysis is required for further elucidation.

Since the residence time is really short (3 s) on the timescale of the experiments, as is the time to titrate of a stoichiometric amount of CO, hydrodynamics are unlikely to play a decisive role.

8.4.2. E-field oxidation (Experiment (2))

To investigate the role of the presence of an E-field during the oxidation, a control experiment was performed in which the E-field was only applied during the oxidation an not during saturation (experiment 1). Surprisingly there was no influence of the presence or absence of an E-field on the oxidation time, indicating that the "memory" of CO was solely set during the "saturation time" as observed in experiment 3. Is important to note that the morphological changes (as presented in **chapter 7**) do not influence "memory" effect during CO oxidation.

8.4.3. E-field saturation (experiment (3))

The observed changes in the difference spectra around 2090 cm^{-1} reveal clearly that the CO band is slightly altered due to the presence of the applied potential during CO saturation period. It is found that this band scale with the application of a negative potential, while for positive potentials no changes were observed. The lengthening of the oxidation time in experiment (1) is observed for both negative and positive potentials, while the here observed only occur for negative potentials, indicating that these two phenomena are not fully correlated.

8.5. Conclusions

In conclusion, we found a unexpected effect of the presence of an E-field during CO adsorption on the time needed for oxidation of the adsorbed CO. The presence of the E-field results in a longer CO-oxidation time, amounting up to a maximum of 8 hours, which is two hours longer than without an applied E-field. Further analysis for a solid interpretation of this phenomenon is required.

8.6. References

(1) Berlowitz, P. J.; Peden, C. H. F.; Goodman, D. W.; *J. Phys. Chem.*, **92**, (1988) 5213

(2) An, K.; Alayoglu, S.; Musselwhite, N.; Plamthottam, S.; Melaet, G.; Lindeman, A. E.; Somorjai, G. A.; *J. Am. Chem. Soc.*, **135**, (2013) 16689

(3) Mojet, B. L.; Miller, J. T.; Ramaker, D. E.; Koningsberger, D. C.; *J. Catal.*, **186**, (1999) 373

(4) Jakubith, S.; Rotermund, H. H.; Engel, W.; von Oertzen, A.; Ertl, G.; *Phys. Rev. Lett.*, **65**, (1990) 3013

(5) Gorodetskii, V. V.; Elokhin, V. I.; Bakker, J. W.; Nieuwenhuys, B.E.; *Catalysis today*, **105**, (2005) 183

(6) Zambelli, T.; Barth, J. V.; Wintterlin, J.; Ertl, G.; *Nature*, **390**, (1997) 495

(7) Ebbesen, S. D.; Mojet, B. L.; Lefferts, L.; *Langmuir*, **22**, (2006) 1079

9

Summary and Outlook

Closing of an E-field cycle

The research described in this thesis aimed to explore new concepts in catalysis with the use of a homemade ATR-IR silicon-based microreactor. During this journey we have performed multidisciplinary research at the interface between physics and chemistry. New insights in the fabrication, integration and characterization of ATR-IR microreactors were generated. Excitingly, a goal of this project is achieved with the fabrication of an E-field device which allows the study of catalytic chemical reactions with ATR-IR spectroscopy. This work shows promising potential for the application of microreactor technology to study *in situ* chemical processes influenced by external electrical fields..

"*Switch* ***off*** *the light*"

9.1. Summary

Chapter 1 provides a general overview of the scope of the thesis and the steps in the fabrication of a new ATR-IR microreactor, which allows application of an external electrical field. In this work we attempt to lower the activation barrier as a new approach to control the selectivity of a chemical reaction by application of an external electrical field.

In **Chapter 2** we compare two silicon dry etching methods to create various microstructures, by varying the gas loading during reactive ion etching (RIE) using a single mask-layer etching procedure. The sculpting of the microstructure shapes was systematically investigated and the resulting structures are reported.

Chapter 3 describes the water and oil repellency of the fabricated microstructures (micropillars), which display high equilibrium contact angles. We have studied the evaporation-driven wetting transition of water on these substrates. We verified whether the observed transitions could be described with the global interfacial energy argument. Our results indicate that for some substrates such argument cannot describe the wettability of a surface correctly, i.e. the Cassie-Baxter to Wenzel transition. We attribute this to the added roughness and edge-curvature (by the RIE process) which are the physical origin of an imposed energy barrier. These micropillars can also be used as electrodes in ATR-IR microreactors.

In **Chapter 4** we present the fabrication, characterization and application of ATR-IR microreactors in which an electric field can be applied over a gas or liquid medium. We compare the generated E-field values with the E-field strength of a zeolite. In order to reach the higher field strengths and in order to prevent field electron emission through the flow channel, the microreactor has to be optimized further.

In **Chapter 5** describes the use of ATR-IR microreactor for studying changes around 1727 cm^{-1} in the IR spectra upon applying an E-field. We reveal that the encountered changes are caused by other phenomena and not due to adsorbed molecules. We evidence that the observed changes are related to oxygen interstitial defects (O_i) in Si. The O_i signal decreases with increasing electrical field strength, which is attributed to the depopulation of the ground-state of the vibration as a consequence of the enhanced temperature.

In **Chapter 6** we demonstrate that electron transport through *n*-hexane is possible. The changes in the IR bands upon/during electron conduction suggest two possible scenarios: Firstly, Electro-optical Kerr Effect during the application of the E-field and secondly, an assembly-organization mechanism of the packed molecular layer. Excitingly more studies with this device are expected, e.g. E-field chemistry in organic liquids for fine chemical applications.

Chapter 7 discusses the capability of *in situ* ATR-IR measurements after coating the microreactor flow channel with Pt nanoshapes. This enhances the adsorption of CO species, which allowed mechanistic and spectrochemical studies. We demonstrate the potential of the device for investigations on E-field induced structural changes of metallic nanoshapes by using CO as a probe molecule. We show that the induced changes can be explained by an enhanced ripening process of the Pt nanoparticles.

In **Chapter 8** the changes in reactivity upon applying an E-field are discussed. Surprisingly, the presence of an external E-field during the chemisorption of CO at room temperature plays a decisive role in the CO oxidation time.

9.2. Outlook

9.2.1 ATR-IR Microreactor redesign

In order to achieve a strong E-field in the channel of ATR-IR microreactor, similar in strength to the ones in zeolites,[1, 2] narrower interspaces (channel heights) are required. These variations lead to consider a redesign of the ATR-IR microreactor. Furthermore, several other points also have to be considered in the new microfabrication procedure. Firstly, to avoid any bending of the flow channel of the crystal during the alignment, prebonding and fusion bonding[2-4] the use of more supporting columns[3-5] is essential. Secondly, the effect of having smaller interspaces might electron emission through the microreactor flow channel, thus the addition of a thicker insulating layer with low dielectric constant will be beneficial.[3] Thirdly, the interference of micropillars in the IR spectra, might be reduced by a non-uniform distribution of the pillars to avoid the reported artifact,[3, 4] with the possibility to perform IR measurements at higher resolutions (i.e. 1 cm^{-1} and 4 cm^{-1}). Lastly, the deposition of thermally stable catalyst materials (i.e. between 900 to 1000 °C[6]) during the chip fabrication procedure would avoid difficult prost-fabrication methods.

9.2.2 Coupling IR polarized light in ATR microreactor

The use of polarized IR light radiation,[7] i.e. s-polarized (⊥) or p-polarized (=) IR radiation in a ATR-IR microreactor to differentiate between perpendicular (⊥) and/or parallel (=) oriented to the ATR-IRE adsorbed CO_L molecules on platinum upon applying an E-field is proposed (see **Figure 1**).

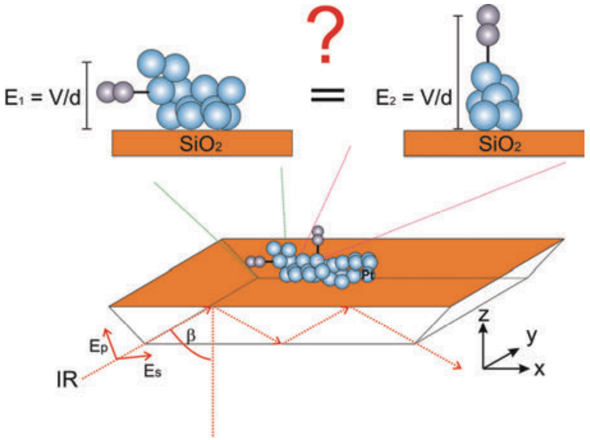

Figure 1. A schematic representation of the direction and polarization of the IR beam in the ATR-IRE. In the left-top side of the sketch a CO_L molecule parallel to the ATR-IR surface is presented, while a molecule oriented perpendicular to the ATR-IR surface is shown in the left-top side. The electromagnetic field (E) directions of p-polarized (E_p) and s-polarized IR light are (E_s) are indicated.

References

(1) Blatter, F.; Moreau, F.; Frei, H.; *J. Phys. Chem.*, **98**, (1994) 13403

(2) **Chapter 1** in this thesis

(3) **Chapter 4** in this thesis

(4) **Chapter 5** in this thesis

(5) **Chapter 6** in this thesis

(6) Etacheri, V.; Seery, M. K.; Hinder, S. J.; Suresh, C. P.; *Adv. Funct. Mater.*, **21**, (2011) 3744

(7) Ras, R. H. A.; Schoonheydt, R. A.; Johnston, T. C.; *J. Phys. Chem. A*, **111**, 8787

9

Samenvatting en Outlook

"Closing of an E-field cycle"

In het in dit proefschrift beschreven onderzoek worden nieuwe concepten in katalyse onderzocht met behulp van een Silicium gebaseerde ATR-IR microreactor. Dit onderzoek was een multidisciplinaire wandeling op het grensvlak tussen natuurkunde en scheikunde. Er zijn nieuwe inzichten opgedaan in de fabricage, integratie en karaterisatie van ATR-IR micro-reactoren. Een aansprekend doel van het project, om een katalytische reactie te bestuderen door middel van ATR-IR spectroscopie onder toepassing van een elektrisch veld is verwezenlijkt met de fabricage van deze reactor. Het werk heeft potentieel om te leiden tot nieuwe toepassing van microreactortechnologie waarin een elektrisch veld wordt gebruikt om chemische processen te sturen.

"*Switch* ***off*** *the light*"

9.1. Samenvatting

Hoofdstuk 1 geeft een algemeen overzicht van dit proefschrift en de fabricage-stappen van de nieuw ontwikkelde ATR-IR micro-reactor, waarin de toepassing van een extern elektrisch veld in situ kan worden bestudeerd met ATR-IR spectroscopie. Einddoel van het werk is om de activeringsenergie van een katalytische reactie te verlagen door toepassing van een extern elektrisch veld.

In **hoofdstuk 2** worden ets-procedures om verschillende microstructuren aan te brengen in een Si wafer beschreven. Door variatie van de gas compositie gedurende het etsen door een masker werd de vorm van de microstructuren systematisch gevarieerd.

Hoofdstuk 3 bevat een gedetailleerde studie naar de water en olie afstotende eigenschappen van sommige van de gefabriceerde microstructuren (voornamelijk micropilaren). De verdamping ge-induceerde bevochtiging door water is gebruikt om de robuustheid van de bevochtingseigenschappen van deze oppervlakken te testen. Er is bekeken of deze Cassie-Baxter naar Wenzel overgang beschreven kan worden de totale grensvlak energie in deze twee situaties met elkaar te vergelijken, wat niet het geval bleek. In bepaalde gevallen bleek de Cassie-Baxter naar Wenzel overgang niet plaats te vinden, wat wordt toegeschreven aan de additionele oppervlakte ruwheid en toegenomen kromtestraal van de pilaren, als fysische oorzaak van een kinetische barrière.

In **hoofdstuk 4** wordt de ontwikkeling, karakterisering en toepassing beschreven van ATR-IR micro-reactoren waarin een extern elektrisch veld wordt aangelegd over een gas of vloeistofmedium. De behaalde veldsterktes in de microreactor worden vergeleken met de berekende veldsterktes in zeolieten. Het blijkt dat de microreactor verder geoptimaliseerd zou moeten worden om vergelijkbare veldsterktes als in zeolieten te halen zonder significante electronen-overdracht door de reactor.

Hoofdstuk 5 beschrijft een studie naar veranderingen in het ATR-IR spectrum van de microreactor rond 1727 cm^{-1} als er een elektrisch veld wordt toegepast. De gevonden veranderingen worden toegeschreven aan "artefacten" en niet aan geadsorbeerde moleculen. De veranderingen rond 1727 cm^{-1} blijken te zijn gerelateerd aan interstitieel zuurstof (O_i) in het silicium. Het O_i signaal neemt af bij toenemende veldsterktes, wat wordt toegeschreven aan een verminderde bezetting van de grondtoestand van deze vibratie ten gevolge van de oplopende temperatuur in de microreactor bij toenemende veldsterktes.

Hoofdstuk 6 beschrijft de veranderingen in de ATR-IR spectra als een extern veld wordt toegepast over een microreactor met n-hexaan. Mogelijke scenario's voor de veranderingen in de absorptie spectra, een electro-optisch Kerr effect en een vorm van zelf-organisatie van de hexaan moleculen, worden beschreven.

Hoofdstuk 7 beschrijft de coating van de ATR-IR microreactor met Pt nanodeeltjes. Op de aangebrachte Pt nanodeeltjes wordt CO geadsorbeerd, wat in situ wordt gevolgd door middel van ATR infrarood spectrocopie. Er is zowel lineair geadsorbeerd als gebrugd geadsorbeerde CO aanwezig. De afname van de geintegreerde intensiteit van de lineair geadsorbeerde moleculen in opeenvolgende experimenten wordt toegeschreven aan een verlaging van het beschikbare oppervlak ten gevolge van sintering van de Pt nanodeeltjes.

In **hoofdstuk 8** wordt het effect van de aanwezigheid van een extern elektrisch veld op de benodigde tijd voor CO oxidatie in deze ATR-IR microreactoren beschreven. Het blijkt dat de aanwezig van het externe veld tijdens de chemisorptie van CO een beslissende rol speelt voor de benodigde CO oxidatie tijd.

9.2. Outlook

9.2.1 Herontwerp van de ATR-IR microreactor

Ten einde voldoende hoge elektrische veldsterktes (vergelijkbaar met de berekende veldsterktes in zeolieten) te bereiken in het kanaal van de ATR-IR micro-reactor, is een kleinere reactor hoogte vereist. Dit vereist een herontwerp van de ATR-IR micro-reactor. De volgende aspecten moeten daarbij in ogenschouw worden genomen. Ten eerste om te voorkomen dat het micro-reactorkanaal vervormd gedurende de fabricage is het aan te bevelen om meer pilaren te gebruiken die de beide zeiden van de reactor met elkaar verbinden en daardoor de reactor verstevigen. Ten tweede, om toename van electronen-emmissie bij nauwere kanalen te voorkomen, is het gebruik van een dikkere isolerende tussenlaag (met een lage di-electrische constante) aan te bevelen. Ten derde kan de interferentie door de micropillaren in de ATR-IR spectra verminderd worden door de ondersteunende pilaren niet-uniform te plaatsen, waardoor accurate metingen met hogere resolutie mogelijk worden. Als laatste zou de depositie van thermisch stabiele (tot 1000 °C) katalysatoren gedurende de fabricage van de micro-reactor de moeilijkheden om na de fabricage katalysatordeeltjes in de reactor te krijgen vermijden.

9.2.2 Gebruik van gepolariseerd IR licht in de ATR-IR microreactor

Het gebruik van gepolariseerd licht, loodrecht op de voortgangsrichting (⊥) of parallel daaraan (=) kan mogelijk gebruikt worden om onderscheid te maken CO moleculen georiënteerd loodrecht op of parallel aan het ATR kristalvlak (zie **figuur 1**).

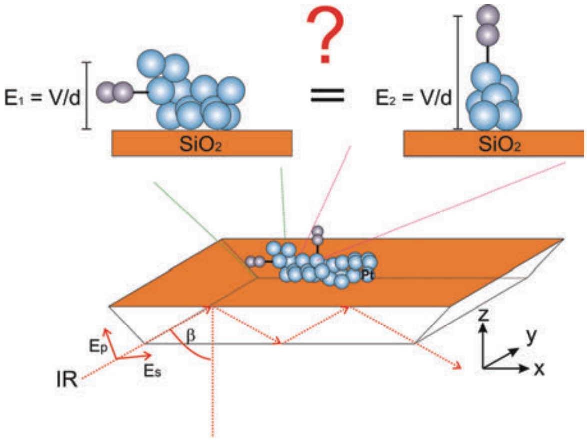

Figuur 1. Schematische weergave van een gepolariseerd IR licht in het ATR kristal. Linksboven een schematische weergave van een lineair geadsorbeerd CO molecuul parallel georiënteerd aan het ATR kristaloppervlak, rechts een schematische weergave van een lineair geadsorbeerd CO molecuul met een loodreachte orientatie ten opzichte van het ATR kristal. De polarsatierichtingen van het infrarode licht zijn weergeven met E_p (loodrecht) en E_s (parallel).

References

(1) Blatter, F.; Moreau, F.; Frei, H.; *J. Phys. Chem.*, **98**, (1994) 13403

(2) **Chapter 1** in this thesis

(3) **Chapter 4** in this thesis

(4) **Chapter 5** in this thesis

(5) **Chapter 6** in this thesis

(6) Etacheri, V.; Seery, M. K.; Hinder, S. J.; Suresh, C. P.; *Adv. Funct. Mater.*, **21**, (2011) 3744

(7) Ras, R. H. A.; Schoonheydt, R. A.; Johnston, T. C.; *J. Phys. Chem. A*, **111**, 8787

About the Author

Arturo Susarrey Arce, was born in La Paz, Baja California Sur, Mexico. He graduated from Universidad Autonoma de Nuevo Leon. He worked for few years in the research and development department in Johnson Controls-Latin America division. Then he finished his masters studies in Materials Science and Engineering at the Universidad Nacional Autonoma de Mexico. Immediately after finishing his fellowship in Italy, he started his PhD at University of Twente. The current work present part of the outcome of his PhD research.

About the cover of my thesis

The combination of colors reflects the passion and commitment with my work, activities and friends. The front cover of my thesis shows a simple atomistic representation of a crystal structure. On top, throughout the sketched structure, an infrared beam is placed which summarize my work with ATR-IR. In the back cover of the thesis, my graphical biography is sketched. Having grown up in Loreto, Baja California Sur, Mexico, the central picture provides an example of the gorgeous town. Linked to it, from bottom to top, I combine my research activities and sports (e.g. see the “numero de participante” 22), followed by my experiments (see basic lab-kit) and another more touristic picture of my beautiful port. The meaning of the upward direction of the steps (made by using one of my sport shoes) is:

W*e should never go down.*

In life no matter what the cause is, we should always try to go up

– by *Rossana Yañez Mendoza.*

Publications:

[14] A. Susarrey-Arce, *et al.*, *CO oxidation on Pt nanoparticles in low E-fields studied by ATR-IR spectroscopy*, (in preparation) (2014)

[13] A. Susarrey-Arce, *et al.*, *CO adsorption on Pt nanoparticles in low E-fields studied by ATR-IR spectroscopy*, (in preparation) (2014)

[12] A. Susarrey-Arce, *et al.*, *Electric field-induced molecular polarization of n-hexane in an ATR-IR microreactor*, (in preparation) (2014)

[11]. A. Susarrey-Arce, R.M. Tiggelaar, E. Karabudak, R.G.P. Sanders, B. Geerdink, S. Schlautmann, L. Lefferts, A. van Houselt and J.G.E. Gardeniers, *A new ATR-IR microreactor to study electric field driven processes* (submitted) (2014)

[10]. A. Susarrey-Arce, R.M. Tiggelaar, R.G.P. Sanders, B. Geerdink, L. Lefferts, J.G.E. Gardeniers, A. van Houselt, *J. Phys. Chem. C*, 117 (2013) 21936

[9]. A. Susarrey-Arce, Á.G. Marín, S. Schlautmann, L. Lefferts, J.G.E. Gardeniers and A. van Houselt, *J. Micromech. Microeng.*, 23 (2013) 025004

[8]. T. Tran, H. J. J. Staat, A. Susarrey-Arce, T. C. Foertsch, A. van Houselt, H. Gardeniers, A. Prosperetti, D. Lohse, Chao Sun, *Soft Matter*, 9 (2013) 3272

[7]. Á.G. Marín, H. Gelderblom, A. Susarrey-Arce, A. van Houselt, L. Lefferts, J. G. E. Gardeniers, D. Lohse and J. H. Snoeijer, *Proceedings of the National Academy of Sciences*, 24 (2012) 1

[6]. A. Susarrey-Arce, Á. G. Marín, H. Nair , L. Lefferts , J. G. E. Gardeniers , D. Lohse and A. van Houselt, *Soft Matter*, 8 (2012) 9765

[5] A Susarrey-Arce, V Petranovskii, MA Hernández-Espinosa, R Portillo, W de la Cruz, *Journal of Nanoscience and Nanotechnology*, 11 (2011) 5574

[4] N. Bogdanchikova, I. Tuzovskaya, A. Pestryakov, A. Susarrey-Arce, *Journal of Nanoscience and Nanotechnology*, 11 (2011) 5476

[3] Arturo Susarrey-Arce, Miguel Angel Hernández-Espinosa *et al.*, *Particle & Particle Systems Characterization*, 27 (2010) 100

[2] A Susarrey-Arce, M Herrera-Zaldívar, W de la Cruz, U Pal, *Journal of Nano Research*, 5 (2009) 177

[1] A. Susarrey-Arce, M Herrera-Zaldívar, V Petranovskii, *Studies in Surface Science and Catalysis*,
174 (2008) 173

Proceedings and others:

[3] M. C. Ramirez-Camacho, I. Tuzovskaya, A. Susarrey-Arce, A. Pestryakov, N. Bogdanchikova, *Advanced Materials Research*, 880 (2014) 253

[2] M. C. Ramirez-Camacho, I. Tuzovskaya, N. Bogdanchikova, A. Susarrey-Arce, V. Gurin, *Advanced Materials Research*, 872 (2014) 94

[1] A. Susarrey-Arce, A. van Houselt, Nederlands tijdschrift voor natuurkunde, 79 (2013) 86

Conferences

Susarrey Arce, A.; Houselt, A. van; Gardeniers, J.G.E.; Lefferts, L.; Reaction-desorption assited by an electrical field - fact or fiction? Conference: NCCC XIII: Noordwijkerhout, The Netherlands (2011)

Susarrey Arce, A.; Houselt, A. van; Lefferts, L; Gardeniers, J.G.E.; Towards selective oxidation by electrostatic manipulation. Annual Meeting 2011, MESA$^+$: Enschede, The Netherlands (2011)

Susarrey Arce, A., Houselt, A. van, Gardeniers, J.G.E. & Lefferts, L.; Towards selective oxidation by electrostatic manipulation. Conf. Energy and Materials from the Sun: Rolduc Abbey (2011)

Susarrey-Arce, A.; Tiggelaar, R.M.; Houselt, A. van, Gardeniers, H.; Lefferts, L.; A Microreactor for electrostatic manipulation combined with ATR in situ characterization technique. Conf. Energy and Materials from the Sun: Rolduc Abbey (2012)

Susarrey Arce, A.; Houselt, A. van; Gardeniers, J.G.E.; Lefferts, L.; Electric field (E-field) driven processes studied in an ATR-IR microreactor. Conference: NCCC XIII: Noordwijkerhout, The Netherlands (2013)

Susarrey Arce, A.; Gomez Marin, A.; Schlautmann, S.; Lohse, D.; Lefferts, L.; Gardeniers, H.; Houselt, A. van; Towards the Design of Omniphobic Surfaces and Its Applications, MRS fall meeting, Boston (2014)

Acknowledgements

The last four years, I have met many people. I would like to thank to all of them for their contribution to this thesis without their support and advices this thesis would not be possible. I would like to express my gratitude to Prof. Dr. Ir. L. Lefferts and Prof. Dr. H. Gardeniers for the given opportunity to carry out my PhD in and Catalytic Processes and Materials (CPM) Mesoscale Chemical Systems (MCS) at University of Twente. I would like to thank Prof. Dr. Ir. L. Lefferts for the freedom he gave to carry out my experiments. Believing in me and in this project and encourage throughout all the faced challenges is a is not an easy task. For this I would like to thank Dr. A. van Houselt and Prof. Dr. H. Gardeniers.

I would like to extend my acknowledgements to my committee members for their suggestions and comments on my thesis. Prof. Dr. S. Franssila, Prof. Dr. G. Mul, Prof. Dr. Ir. A. I. Stankiewicz and Prof. Dr. D. Lohse.

There are many people with whom I have greatly collaborated along these four years. Dr. R. Tiggelaar for your help, inputs and suggestions. My appreciation to Dr. A. G. Marín for his enthusiasm and contributions to this work. I would like to acknowledge Dr. H. Nair, Dr. T. Tran, Dr. C. Sun, Dr. H. Gelderblom and Dr. J. H. Snoeijer for their enormous contributions to this work. To Prof. Dr. D. Lohse, my gratitude and appreciation. Thank you for your help and advice.

Many thanks to my co-workers for their contributions, Dr. E. Karabudak, S. Schlautmann, R.G.P. Sanders and B. Geerdink, M. Sc. M. Morassutto, A. te Boekhorst. I would like to also thank the scientific staff from MCS and CPM, Dr. B. Mojet and R. Luttge as well as Prof. Dr. K. Seshan, thank you so much for your advice and consideration.

I would like to thank to K. Altena-Schildkamp, R. Lubkemann, T.L.M. Velthuizen and L. Vrielink for their technical support. To our lovely secretaries J. Emmerich, L. Harryvan, B. Boogaard and my special appreciation to M. de Jong.

I am really fortunate to have wonderful friends, on whom I could always find support and count on. Rossana Yáñez, Kaisa Vikla, Fatemeh Nikayin Silvia Murillo, Yolanda Murillo, Marijana Kovačević, Amanda Davila, Olga Katan, Maaike de Jong, Cristina Franch Martí, Iliana Nava, Kamila Koichumanova, Ana Berta Castro, Sharon Sandoval, Hrudya Nair, Agry Galeana, Maria Castellvi, Reyes Mallada, Federico Hernandez, Roald Tiggelaar, Arie van Houselt, Chie-Chao Yang, Roger Brunet Espinoza, Gonzalo Ríos, Ruben Lubkemann, Koteswara Rao Nidadavolu and Stefan Schlautmann, to you all thank you. To my best-officemates, Yingnan Zhao, Joline van Beek and Shilpa Agarwal, thank you for the great time and friendship.

To my colleagues at CPM, Châu Hoang, Tang Son Nguyen and Jie Zhu, many thanks for the great time that we have spent together. I would like also to thank my colleagues from the MCS group, David Fernandez Rivas, Mattia Morassutto, Wim De Malsche, Engin Karabudak, Rick Elbersen, Bart Schurink, Hoon Suk Rho, Xingwu Sun, Sijia Xie, Hainan Zhang, Elizaveta Vereshchagina, Nikolay Dimov, Roland Blanch Ojea, Brigitte Bruijns and Saskia Schildkamp. Thanks for the nice time and great conversations.

The best-running team ever and my dear friends: Olga Katan, Federico Hernandez, Kaisa Vikla, Roald Tiggelaar and Ruben Lubkemann. It was a great pleasure to run with you guys.

Inga Tuzovskaya and Masoud Zabeti my dear friends and paranymphs, it is an honor to have you next to me during the defense. Thank you for your friendship and support. Inga Tuzovskaya and Masoud Zabeti, my great pleasure to have you here. Thank you once more for your support along these years.

"Ik wil graag Henri Dijkerman en zijn familie bedanken voor hun steun en dat zij hier vandaag zijn".

"Mi más grandioso agradecimiento a mi familia: Arely Arce Peralta, Arturo Susarrey Amador, Soledad Alvarez, Francisco Susarrey Arce, Arely Susarrey Arce y sobrino Arturo Susarrey Arce. Especialmente a mi abuelo, Arturo Susarrey Acero sé que si su condición física le permitiera el estaría aquí a mi lado".

Arturo Susarrey Arce
Enschede, 10th of April 2014

DESIGN: ROSSANA YAÑEZ MENDOZA